Precision Measurements to Explore Underlying Geometries and Interactions in a Trapped Ba$^+$ Ion

Debashis De Munshi

(M.Sc.(Physics), S.N.B.N.C.B.S., West Bengal University of Technology)

A thesis submitted in fulfilment of the requirements

for the degree of Doctor of Philosophy (Ph.D.)

at

Centre for Quantum Technologies,

National University of Singapore,

Singapore

2016

CQT | Centre for Quantum Technologies

National University of Singapore

DECLARATION

I hereby declare that this thesis is my original work and it has been written by me in its entirety.

I have duly acknowledged all the sources of information which have been used in the thesis.

This thesis has also not been submitted for any degree in any university previously.

Debashis De Munshi
31st October, 2016

Dedicated to a bunch of people who themselves may have never entered a lab, but without whom I definitely wouldn't be in a lab.

ABSTRACT

The work described in this thesis consists of both theoretical and experimental research performed on single trapped ion. The barium ion, being a heavy multi-electron system, allows benchmarking of highly demanding ab-initio many body electronic structure calculations. The dipole forbidden transitions in barium ion also serves as a test bed for atomic parity non-conservation, geometric phase generation, optical qubit, etc.

In this work, the possibility of measuring and quantifying geometric phase in two different symmetry of the underlying Hamiltonian has been studied. This study leads to the prospect of using dipole forbidden transition in barium ion as its possible test bed. However, it is essential to measure the quadrupole shift of this transition before implementing the geometric phase measurement protocol.

In the experimental section of this thesis, precision measurement on the allowed dipole transition has been performed to benchmark the many body calculations required to study atomic parity non-conservation in barium ion. Further experiments has been performed in order to measure the quadrupole shift of the dipole forbidden transition. These measurements firmly sets the foundations for future measurements to be performed on both atomic parity non-conservation and implementation of geometric phase generation proposals as developed in the theoretical part of the thesis.

This thesis contains a theoretical proposal to implement geometric phase generation protocol in a trapped barium ion using only electric fields. It further includes the first measurements of branching fraction of dipole allowed transition in barium ion with a precision well below 0.05% which allows us to discriminate between different many body calculations done with a precision of 1%. In addition, this thesis lays the foundation to measure the more challenging electric quadrupole shift of the dipole forbidden transition in barium ion. This led to implementation of a fast optical qubit at a wavelength close to telecommunication wavelength.

List of Tables

List of Figures

Contents

Chapter 1

Introduction

The field of precision measurement aims at improving uncertainties of the measured fundamental quantities. This is required for better understanding of the fundamental properties of nature and the accuracy of our models and theories about the universe. It is the high precision measurements of the fundamental properties of the building blocks of nature like the g-factor of a free electron [1–5], that has allowed us to test the principles of quantum mechanics, in general and quantum field theory, in particular, to extremely high precision. Therefore quantum field theory has emerged as the most precise theory of nature known to mankind till date.

The field of precision measurement also involves developing tools to probe nature with unprecedented precision. It includes developing laser sources with narrower linewidth (more and more precise frequency) [6–8], ultra high vacuum chambers (to develop a truly isolated system) [9] and low noise detection systems. Apart from gaining more in-depth knowledge about the laws of physics, this field has also opened up possibilities of developing quantum technologies. The tools developed for the purpose of precision measurements have been used to harness and manipulate quantum nature of matter [10–19]. The most advanced quantum computer that has ever been built is based on ion traps and utilizes the tools for precision spectroscopy [19–22].

Before moving on to more details of the work, let me introduce what it means to perform a precision measurement. To give an idea about what precision measurements are, we have to distinguish between precision and accuracy. Precision of a measured value refers to the repeatability of the measurement. In other words as is shown in Fig 1.1, it is the scattering of the measured value from its
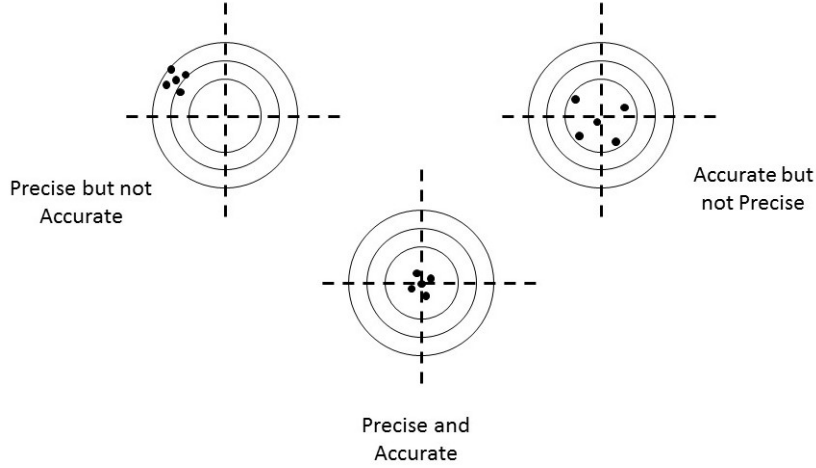
Figure 1.1: The difference between precision and accuracy

mean value, or in other words it is the standard deviation of the measurement. Accuracy on the other hand refers to the deviation of a measured value from the actual or true value of the measured quantity. In either case, larger standard deviation means lower precision or accuracy. As further chapters will reveal, there has been instances where measured values, via increasing its precision, has shed light on the flaws of underlying theories developed by theoreticians to model interactions in nature and that in turn affected the 'accuracy' of the model.

Whether a measurement will be accurate or not is determined by the design of the experiment, or simply put, whether the experiment really measures what it is set to measure. The experiment design also plays a significant role in setting the precision of the measurement. Larger the number of the measured parameters, lower is the precision of the measurement due to error propagation rule.

The work presented in this thesis is geared towards precision measurements of properties of a trapped barium ion. Precision measurements are required for studying both fundamental interactions at the atomic scale as well as to observe and measure geometric phases that can be imposed on the electronic levels of the ion via external field manipulations.

Presence of two metastable excited states of $^{138}Ba^+$ makes it a suitable choice for precision measurements as they have long lifetimes [23–25] and hence narrow linewidth, as narrow as 12 and 31 mHz for $j = \pm\frac{3}{2}$ and $j = \pm\frac{5}{2}$ states respectively . These states for barium also have significantly large quadrupole moment [26], as compared to Ca^+ [27]. This means that these levels can have a

stronger interaction with an electric field gradient. This opens up a variety of opportunities because trapped ions are extremely sensitive to electric fields and it is possible to create configurations of electric field, such that the gradient is non-zero while the electric field is zero.

This thesis is organized in the following manner- Chapter 2 introduces the concepts of ion trapping, laser cooling and coherent manipulations. The third chapter deals with the theoretical considerations regarding precision measurements of properties of barium ion as well as introduces concepts of geometric phase manipulations using external fields. The development of the experimental setup is discussed in the fourth chapter. The fifth and the sixth chapters deal with the results of the precision measurement of branching ratio of excited state of the barium ion and fast qubit operation using dipole forbidden levels of barium respectively. It also discusses the development and challenges towards the measurement of the quadrupole moment of the D levels of the barium ion. The thesis concludes with a summary and outlook for further development of this work.

Chapter 2

Ion Trapping and Laser Cooling

An ion trap is a device which allows confinement of charged particles in space using electric and/or magnetic fields [28–39]. Basic electrodynamics tells us that charged particles cannot be held in space using only static electric field. This is evident from the differential form of the Gauss's law which gives us the following equation for electrostatic potential in free space-

$$\nabla^2 V = 0. \tag{2.1}$$

The Laplace's equation, Eq .2.1, has the mathematical property that its solutions does not have any minima, or maxima, anywhere other than at the boundaries. It is like a stretched membrane. Unless one presses down the middle of the membrane, there is no minima anywhere. Similarly if there is no charge, then nothing is 'pressing down' the potential and thus there is no minima anywhere. However, what can be done, and has been done, is using certain configurations of time dependent electric fields, one can create certain motion of ions, which are confined to a limited volume in space. A Paul trap works based on this dynamic electric field. In this thesis only Paul traps are used and hence the following discussions are restricted to this kind of ion trap alone. However, static magnetic fields or a combination of electric and magnetic fields can also be used for ion confinement.

To understand physically the principle of operation of an ion trap, imagine you holding a hot potato. You do not want the potato to fall, but you also cannot keep holding it in one hand. So you keep on bouncing it between both of your hands. An ion trap also uses a similar idea. As an ion starts moving in one direction, the potential changes in time such that, by the time, it reaches the boundary of its confinement, it faces a high potential and starts going back in the opposite direction. Thus in an

ion trap, the trapping is dynamic process where the ion is constantly kicked around and kept confined within the trapping volume.

2.1 Mathematical Description and Equation of Motion

So now that the idea of trapping a charged particle is established, it is time to formulate the equation of motion for the ions confined in a trap. As one can feel already, the frequency, which is like the rate of compensation, and the amplitude, what is how hard you compensate, of the time dependent fields will depend on the mass and charge of the ion. This is because mass governs the motional velocity of the ion while responding to the compensation and change governs its strength.

From classical mechanics, we know that any minima, up to the first significant order, can be approximated with a simple harmonic oscillator, which has a quadratic dependence of potential in space. So we model the confining potential as a three dimensional harmonic oscillator potential. We also assume that the electric field varies in a sinusoidal manner. This is a reasonable assumption because any other type of dependence can always be resolved in terms of different sinusoidal frequencies (fourier decomposition) and so knowing the equation of motion for one single driving frequency will allow us, if necessary, to understand the equation of motion for any other type of time dependence. The generalized potential required to confine the ion can be written as [38, 39]

$$V(x, y, z, t) = \frac{V_s}{2}(\alpha_1 x^2 + \alpha_2 y^2 + \alpha_3 z^2) + \frac{V_d}{2}\cos(\omega_{rf} t)(\alpha_1' x^2 + \alpha_2' y^2 + \alpha_3' z^2). \qquad (2.2)$$

V_s represents the amplitude of the static part of the potential and V_d the amplitude of the dynamic part. α_i and α_i' are the geometrical weight factor for each dimension, for the static and dynamic parts of the potential respectively.

Now Eq. 2.1 and Eq. 2.2 constrains the values of α and α'. So

$$\sum_i \alpha_i = 0 \qquad (2.3)$$

16

and

$$\sum_i \alpha_i' = 0. \tag{2.4}$$

These conditions can be met in a variety of ways. However, two typical ways are $\alpha_1 = \alpha_2 = -\frac{1}{2}\alpha_3$; $\alpha_1' = \alpha_2' = -\frac{1}{2}\alpha_3'$ and $\alpha_1 + \alpha_2 = -\alpha_3$; $\alpha_1' = -\alpha_2'$; $\alpha_3' = 0$. The first situation corresponds to what is called a ring trap and the second condition is met in a linear Paul trap [38,39], the trap type we use in this work.

If one writes the classical equation of motion of a charged particle in a potential of the form given in Eq. 2.2, then the equation belongs to a general class of equations called the Mathieu's equations. This class of equations represents solution of a simple harmonic oscillator with a time dependent restoring force. Starting from $\ddot{x} = -\frac{e}{m}\frac{\partial V}{\partial x}$, where V is the potential in Eq. 2.2, we obtain the equation of motion of the ion in each dimension as

$$\frac{d^2x}{d\theta^2} + \{a_x - 2q_x\cos(2\theta)\}x = 0, \tag{2.5}$$

where $\theta = \frac{\omega_{rf}t}{2}$, $a_x = \frac{4eV_s\alpha_1}{m\omega_{rf}^2}$ and $q_x = \frac{4eV_d\alpha_1'}{m\omega_{rf}^2}$ respectively.

The solution for the Mathieu's equation is of the form [38]

$$x(\theta) = Ae^{i\beta_x\theta}\sum_{n=-\infty}^{\infty} C_{2n}e^{i2n\theta} + Be^{-i\beta_x\theta}\sum_{n=-\infty}^{\infty} D_{2n}e^{-i2n\theta}. \tag{2.6}$$

In the lowest order of approximation, $\beta_i = \sqrt{a_i + q_i^2/2}$ and stable orbits for the trapped ions are achieved only for $0 \le \beta_i \le 1$. Fig. 2.1 shows the stable trapping parameters for a linear Paul trap.

For the linear Paul trap realization, $a_{x,y} = 0$, $\beta_{x,y} = q_{x,y}/\sqrt{2}$. This allows us to fix the range of frequencies and amplitudes of the rf potential that is to be applied to trap a singly charged barium ion, with mass 138 a.m.u., in the radial direction.

In the lowest order approximation, the orbit of a trapped ion in each of the radial dimension is given by

$$x(t) = x_0\cos\left(\beta_x\frac{\omega_{rf}t}{2}\right)[1 - \frac{q_x}{2}\cos\left(\omega_{rf}t\right)]. \tag{2.7}$$

17
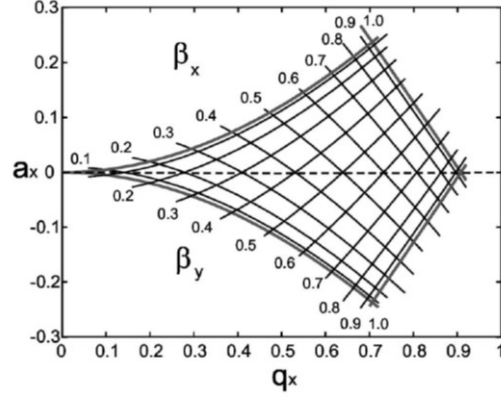
Figure 2.1: The parameter region which gives stable confinement of trapped ions [38].

The ion motion has a lower frequency component given by $(\beta_x \frac{\omega_{rf} t}{2})$, which is called the secular frequency, and a high frequency component that drives at the frequency of the radio-frequency field. The second component is called the micro-motion.

2.1.1 Experimental Trap Realization

As already mentioned in this work a linear Paul trap configuration is used to confine singly charged barium ion with mass number of 138 a.m.u. For achieving the highest stability, the trap parameters, such as RF voltage and frequency are set such that the stability parameter q has a value approximately 0.4. Fig. 2.1 shows the parameter values which give stable ion motion and allows for trapping the ions.

The rf voltage is applied to the blade structures, as shown in Fig. 2.2 instead of rods as it allows for greater optical access.

For such a configuration, the geometric parameter, $\alpha'_{x,y}$, for the radial direction, becomes $\alpha'_{x,y} = 1/r_0^2$. Thus for radial confinement, the stability parameter for a linear Paul trap is $\beta = \frac{4eV_d}{\sqrt{2}m\omega_{rf}^2 r_0^2}$.

For a linear trap, the axial confinement is achieved by applying DC voltage on the end cap electrodes shown as dots in middle of Fig. 2.2. In the axial direction, the potential is a time independent harmonic trapping potential with the depth of the trap defined by the voltages applied to the end caps.

18
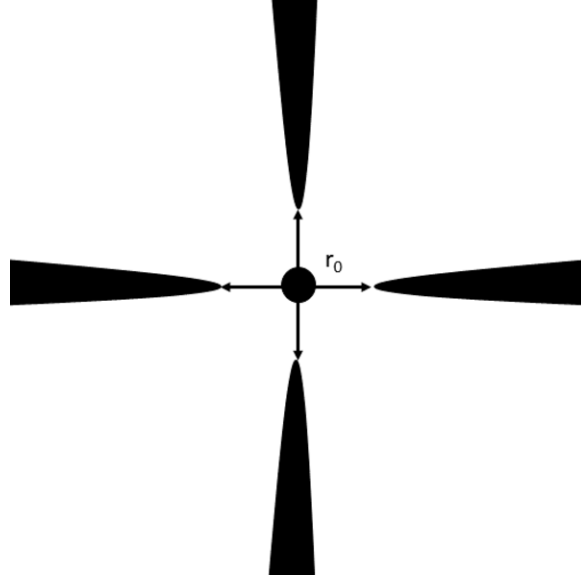
Figure 2.2: Trap configuration: side view showing the RF blades

Ideally, the potential is of the form

$$V_{dc}(z) = \frac{V_0}{z_0^2} z^2,$$

(2.8)

where V_0 is the voltage applied on the end caps and z_0 is the distance of the end caps from the center of the trap. However, in reality, the potential is screened by the other electrodes of the trap. So the exact potential experienced by the ion is determined by measuring the axial secular frequency.

The relation between the trapping frequency and the effective DC potential experienced by the ion can be obtained in the following manner. Let us assume m is the mass of the ion, ω_{dc} is the axial trapping frequency and V_e is the effective DC potential 'seen' by the ion. Using the ideal form of the potential and the spring constant of a harmonic trap being given by $m\omega_{dc}^2$, we obtain

$$\frac{2eV_e}{z_0^2} = m\omega_{dc}^2.$$

(2.9)

This equation gives

$$V_e = \frac{m\omega_{dc}^2 z_0^2}{2e}.$$

(2.10)

For the purposes of the work presented in this thesis, we also need to know the electric field gradient which is experienced by the ion. Using Eq. 2.8 and 2.10, we can obtain the DC electric field gradient experienced by the ion as

$$\frac{dE_z}{dz} = \frac{m\omega_{dc}^2}{e}.$$

(2.11)

19

For the trap used in the experiments presented in this thesis, r_0 is 0.7 mm and z_0 is 2.2 mm. Detailed description about the structure and design of the trap is provided in chapter 3.

2.2   Cooling of Trapped Ions

In this section, we will describe the methods that can be used to cool the trapped ions. The way ion traps work is that the parameters are set to keep the trap in a stable trapping region and then an atomic source is turned on, usually a oven. The atoms are then ionized inside the trap volume and because of the parameters of the trap, these newly formed ions become confined inside the trapping region. However, the trap, being composed of electric fields, represents a conservative force field and hence the energy of the ions are defined by the oven temperature which is usually at about 700 K to 800 K. While it is good enough for certain kinds of experiments, for more precise experiments, we require these ions to have less kinetic energy.

Cooling means a method of dissipation, a process to reduce the kinetic energy of the ions. Energy of the ions can be dissipated by buffer gas collisions, resistively dumping the ion image current on a cooled resistor or by collision with light. In this work we employ lasers to perform the job and hence in the following sections the techniques of laser cooling are described.

2.2.1   Doppler Cooling

The most standard way of cooling down ions now a days is via laser cooling [38, 40–47]. Physically, the mechanism of laser cooling is the following-
Imagine a two level atom. It absorbs one photon of light which excites the atom from the ground state to the excited state. During this process, the atom gets a kick in the direction the photon was coming due to conservation of momentum. Now when the atom falls back to the ground state, the atom will emit a photon, which will also give a recoil kick in the direction opposite to that of the direction of the emitted photon. The cooling process (or heating process; they are equivalent, one takes away kinetic energy and one provides extra kinetic energy by similar mechanism) however relies on the fact that the photon absorption from the laser takes place in one direction, the direction of the propagation of light, but the emission process is symmetric and can take place in any direction in
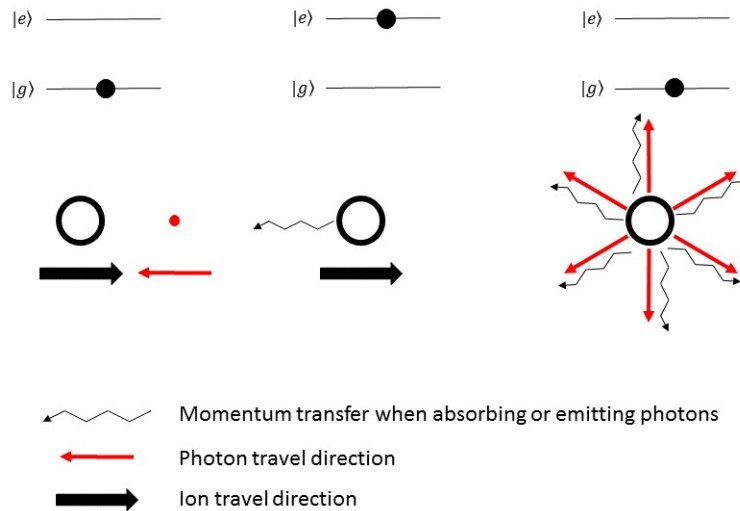
Figure 2.3: The figure shows the process of Doppler cooling. The ion absorbs a photon coming in the opposite direction to its velocity. When the photon is absorbed, it transfers a certain amount of momentum to the ion in the direction opposite to its motion. When the ion releases the photon, it does it in a random direction, compared to its direction of motion. Now when this process is repeated for a large number of times, the ion momentum is reduced by the momentum changes due to absorption while the momentum transfers due to emission is canceled out because of its random nature.

space. Now, when this process takes place multiple number of times, the ion keeps on getting kicks in one direction, because of the photons absorbed from the laser beam, while the recoil from the emitted photons cancel out each other because of their random spherical distribution. Fig. 2.3 gives a visual description for this process. Utilizing Doppler shift, it is possible to tune the laser such that in the atom's moving frame the light is resonant, when it is moving towards the laser beam or away from the laser beam. If the laser frequency is tuned such that the atom sees resonance only when it is moving towards the laser beam, then it will cool down, because the atom will receive the directional kicks opposite to its direction of motion and hence it will reduce the kinetic energy of the atom. However, if the laser frequency is tuned such that the atom 'sees' the laser when it is moving away, then it will heat up the atom and increase the kinetic energy of the atom as the kicks will be in the same direction as the motion of the atom. Since an atom sees a higher frequency, when it is moving towards the light, the frequency of the laser has to be tuned lower than the resonance frequency of the transition so that the atom 'sees' the laser only when it is moving towards it. Since the frequency is lower than the resonance, it is called red detuned. Thus for cooling an atom, the laser should be red detuned compared to the resonance frequency of the atom.

With the above picture of laser cooling, it is now understandable that the cooling process will

strongly depend on how fast the atom can absorb and emit photons. Availability of the laser with the correct frequency is also an important factor in determining whether laser cooling is possible for a given atomic species or not. The rate of photon absorption and emission depends on the laser intensity and linewidth (the spectral density, how much power is there per unit frequency range) and also the natural linewidth of the atomic transition in question. The atomic linewidth will determine how fast an atom de-excites after it has been excited; wider the linewidth, faster is the de-excitation process.

The de-excitation process for the atom should be spontaneous and not stimulated. This is because stimulated emission will lead to emission of photons in the direction of the incoming beam and thus if the transition is dominated by stimulated emission, then the cooling process will be inefficient. Thus the linewidth should be large enough for the atom to not have time to be de-excited via stimulated processes while the laser intensity should also be small enough to avoid stimulated emission as much as possible.

The rate of Doppler cooling is determined by how fast the atom excites and de-excites. The spontaneous emission rate is given by the natural linewidth Γ of the upper state while the wavelength of the light determines the momentum kick the atom receives when it absorbs or emits a photon. The average force on the atom/ion is given as [38, 48]

$$\hbar k \Gamma \rho_{ee}, \tag{2.12}$$

where k is the wave vector of the photon absorbed and ρ_{ee} is the rate of excitation [38, 48]. This rate, ρee, given as $\langle e | \rho | e \rangle = \rho_{ee}$, in turn depends on the laser intensity and frequency as well as properties of the atom which is being cooled. ρ_{ee} can be written as [38, 48]

$$\rho_{ee} = \frac{s/2}{1 + s + (2\delta/\Gamma)^2}, \tag{2.13}$$

where saturation parameter s is defined as $s = \frac{2|\Omega|^2}{\Gamma^2}$ and δ is the effective detuning of light, taking into account detuning from resonance while the atom is at rest as well as the contribution of the Doppler shift. If Δ is the detuning of the laser from the resonance frequency at rest and v is the velocity of the ion, then $\delta = \Delta - \vec{k} \cdot \vec{v}$

The final temperature which doppler cooling can achieve, as can be guessed, depends on the linewidth of the transition, which is being used for the Doppler cooling cycle. The cooling will stop when the doppler shift, because of the motion of the atom/ion, is no longer greater than the natural linewidth of the excited state used to drive the transition. In this limit, sometimes the atom will absorb at the minima of the line and emit at the maxima of the line while some other time, it will absorb at the maxima of the line and emit at the minima of the line. If the laser linewidth is much smaller than the transition linewidth, then the minima of this spread of energy can be achieved when the laser is kept at a detuning, half of the natural linewidth of the excited state. In this situation, the maximum difference between the momentum change due to the absorbed and emitted photon is $\hbar k \Gamma / 2$. If the detuning is bigger than half the natural linewidth, then the difference will be larger than $\Gamma / 2$ and the final temperature achieved will be higher.

To obtain the corresponding temperature, this energy is equated to $k_B T_{Dop}$ and thus the doppler limit of temperature comes out to be [38, 48]

$$T_{Dop} = \frac{\hbar \Gamma}{2 k_B}.$$ (2.14)

For barium ion, the upper state has a linewidth of 15 MHz. This gives a Doppler limit of temperature as 360 μK.
Looking at Eq. 2.12 and 2.14, we will see that there is a trade-off based on the natural linewidth of the atom. Higher the linewidth, faster is the rate of cooling, but the final temperature reached is also higher. On the other hand, with narrower lines, one can reach lower temperatures, but then the rate of cooling is also lower. For this reason, to reach even lower temperatures, one first cools the ensemble using a larger linewidth transition and then employs a lower linewidth transition to perform a resolved sideband cooling [38].

Procedurally, when we load ions in the trap, we keep the laser red-detuned to about 300 MHz to 400 MHz away from the resonance. This is to make sure that the laser can address the initial hot ions. Once trapped, the detuning of the laser is reduced and it is brought closer to resonance till the detuning of $\Gamma / 2$ is reached. Thus one achieves Doppler temperature limit.

|e⟩ —————— |e⟩ ——————— |n = 4⟩
                              ——————— |n = 3⟩
                              ——————— |n = 2⟩
                              ——————— |n = 1⟩
                              ——————— |n = 0⟩

|g⟩ —————— |g⟩ ——————— |n = 4⟩
                              ——————— |n = 3⟩
                              ——————— |n = 2⟩
                              ——————— |n = 1⟩
                              ——————— |n = 0⟩

Free atom energy levels   Trapped atom energy levels
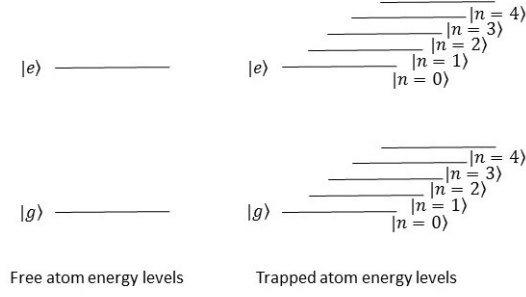
Figure 2.4: Energy level diagrams of a free and trapped atom/ion

2.3   Coherent Manipulation and Resolved Sidebands

As mentioned before, barium ion has a metastable $5D_{3/2}$ and $5D_{5/2}$ states which are coupled to the ground state via dipole forbidden or quadrupole coupling. Because of the long lifetimes of these states, coherent manipulation of the electronic state of the ion is possible using these transitions.

The total hamiltonian of an ion in an ion trap system is written as

$$H_{\text{total}} = H_{\text{atom}} + H_{\text{trap}}, \tag{2.15}$$

where H_{trap} in most of the cases can be written down as a harmonic potential and H_{atom} is the atomic Hamiltonian.

Since the two Hamiltonian have separable Hilbert spaces (H_{atom} acts on the internal state of the atom while H_{trap} acts on the external motional modes of the atoms), the total eigenstate of the system then becomes

$$E_{\text{total}}^i = E_{\text{atom}}^i + (n_{\text{trap}} + \frac{1}{2})\hbar\omega, \tag{2.16}$$

where E_{total}^i and E_{atom}^i is the ith atomic level after and before modification by the trap potential. n_{trap} is the quantum number of the harmonic oscillator eigenstates of the trap. Fig. 2.4 shows the energy levels of a trapped ion (it also works for trapped atoms, though atom traps have much weaker trapping potential).

Thus each internal state of the ion is further split into motional eigenstates which has a ladder structure because of the harmonic potential of the trap. These structures are called the motional sidebands. Due to the extremely narrow linewidth of the D states and th trap frequency being of the order

24

of MHz, these sidebands play a significant role in the coherent manipulations of the ion state.

Thus the physical system can be considered as a two level atomic system interacting with a laser field, superimposed with energy eigenstates of the simple harmonic trap.

In the presence of a laser addressing the transition between the two levels, the total Hamiltonian becomes

$$H_{\text{total}} = H_{\text{atom}} + H_{\text{trap}} + H_{\text{interact}}, \qquad (2.17)$$

where H_{interact} is the interaction between the atom and the light. The generalized form of this interaction can be written as [38, 49]

$$H_{\text{interact}} = \frac{\hbar\Omega}{2}(|g\rangle\langle e| + |e\rangle\langle g|)\left(e^{i(k\hat{x}-\omega t+\phi)} + e^{-i(k\hat{x}-\omega t+\phi)}\right), \qquad (2.18)$$

where k is the wave vector of the light, $\hat{x}$ is the position operator of the ion, Ω is the on-resonance Rabi oscillation frequency for the transition representing the coupling between the two states and ϕ is the phase of the light at the position of the ion.

Rabi oscillation is a driven phenomenon in atomic systems. When a two level atom interacts with laser connecting the two levels, the population of each level (probability of the electron to be in either the ground state or excited state) oscillates with time in a sinusoidal manner. The frequency of this oscillation depends on the intensity and detuning of the laser from the resonance frequency as well as the strength of coupling of the two levels. This frequency of oscillation is called Rabi oscillation frequency.

Eq. 2.18 can be re-written in the interaction picture, and after applying rotating wave approximation [38, 49], as

$$H_{\text{interact}} = \frac{\hbar\Omega}{2}\hat{\sigma}^{+}e^{i(\eta(\hat{a}e^{-i\omega t}+\hat{a}^{\dagger}e^{i\omega t})-\delta t+\phi)} + H.C. \qquad (2.19)$$

Here the two atomic levels are represented in the basis of the Pauli matrices for a spin $1/2$ system, $\hat{a}$ and $\hat{a}^{\dagger}$ are the ladder operators, δ is the detuning of the light from the resonant frequency and η is

the Lamb Dicke parameter, given as

$$\eta = k\sqrt{\hbar/(2m\omega)}. \tag{2.20}$$

Lamb-Dicke parameter is the ratio of the wavelength of light to the spread of the ground state motional wavefunction of the trapped ion. Lamb-Dicke regime is defined mathematically as $\eta \ll 1$ [38, 49]. Physically this means that the recoil of the absorbed or emitted photon is not strong enough to change the motional mode of the trapped ion.

In the Lamb-Dicke regime, Eq. 2.19 can be approximated as

$$H_{\text{interact}} = \frac{\hbar\Omega}{2}\hat{\sigma}^+(1 + i\eta(\hat{a}e^{-i\omega t} + \hat{a}^\dagger e^{i\omega t}))e^{i(\phi-\delta t)} + H.C. \tag{2.21}$$

Thus the equation breaks down into three distinct transitions- the first is between $|n\rangle\,|g\rangle \rightarrow |n\rangle\,|e\rangle$, when $\delta = 0$ with the coupling strength being Ω. This is called the carrier transition. Second is the red sideband, between $|n\rangle\,|g\rangle \rightarrow |n-1\rangle\,|e\rangle$ when $\delta = -\nu$, with a coupling strength of $\Omega_{n,n-1} = \Omega\sqrt{n}\eta$. This is called the red-sideband transition. Third is the transition between $|n\rangle\,|g\rangle \rightarrow |n+1\rangle\,|e\rangle$ when $\delta = \nu$, with a coupling strength of $\Omega_{n,n+1} = \Omega\sqrt{n+1}\eta$. This is called the blue-sideband transition. Fig. 2.5 shows the three different lowest order transitions that are possible due to a laser ion interaction in the Lamb-Dicke regime.
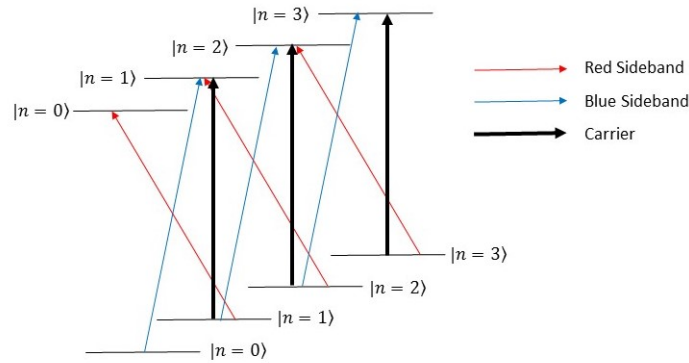
Figure 2.5: The three possible transitions for resolved sidebands in the Lamb-Dicke regime. While carrier makes the transition between the same motional states, the red sideband induces transition between higher to lower motional states while the blue sideband is transition between lower to higher motional states.

The Rabi oscillation can also be used to define the Π time of the system. The Π time is defined

as the excitation time such that probability of excitation after Π seconds is 1. This time signifies the amount of time the atom must be exposed to the laser to coherently transfer the entire population to the excited state. $\Pi/2$ time defines the time in which the probability of excitation is exactly $\frac{1}{2}$ and is half the Π time. Π and $\Pi/2$ pulses are laser pulses having duration equal to Π and $\Pi/2$ time respectively. As can be seen from the previous discussion, the Π time is different for the main transition line and the sidebands. For the sidebands, it is also dependent on the motional state of the trapped ion, with lower motional states having longer Π times.

After Doppler cooling, the trapped ion is thermally distributed among different motional states, with the average phonon number of $\bar{n}$. The distribution is given as [38, 49]

$$p(n, \bar{n}) = \frac{\bar{n}^n}{(\bar{n} + 1)^{n+1}}. \tag{2.22}$$

The excitation probability for a two level system driven by a laser interaction as a function of excitation time is given as

$$p_e(t) = \left| \frac{\Omega}{\sqrt{\Omega^2 + \delta^2}} \right|^2 \sin^2 (\sqrt{\Omega^2 + \delta^2}) t \tag{2.23}$$

and the Rabi frequency between motional modes n and $n + m$ is given as

$$\Omega_{n,n+m} = \Omega | \langle n + m | e^{i\eta(a + a^\dagger)} | n \rangle |. \tag{2.24}$$

From Eq. 2.22, 2.23 and 2.24 it is possible to obtain the generalized excitation probability as a function of time that can be observed for a trapped ion after Doppler cooling at resonance. This equation is modified by the fact that transition between different motional modes have different Rabi frequencies and the ion is thermally distributed among these motional modes. This requires an averaging over different modes to obtain the exact excitation probability, which is different from the solution of the Rabi problem. It is given as

$$P_e(t) = \sum_{n=0}^{\infty} p(n, \bar{n}) \sin^2 (\Omega_n^2 t) \tag{2.25}$$

Using Eq. 2.24 and 2.25 the excitation probability at resonance can be written as a function of time, to the lowest order in η^2, as [38, 49]

$$P_e(t) = \frac{1}{2} \left(1 - \frac{\cos (2\Omega t) + 2\Omega t \eta^2 n \sin (2\Omega t)}{1 + (\Omega t \eta^2 n)^2} \right). \tag{2.26}$$

Eq. 2.26 gives the probability of excitation of the transition line at resonance. However, as we have seen before, in the Lamb-Dicke regime, there are different sideband transitions that are possible- the red sideband and the blue sideband. Let P_{rsb} be the red sideband excitation probability and P_{bsb} is the blue sideband excitation probability.

Assuming a thermal distribution with an average phonon number of $\bar{n}$, P_{rsb} is given as [38, 49],

$$P_{rsb}(t) = \sum_{n=1}^{\infty} p(n, \bar{n}) \sin^2 (\Omega_{n,n-1}^2 t) \tag{2.27}$$

while P_{bsb} is given as

$$P_{bsb}(t) = \sum_{n=0}^{\infty} p(n, \bar{n}) \sin^2 (\Omega_{n,n+1}^2 t) \tag{2.28}$$

Now $\Omega_{n+1,n} = \Omega_{n,n+1}$. Using this equality and Eq. 2.27 and 2.28,

$$P_{rsb}(t) = \frac{\bar{n}}{\bar{n} + 1} P_{bsb}(t) \tag{2.29}$$

If $R = \frac{P_{rsb}(t)}{P_{bsb}(t)}$, then the average phonon number is given as

$$\bar{n} = \frac{R}{R - 1}. \tag{2.30}$$

Thus by measuring the ratio of red sideband and blue sideband excitation probability, it is possible to estimate the average phonon number of the ion after Doppler cooling. Using this measured value of the average phonon number and the observed excitation probability of the trapped ion, the experimental value of the Lamb-Dicke parameter can be obtained using Eq. 2.26, as is done in Chapter 5.

2.3.1 Free Evolution of a Qubit: Ramsey Interferometry

While Rabi oscillation is a driven phenomenon, Ramsey measurement is a free evolution of a two level system. Ramsey measurement is performed by applying two $\Pi/2$ pulses at resonance with an evolution time in between and a phase difference between the pulses dependent on the free evolution time. After applying the two pulses, the probability of excitation is measured. The probability of excitation oscillates with the free evolution time, with the frequency of oscillation depending on the

detuning of the laser from the resonance. The free oscillation of the qubit decays with time because of loss of phase coherence of the qubit due to interaction with the environment, especially stray magnetic fields. Ramsey measurement gives an insight into the free coherence time of the qubit and the quantum information retention capability of the system.

2.4 Conclusion

We have thus seen how we can prepare a trapped ions for experiments in the quantum regime. The radio frequency fields help to confine the ion in a limited space while laser cooling helps to bring the ion to the quantum regime and allows us probe the quantum dynamics of the ions external motion. The biggest advantage of trapped ion is that one can trap a single ion in space, isolated from the surroundings. This opens up several possibilities of high precision measurement because the system is no longer affected by uncontrolled interactions with other atoms or ions. While the trap potential can shift the D states of the ion via interaction between electric quadrupole and electric field gradient, it is a very well defined and well controlled potential, depending on a few electrical parameters and hence can be well adjusted to suit the needs of the experiment.

All these advantages makes trapped ions an excellent system to study the weakest signature of exotic interactions possible within an atom. In the rest of this work, we gear towards measurement of such properties of a trapped barium ion.

In the next chapter we discuss how our measurements are helpful towards measuring the atomic parity non-conservation in Ba$^+$. We also develop a framework to generate global phases on several trapped ions using electric quadruple interaction with the D-levels of barium ion. As these states have extremely narrow linewidth, it opens up a range of possibilities to study quantum dynamics and geometric phase generating interactions, framework for which is discussed in the following chapter.

Chapter 3

Light-Matter Interaction: Probing Electroweak Interactions and Symmetry Breaking

Now that we have established our basic system, let us discuss the science that can be performed using that system. Ion traps provide an extremely clean and controllable environment for quantum systems. Barium ion has long lived D states which are coupled to the ground state with dipole forbidden transitions [23–25]. This opens up several avenues to perform precision tests of fundamental interactions quantum manipulation of the D level using geometric phases.

Barium is a very good contender for atomic parity non-conservation measurements [26, 53, 54, 108]. These are tests of weak interactions but performed on atomic level and not using a massive collider. These effects scale as cube of the atomic number [50, 51] and thus for barium it is quite strong. Also since the D levels are long lived, it can allow one to probe small shifts arising from parity non-conserving interactions.

Apart from having a long lifetime (32 seconds and 80 seconds for two fine structure levels), the D levels also have an inherent quadrupole moment [26]. At it is shown here, this allows geometric phase generation via interaction with a time dependent electric field gradient.

In this chapter, we first discuss how parity non-conserving interactions can be measured for a

trapped barium ion. Then we move over to proposing a novel trap design which allows for geometric phase generation for trapped ions and how we can move the system from non-abelian evolution to abelian one via breaking the inherent symmetry of the system.

3.1   Measuring Exotic Atomic Interactions- Atomic Parity Non-Conservation (PNC) Measurements Protocol
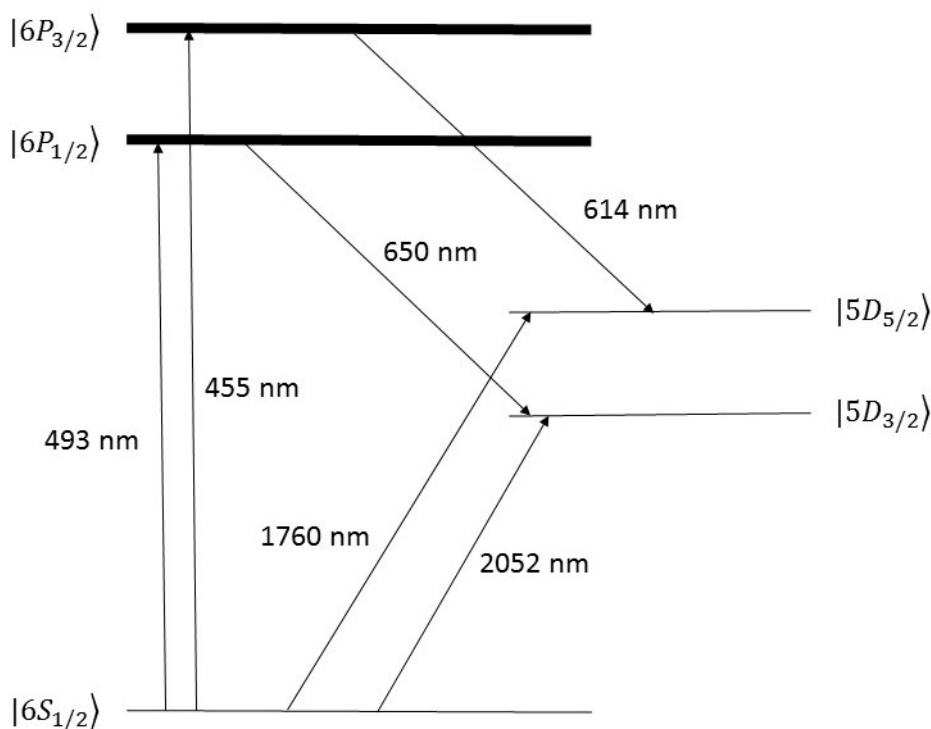
Figure 3.1: Relevant energy levels of a ^{138}Ba$^+$.

Parity-non conservation experiments look for breaking of parity symmetry in atomic systems. Parity symmetry implies that the mirror image of a system follow the same law of physics as the system itself. However, it has been seen that for electro-weak interaction, parity is not conserved [57]. Weak interaction, as the name suggests is extremely weak and only certain families of particles interact with each other via weak interaction. One of the possible interactions are lepton-hadron weak interaction. In an atomic system, hadrons are nucleons like protons or neutrons and electrons are leptons.

If one looks at the S level wavefunction, one can see that the wavefunction penetrates the nu-

cleus. This means that the electron 'spends' sometime inside the nucleus or in more technical term, there is a short range interaction between the nucleus and the electron. This leads to weak interaction between the electron and nucleons. Parity of wavefunctions govern the selection rules in atomic transitions. Ground state electron, because of selection rules, have a dipole forbidden transition with the D level. However, because of the weak interaction of the electron with the nucleus, the ground state of the Ba^+ ion acquires some odd-parity despite being a pure even-parity state. This allows for a small dipole coupling between the S-level and D-level. The goal is to estimate this parity violating coupling between the S and D levels.

3.1.1 Methodology and Required Parameters

$S_{1/2}$ **Zeeman**   **AC Stark**   **PNC LS**
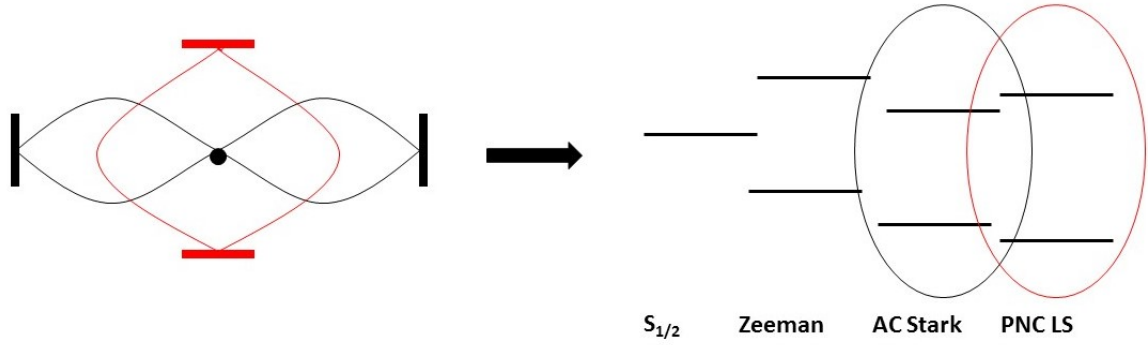
Figure 3.2: Scheme for measurement of atomic PNC.

The scheme for measuring atomic PNC relies on A.C. stark shift (shift of energy levels of an atom induces by off-resonant light) induced by electric field and electric field gradients on the $S - D$ transition [53]. As Fig. 3.2 shows, first the barium ion is held at the node of a standing wave. This leads to a AC stark shift because of the electric field gradient interacting with the transitional quadrupole between S and D levels. Then we switch on the second standing wave such that the ion is at the anti-node of the standing wave, where the electric field is maximum. Now, because of the small dipole coupling due to PNC between the S and D levels, it leads to a further shift of the levels. From measurement of these shifts along with some input parameters, one can obtain the PNC hamiltonian coupling S and D levels.

If one considers m and m' as the two zeeman sub-levels for S and D states, then the effective Rabi frequency between these two sub-levels are [50, 54]

$$|\Omega_{m'm}^2| = |\Omega_{m'm}^{quad} + \Omega_{m'm}^{pnc}|^2, \tag{3.1}$$

taking into account the contribution from the quadrupole and the PNC induced dipole transitions.

The Rabi frequency components can be broken down into-

$$\Omega_{m'm}^{quad} = -\frac{1}{2\hbar}\Sigma_i(\epsilon_{m'm}^{quad})_{ij}\Big(\frac{\partial E_i}{\partial x_j}\Big)_{r=0} \tag{3.2}$$

and

$$\Omega_{m'm}^{PNC} = -\frac{1}{2\hbar}\Sigma_i(\epsilon_{m'm}^{PNC})_i E_i(0). \tag{3.3}$$

Here $\epsilon_{m'm}^{PNC}$ is the matrix element arising from the parity non-conserving interaction. In terms of wavefunctions, the PNC matrix elements can be written as

$$\epsilon_{m'm}^{PNC} = \Sigma_n \frac{\langle D_{3/2}, m'| \, er \, |nP_{1/2}, m\rangle \langle nP_{1/2}, m| \, H^{PNC} \, |6S_{1/2}, m\rangle}{E_{6S_{1/2}} - E_{nP_{1/2}}}. \tag{3.4}$$

Here H^{PNC} is given as [50, 53]

$$H_{n\bar{n}}^{PNC} = i \, 1.8 \times 10^{-7} Z^2 Q_W K_r \frac{(W_n W_{\bar{n}})^{3/4} a_0^{1/2}}{(Z_{ion} + 1) \, e}. \tag{3.5}$$

K_r is a relativistic factor arising from the fact that electrons in heavy elements are moving at relativistic velocities in stable orbit. This factor for barium is approximately is 3. W_n and $W_{\bar{n}}$ are the electronic binding energies of the levels n and $\bar{n}$. The binding energy increases with the increase of the nuclear charge and hence heavier elements are better candidates for measurement of parity non-conserving effects. i comes from time reversal invariance requirements. Q_W is the weak charge and signifies the strength of weak interaction. It is given as $Q_W = Z(1 - 4 \sin^2 \theta_W) - N$ where $\sin^2 \theta_W = 0.230$ from particle collision measurements. The goal of the experiment is measurement of Q_W and to open an independent line of enquiry into weak interactions, via experiments performed at a different scale of energies.

If we look at Eq. 3.4, we will see that the primary requirement for estimating $\epsilon_{m'm}^{PNC}$ is very precise knowledge of the dipole matrix elements coupling the P and D levels. As a part of this thesis,

we performed high precision measurement of the dipole matrix element of the transition $6P_{1/2}$ to $5D_{3/2}$. This was done by precisely measuring the branching fraction for this transition and from existing knowledge of the lifetime of the $P_{1/2}$ level. The requirement of level of precision is less than 1% as the benchmark is set by the most accurate measurement in cesium atom [105] that can distinguish different alternatives of the Standard Model [50].

3.1.2 Branching Fraction Measurement
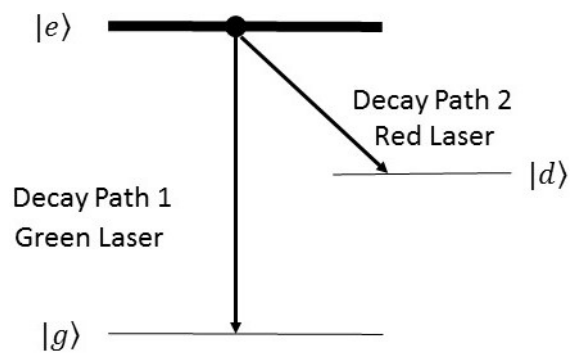
Figure 3.3: Level diagram for branching fraction measurement.

Branching fraction is the measure of the probability of an electron de-exciting via one path over another. Ideally, one excites the electron to the upper level and then observes the path by which it decays by measuring the wavelength of the photon which is emitted [55]. The process is repeated numerous times to obtain the branching fraction.

However, the above measurement process has some limitations. First of all, for dipole coupled excited states, the upper state lifetime is of the order of a few nanoseconds [100]. So from an experimental point of view that becomes a challenge to synchronize the experiment with such short time scales. Also it would require the use of pulsed lasers with sub nanosecond pulse widths to deterministically excite the electron and shut down the excitation laser because that would interfere with the photon count measurement. Pulse lasers, by the very nature of them, have large wavelength spread and thus can cause off-resonant excitation and affect the precision of the measured value. Continuous laser excitation and observation of optical nutation as performed by Davidson [111] provides the values of the branching fraction but with uncertainties dominated by model parameters such as

detuning, intensity, etc.

The second experimental difficulty comes from the fact that when measuring two separate wavelengths, it is hard to calibrate the detection efficiencies with high precision. The reason detection efficiencies play a huge role is the following:

Lets say the experiment is performed one million times and we want to see how many photons come via decay path 1 (which we call green photons) and how many via decay path 2 (which we call red photons), as shown in Fig. 3.3. Lets assume that the branching fractions are p_1 and p_2, which means out of one million experiments, $p_1 \times 1,000,000$ green photons are emitted and $p_2 \times 1,000,000$ red photons are emitted. However, because of detection efficiencies we will detect only a fraction of these two. Now without the precise knowledge of the detection efficiencies for each wavelength it is not possible to obtain the proper branching fraction by the ratio of the detected number of photons for each wavelength. This leads to additional uncertainty in the measurement of the branching fraction.

This scheme however can be improved by considering the fact that $p_1 + p_2 = 1$ [109]. And also by considering the following dynamics using a continuous beam laser, which allows us to eliminate the use of pulsed lasers.

Lets consider the level diagram shown in Fig. 3.3. First the green laser is turned on. In that scenario, the population dynamics is given as follows-

$$\dot{\rho}_{ee} = \frac{i\Omega(t)}{2}(\rho_{eg}(t) - \rho_{ge}(t)) - \Gamma\rho_{ee}(t), \tag{3.6}$$

$$\dot{\rho}_{gg} = \frac{i\Omega(t)}{2}(\rho_{ge}(t) - \rho_{eg}(t)) + p_1\Gamma\rho_{ee}(t) \tag{3.7}$$

and

$$\dot{\rho}_{dd} = p_2\Gamma\rho_{ee}(t). \tag{3.8}$$

Here ρ_{ii} is the population in the i th state and ρ_{ij} is the population transfer between the i, j th state. Physically, if the green laser is kept switched on, the electron will shuttle between $|g\rangle$ and $|e\rangle$ a few times and then decay into the $|d\rangle$ level, which is not optically driven to the $|e\rangle$ state. Thus finally

all the population will decay into the $|d\rangle$ state giving rise to the following equality

$$\int_0^\infty \dot{\rho}_{dd}(t) \, dt \; = \; 1. \tag{3.9}$$

Now the average number of spontaneous photons emitted is given by

$$<n>= \int_0^\infty \Gamma \dot{\rho}_{ee}(t) \, dt. \tag{3.10}$$

From Eq. 3.9, 3.10 and 3.8, we obtain

$$<n>= \frac{1}{1-p_1}, \tag{3.11}$$

where the fact $p_1 + p_2 = 1$ has been used. Now since the final photon emitted is not green but red, so the average number of green photons emitted, while the green laser is driving the transition is given as

$$N_g =<n> -1 = \frac{p}{1-p}. \tag{3.12}$$

Thus we have a relation between the number of green photons emitted while the population is pumped into $|e\rangle$ state using the green laser and the branching fraction along decay path $|e\rangle \rightarrow |g\rangle$.

Now if we pump out the population from the D level using a red laser, it will emit only one green photon before it decouples from the red laser. By counting that photon, we can estimate the detection efficiency of the green wavelength with extremely high precision because if we run the experiment a million times, we know that only one million green photons will be emitted during the entire process. So by counting the actual number of green photons that we detect during that time, we can obtain a very precise value of the green detection efficiency.

One of the underlying assumption of the above algorithm is that there is no decay from the $|d\rangle$ level to $|g\rangle$ level. This is true for barium ion where the meta stable states have lifetimes of the order of 30 seconds and thus during the experimental cycle, which usually lasts for a about a hundred microsecond, we can ignore the decay from $|d\rangle$ to $|g\rangle$. The advantage of this detection is that the measurement involves only one wavelength of light and it is completely independent of the detuning

and intensity of the probe laser. It has some systematics which will be discussed in detail in chapter 4.

This scheme will only apply for a Lamda-type system where the excited level decays into one ground state and one meta-stable state. The whole measurement algorithm will become more complicated for levels where it decays into two or more metastable levels. The details of such a measurement process is described in details in Tarun Dutta's thesis [114] where we performed branching fraction measurement of $6P_{3/2}$ level of the barium ion.

3.2 Quadrupole Transition and Quadrupole Moment of $5D_{5/2}$ level

For an atomic system interacting with an electromagnetic field, the transition between two levels $|\psi_1\rangle$ and $|\psi_2\rangle$ is governed by

$$\int \psi_1^*(x) T \psi_2(x) dx. \tag{3.13}$$

Now based on the symmetry of $|\psi_1\rangle$ and $|\psi_2\rangle$ as well as that of the transitional moment T, the integral can either vanish or have a non-zero value, the latter being an allowed transition. For atomic levels, that is solutions for spherically symmetric potentials, the parity of a state is given by $(-1)^l$, where l is th orbital quantum number of the states involved in the transition. For barium ion, thus the S level (l=0) have even parity, P (l=1) have odd and D (l=2) levels have even parity.

For a transition to take place, the integral must have a non-zero value, which is possible when the integrand has a even parity. The parity of the integrand also depends on the parity of the transitional moment. The dipole transition has an odd parity (depends on x, y and z), while quadrupole transition has even parity (depends quadratically on the dimensional variables). Thus for a transition between S and D levels, dipole pathway is forbidden while the quadrupole transition is allowed.

The coupling strength for the quadrupole transition [59, 60] is given by,

$$\Omega_{quad} = \left| \frac{eE_0}{2\hbar} \left\langle 6S_{1/2}, m \right| (\vec{\epsilon} \cdot \vec{r})(\vec{k} \cdot \vec{r}) \left| 5D_{5/2}, m' \right\rangle \right|, \tag{3.14}$$

where E_0 is the amplitude of electric field of the light, r is the spatial variable for the electron, $\vec{\epsilon}$ is the polarization vector, $\vec{k}$ is the wave vector of the light and m and m' are the zeeman sub-levels of

the S and D state. As can be seen, unlike dipole transition, where the dependence is linear in r, for quadrupole, it is quadratic in r.

Using Wigner-Eckart theorem, Eq. 3.14 can be written as [59, 60]

$$\Omega_{quad} = \left| \frac{eE_0}{2\hbar} \left\langle 6S_{1/2} \right| \left| r^2 C^{(2)} \right| 5D_{5/2} \right\rangle \sum_{\Delta m=-2}^{2} \begin{pmatrix} 1/2 & 2 & 5/2 \\ -m & \Delta m & m' \end{pmatrix} c_{ij}^{(\Delta m)} \epsilon_i n_j \right|, \qquad (3.15)$$

where $g^{(\Delta m)} = c_{ij}^{(\Delta m)} \epsilon_i n_j$ is the geometric contribution to the quadrupolar coupling strength between the S and D levels. Δm is the change of the magnetic quantum number for the transition between different zeeman levels (m and m'). For transition between $6S_{1/2}$, which has two zeeman sub-levels, $m = \pm\frac{1}{2}$, and $5D_{5/2}$, which has 6 zeeman sub-levels, $m = \pm\frac{1}{2}, \pm\frac{3}{2}, \pm\frac{5}{2}$, the allowed values for Δm are $\Delta m = 0$, $\Delta m = \pm 1$ and $\Delta m = \pm 2$. $\Delta m = \pm 3$ are not allowed because quadrupole coupling cannot cause angular momentum change of more than 2. Thus there are 10 allowed transitions between all the zeeman sub-levels of $6S_{1/2}$ and $5D_{5/2}$.

To calculate the geometric contribution to the coupling strength, let ϕ is the angle between the magnetic field and the 1760 nm laser beam and γ is the angle between the magnetic field and the polarization of the 1760 nm laser beam, the $g^{(\Delta m)}$ can be written as [59, 60]

$$g^{(0)} = \frac{1}{2} |\cos\gamma \sin 2\phi|, \qquad (3.16)$$

$$g^{(\pm 1)} = \frac{1}{\sqrt{6}} |\cos\gamma \cos 2\phi + i \sin\gamma \cos\phi|, \qquad (3.17)$$

$$g^{(\pm 2)} = \frac{1}{\sqrt{6}} \left| \frac{1}{2} \cos\gamma \sin 2\phi + i \sin\gamma \sin\phi \right|. \qquad (3.18)$$

Based on these relations, Fig. 3.4 shows the variation of the quadrupolar coupling strength with respect to the geometrical parameters of the system [59]. This variation of the coupling strength allows us to choose a particular transition set, given by the allowed value(s) of Δm by varying the laser polarization and the magnetic field direction. The beam direction is usually fixed and is determined by the setup geometry.

Other than having a quadrupole coupling with the ground state, the D levels also have inherent quadrupole moments. Because the D levels have even parity, like the quadrupole moment operator,
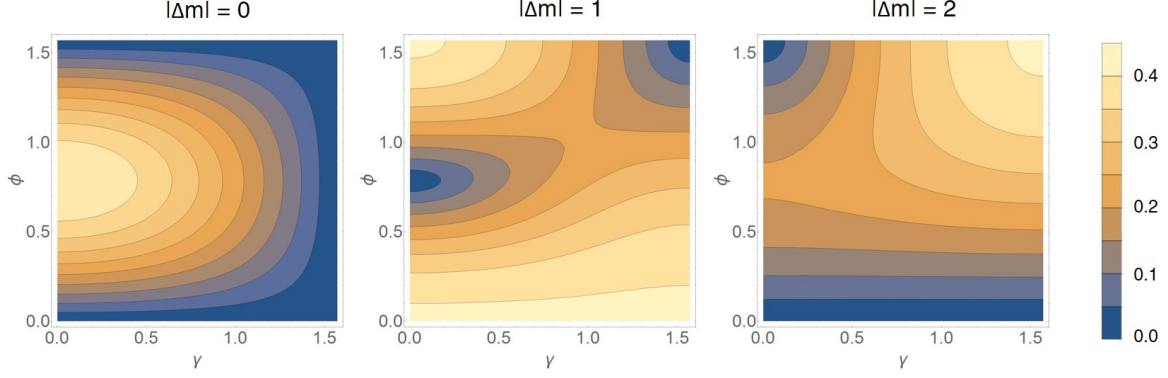
Figure 3.4: Figure showing variation of the coupling strength for transitions for different Δm values between the zeeman sub-levels of $6S_{1/2}$ and the $5D_{5/2}$ states with respect to the geometric parameters of the system.

and angular momentum greater than 1, these levels have a finite value of the quadrupole moment. Knowledge of the quadrupole moment of the levels opens up the possibility of estimating the wavefunction of barium D levels. This in turn fuels the theoretical models required to describe interacting multi-particle systems such as couple cluster theories. Apart from pinning down on models for many body theories, the quadrupole shift is an important shift for any optical ion clock, including Ba^+.

For an atomic level with angular momentum j, the quadrupole shift for a given zeeman level is given as [27, 56],

$$\Delta\nu = \frac{1}{4\hbar}\frac{dE_z}{dz}\Theta(D,j)\frac{j(j+1)-3m^2}{j(2j-1)}(3\,\cos^2\beta - 1), \qquad (3.19)$$

where $\Theta(D,j)$ is the inherent value of the quadrupole moment of the D level and $\frac{dE_z}{dz}$ is the electric field gradient along the z direction. β is the angle between the quantization axis, defined by the magnetic field and the principle axis of the electric field gradient, which in this case is the line joining the two end caps. Eq. 2.11 gives the electric field gradient experienced by a trapped ion due to the axial DC potentials as a a function of the axial trapping frequency of the ion.

Thus the equation governing the level shift due to quadrupole interaction becomes

$$\Delta\nu = \frac{1}{4\hbar}\frac{m\omega_z^2}{e}\Theta(D,j)\frac{j(j+1)-3m^2}{j(2j-1)}(3\,\cos^2\beta - 1). \qquad (3.20)$$

For our trap, the measured value of ω_z for end cap voltage of 1000 V is about 1.5 MHz. Using the theoretical value of quadrupole moment of barium ion [26], we can estimate that the shift of the

level due to quadrupolar interaction is of the order of 200 Hz. Thus we need to be able to develop laser system having linewidth and stability of less than 200 Hz. Development and experiments with such a system is described in chapters 3 and 5.

3.3 Geometric Phase

Geometric phase originates due to cyclic time evolution of an Hamiltonian. This phase can be distinguished from the usual dynamical phase by its dependence on the quantum level structure of the system and the form of the time evolution of the involved Hamiltonian. Although geometric phase depends on the quantum level structure, it is independent of the energy eigenvalues. Therefore it is largely conceived as immune to external perturbations and hence a good quantum computation resource [74–78]. Any quantum computation at its basic level requires quantum gates for both single and two qubits. In order to perform reliably as a component of a quantum computation system, these quantum gates needs to have an error generation probability of 10^{-4}, which is known as fault tolerant threshold (FTT) [79]. So far the only single qubit operation that has shown such kind of FTT is based on an ion trap experiment [80] . Lemmer *et. al* [81] proposed a protocol based on spin phonon interaction which has the potential to beat the FTT. However, their analysis is specific to the proposed qubit system. Geometric phase, being inherently robust to external field fluctuations, provide a likely resource which can be exploited to create quantum gates having such FTT.

In general, the robustness of geometric phase is an inherent property of the mechanics itself. Therefore understanding the origin of such robustness in the context of geometric phase in spin system can allow for more controllability on such geometric phase gates. Any universal quantum computation will need single and two qubit gates which are both Abelian and non-Abelian in nature [74]. In most cases, studies on geometric phases are restricted to either of these two regimes [82–85]. Here we put forward a study in which we can go from Abelian to non-Abelian regime in the same spin system by slowly breaking the symmetry of the system. Analysis of such a system not only provides insights into the underlying physical processes governing each of the limits but also effectively probes the limits of the adiabatic theorem [86], [87] and the relation of adiabaticity and non-abelian behaviour. This is relevant as most of the quantum states are operated in the super-adiabatic regime [88]. Our analysis also provides room for identifying the relevant parameters which influence the phase fluctuation in different regimes.

3.4 Symmetry Breaking: Non-Abelian to Abelian

3.4.1 Theory

A quantum system, with a time dependent Hamiltonian which evolves implicitly and adiabatically with time, acquires an extra geometric phase, on top of its dynamical phase. In [69], Berry formulated the form of this geometric phase under adiabatic approximation as

$$\mathcal{G}_n = i \oint \langle \psi_n | \nabla_r | \psi_n \rangle \, dR \qquad (3.21)$$

for the nth eigenstate. The quantity $\gamma_n = \langle \psi_n | \nabla_r | \psi_n \rangle$ is called the gauge of the evolution because it remains invariant under any similarity transformation, except those involving the variable of the evolution themselves. This definition of the 'scalar' gauge holds only for non-degenerate levels. For degenerate levels, because multiple eigenstates belong to the same energy level, the definition is generalized to a matrix gauge $\gamma_{mn} = i \langle \psi_m | \nabla_r | \psi_n \rangle$, where m and n belong to the degenerate subspace [63], [89].

The adiabatic form of geometric phase can also be derived from the adiabatic theorem. The probability amplitude of an eigenstate belonging to a time dependent Hamiltonian varies as

$$\dot{C}_m = -C_m \left\langle \psi_m \Big| \dot{\psi_m} \right\rangle - \sum_{n \neq m} C_n \frac{\langle \psi_m | \dot{H} | \psi_n \rangle}{E_n - E_m} \, e^{i(\xi_n - \xi_m)}, \qquad (3.22)$$

where the states m and n are non-degenerate and ξ_m and ξ_n are the dynamical phases. The above equation governs the time dependence of the probability amplitudes of the states, beyond the dynamical contribution. Under adiabatic approximation, $\langle \psi_m | \dot{H} | \psi_n \rangle \ll (E_n - E_m)$ and hence the second term in Eq. 3.22 can be neglected in comparison to the first term. Thus for adiabatic evolution, there is no 'mixing' of the different eigenstates. However, as a consequence of the time dependence of the Hamiltonian, there is an additional phase, on top of the dynamical phase, governed by $\left\langle \psi \Big| \dot{\psi} \right\rangle$. Under the conditions of implicit time dependence, this term leads to the underlying gauge of geometric phase as derived by Berry.

This opens up a wide range of possibilities. Now the system is no longer restricted to phases generated by fundamental interaction but by engineering different state evolution, any phase (gauge) can be imposed onto the system. This leads to the term 'artificial gauge'. Now, depending on the system and the interaction, this artificial gauge can be commuting with each other or non-commuting. When the gauge is commuting, it is called an Abelian gauge and when it is non-commuting it is called a non-abelian gauge.

Abelian evolution corresponds to evolution without any population transfer. For a non-degenerate set of levels, under adiabatic condition, all evolutions are Abelian, since adiabaticity guarantees lack of population transfer or mixing. Degenerate levels can also have Abelian evolutions, if the underlying gauge matrix corresponding to the degenerate subspace is diagonal.

On the contrary, non-Abelian evolutions inherently introduces mixing of states or population transfer between the states. For a degenerate subspace, if the off-diagonal elements of the gauge matrix are nonzero, then the evolution is considered as non-Abelian [63], [89]. However, degeneracy itself does not guarantee non-zero off diagonal elements. A subspace of non-degenerate levels, under certain evolutions can have non-zero off diagonal elements. However, conditions imposed by adiabaticity does not leave room for population transfer in such cases and the off-diagonal elements have no physical significance under such conditions. This can be easily demonstrated from Eq. 3.22 as the coupling term drops off because of finite strength of the oscillatory function and the relatively smaller coupling strength in the adiabatic limit.

3.4.2 Non-Abelian to Abelian Changeover

Now that we have establish that there two types of evolution, the natural question is whether it is possible to transfer smoothly from one form of evolution to another and what is the dynamics of the system when such a change over is taking place. To achieve this, we need an evolution with degeneracies and focus on non-Abelian degenerate subspaces. Now, if we introduce non-degeneracy into the system, without changing the underlying geometry and hence the gauge matrix of the evolution, then we can observe the physical significance of the off-diagonal elements slowly diminishing and vanishing in the Abelian regime. Geometry in this context implies the implicit parameters via which

the Hamiltonian was changing with time. Thus the primary goal in this thesis is to study the dynamics of the off-diagonal elements with respect to the symmetry breaking field. This also allows us to probe the Adiabatic theorem the limits of which, under the influence of a symmetry breaking field has long been debated [86], [87]

.

3.5   The System

A trapped barium ion interacting with electric multipoles provides the basic system under consideration. The quadrupole moment of the D level of the barium ion, interacting with a time varying electric field gradient provides the basic system which is required to study the geometric phase evolution and the effect of symmetry breaking in such a system. The time dependent interaction is induced by a variation of the electric field gradient observed by the trapped ion. The time dependence is such that the principle axes describe a conical path about the degeneracy point as shown in Fig. 3.5. The spin $3/2$ interacting with the electric field gradient maintains a time reversal symmetry and hence there are Kramer's degeneracies in the system, i.e., $|\pm 1/2\rangle$ and $|\pm 3/2\rangle$ states form two pairs of degenerate subspaces. The Hamiltonian of quadrupole interaction, as is shown in Eq. 3.23 has $\hat{S}_+^2$ terms and hence couples the $|\pm 1/2\rangle$ substates. Thus the $|\pm 1/2\rangle$ subspace undergoes non-Abelian evolution. The Hamiltonian however cannot couple $|\pm 3/2\rangle$ states, which have a $\Delta m = 3$ and thus cannot be coupled by the quadratic terms in angular momentum operator. Hence the $|\pm 3/2\rangle$ subspace undergoes Abelian evolution. This however is true only within quadrupole approximation which limits the field expansion to S^2 terms.

To induce the non-Abelian to Abelian transition, we now apply a time dependent magnetic field along with the electric field gradient. The magnetic field lifts the Kramer's degeneracy of the system and hence drives the system away from non-Abelian behaviour. However, for a true changeover from non-Abelian to Abelian, the underlying gauge is required to be the same in the presence of the magnetic field. This is achieved by making the magnetic field rotate along with the electric field gradient. This preserves the 'geometry' of the system even in the presence of the magnetic field as the quantization axis remains unchanged. 'Geometry' in this context implies the transformation which connects the diagonal basis of the Hamiltonian with the stationary basis. Because of this constancy of 'geometry', the underlying gauge of the evolution remains invariant. The geometry preservation
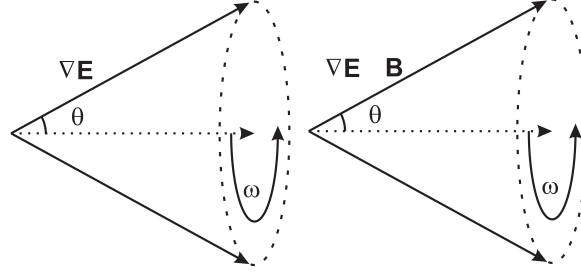
Figure 3.5: Configuration of the applied electric field gradient and magnetic field for inducing non-Abelian to Abelian symmetry breaking. In the adiabatic regime, for the $|\pm 1/2\rangle$ substates, absence of magnetic field is non-Abelian while non-zero magnetic field gives rise to Abelian evolution.

is also ensured by the fact that symmetry breaking Hamiltonian commutes with the non-Abelian Hamiltonian. This allows us to describe the system in both Abelian and non-Abelian regime using the same eigenbasis, which to avoid ambiguity, is taken as the eigenbasis of the Hamiltonian in the Abelian regime. In the following sections a detailed theoretical description of the system's evolution under the influence of the time varying field is derived.

3.5.1 Non-Abelian Regime

The quadrupole moment of the spin $3/2$ system interacting with an electric field gradient gives rise to the non-Abelian geometry for the $|\pm 1/2\rangle$ subspace. The Hamiltonian for a quadrupole moment-electric field gradient interaction is given as

$$H_Q = \frac{1}{6} Q_{ij} \frac{\partial E_i}{\partial x_j}, \tag{3.23}$$

where Q_{ij} is the ijth component of the quadrupole moment and is defined for spin systems as $Q_{ij} = c(\frac{1}{2}(S_i S_j + S_j S_i) - \frac{1}{3}\vec{S}^2 \delta_{ij})$. $\frac{\partial E_i}{\partial x_j}$ is the ijth component of the electric field gradient tensor.

In our case, because of a suitable choice of the principle axes, only the $\frac{\partial E_z}{\partial z}$ component of the electric field gradient tensor contributes to the Hamiltonian of the system. Thus, in the non-Abelian regime, we obtain an effective Hamiltonian given by,

$$H_{NA} = c(S_{z'}^2 - \frac{1}{3}S^2), \tag{3.24}$$

where $S_{z'} = S_x \sin\theta\cos\phi + S_y \sin\theta\sin\phi + S_z \cos\theta$, c being the strength of interaction and $\phi = \omega t$, ω being the rotational frequency of the electric field gradient.

45

The eigenstates of this Hamiltonian are doubly degenerate as electric field preserves Kramer's degeneracy between the Zeeman levels. The two doubly degenerate subspaces consists of $\left|\pm\frac{3}{2}\right\rangle$ corresponding to eigenvalue c and $\left|\pm\frac{1}{2}\right\rangle$ corresponding to eigenvalue $-c$. To obtain the gauge matrices corresponding to these sets of states through the relation $\gamma_{mn} = i\left\langle\psi_m\right|\nabla_r\left|\psi_n\right\rangle$, the wavefunctions in the stationary frame are required. Starting from the diagonal Hamiltonian in the rotating frame, we use Wigner-D matrices to obtain the laboratory frame Hamiltonian. The respective gauge matrices in the laboratory frame are-

$$\gamma_{\pm3/2} = \begin{pmatrix} \frac{3}{2}\cos\theta & 0 \\ 0 & -\frac{3}{2}\cos\theta \end{pmatrix}$$

and

$$\gamma_{\pm1/2} = \begin{pmatrix} \frac{1}{2}\cos\theta & \sin\theta \\ \sin\theta & -\frac{1}{2}\cos\theta \end{pmatrix}$$

.

From these matrices, we can see that for the subspace $\left|\pm\frac{1}{2}\right\rangle$, we have non-zero off-diagonal elements. Hence the degenerate subspace $\left|\pm\frac{1}{2}\right\rangle$ follows non-Abelian evolution. In the non-Abelian regime, the eigengauge is given by the eigenvalues of the gauge matrix, $\pm\frac{1}{2}\sqrt{4 - 3\cos^2\theta}$. For $\left|\pm\frac{3}{2}\right\rangle$, the off-diagonal elements are zero, implying that the states are not mixed by the interaction and thus they experience Abelian evolution.

3.5.2 Abelian Regime

To transfer the system from non-Abelian regime to Abelian regime, we apply a symmetry breaking magnetic field. However, to make any comparison between the two situations, we require the 'geometry' of the system to remain invariant in the presence of the magnetic field. More precisely, the connection between the diagonal basis and the stationary frame, which is the Wigner D matrices, should remain the same in the presence or absence of the magnetic field.

The Hamiltonian in the Abelian regime obtained by the application of the magnetic field in the

46

direction of the electric field gradient is given by

$$H_A = c(S_{z'}^2 - \frac{1}{3}S^2) - bS_{z'}. \tag{3.25}$$

The eigenvalue of the $\left|\pm\frac{1}{2}\right\rangle$ subspace now becomes $-c \mp \frac{1}{2}b$. However, the gauge matrices remain unchanged. In the Abelian configuration, the adiabatic theorem leads us to conclude that the off diagonal elements of the gauge matrix corresponding to this set of states, do not contribute to any physical observable including geometric phase. In this regime, the underlying gauge is simply $\pm\frac{1}{2}\cos\theta$ corresponding to the two states.

3.5.3 Non-Abelian to Abelian Changeover

In the two regimes, the states, $\left|\pm 1/2\right\rangle$, are governed by two different underlying gauges given by $\pm\frac{1}{2}\sqrt{4 - 3\cos\theta^2}$ for non-Abelian and $\pm\frac{1}{2}\cos\theta$ for Abelian. The physical manifestation of the gauges is obtained through phase dependent energy shifts. When a system continuously acquires phase, then it manifests itself in the form of shifted energy level. If the rate of phase acquisition is ϕ, then the shift of the energy level is given by $\hbar\phi$. Now, for the geometric phase, if the phase acquired per cycle of evolution is ϕ_g, the gauge of that evolution is γ_n and the implicit variable, as defined in Eq. 3.21, varies with time as $R(t) = \omega t$, then the rate of phase acquisition is given by $\gamma_n\omega$. Thus the shift of the energy level, which is equal to the rate of phase acquisition, is directly proportional to the gauge of the evolution as well as the frequency. Now when the system moves from non-Abelian to Abelian evolution, the gauge of the transformation changes and thus the variation of the energy level shifts, on top of the energy eigenvalue, while going from non-Abelian to Abelian is the primary signature of such a transition.

In the true adiabatic regime ($\omega \to 0$), even the smallest value of b will drive the system away from non-Abelian to Abelian. However, for finite values of ω, the system is governed by two timescales, one depends on ω, the rotational frequency of the fields and the other depends on b, which determines the splitting between the $\left|\pm 1/2\right\rangle$ states. For a finite ω, the Abelian regime can only be achieved for $b \gg \omega$.

3.6 Dressed State Calculations

Unlike the systems studied so far, the system presented here allows a well controlled symmetry breaking field within the same similarity group, thus probing the system evolution at the boundary of commuting and non-commuting basis. In the previous section we have seen that by changing the system from non-Abelian to Abelian regime, the off-diagonal elements loses their physical significance. Continuous tunability of our system allows us to investigate the dynamics of the off diagonal elements with respect to symmetry breaking magnetic field. As it turns out these off-diagonal terms plays an important role in the assumptions of adiabatic theorem.

For studying the dynamics of the off diagonal elements, we begin at the basic Eq. (3.22) governing the evolution of two states. Working with the $|\pm 1/2\rangle$ subspace, we assume that ω is small compared to c such that we can neglect the coupling between $|\pm 1/2\rangle$ and $|\pm 3/2\rangle$ subspaces. By plugging in the values of the variables, the time evolution for the $|\pm 1/2\rangle$ substates are given by

$$\begin{pmatrix} \dot{C_1} \\ \dot{C_2} \end{pmatrix} = i \begin{pmatrix} \frac{\omega}{2}\cos\theta & \omega\sin\theta \, e^{ibt} \\ \omega\sin\theta \, e^{-ibt} & -\frac{\omega}{2}\cos\theta \end{pmatrix} \begin{pmatrix} C_1 \\ C_2 \end{pmatrix}. \tag{3.26}$$

For $b = 0$, Eq. 3.26 governs the behaviour in the non-Abelian regime. Therefore

$$\mathcal{H} = \begin{pmatrix} \frac{\omega}{2}\cos\theta & \omega\sin\theta \, e^{ibt} \\ \omega\sin\theta \, e^{-ibt} & -\frac{\omega}{2}\cos\theta \end{pmatrix} \tag{3.27}$$

is like an effective Hamiltonian governing the evolution of the states $\left|\pm\frac{1}{2}\right\rangle$ for a given value of ω and b.

3.6.1 Application of Dressed State Method

The dressed state approach, which is a derivative of the Floquet Theorem of differential equations with periodic co-efficients, takes into account the full time dependence and allows us to obtain the true eigenvalues, considering all the effects of the time dependence. Even though it was first developed to deal with atom photon interaction, it can be generalized to any equation with periodic co-efficients. For a detailed description of the mathematical algorithm applied here to obtain the

eigenvalues of Eq. (3.27), please refer to [66].

The eigenvalues obtained using the dressed state method provides the complete picture including the effect of phase dependent energy shifts of the levels. It also allows us to obtain the complete dependence of the geometric phase on b and ω and thus letting us to probe not only the limiting cases but the entire behaviour.

(a)

(b)

(c)

(d)
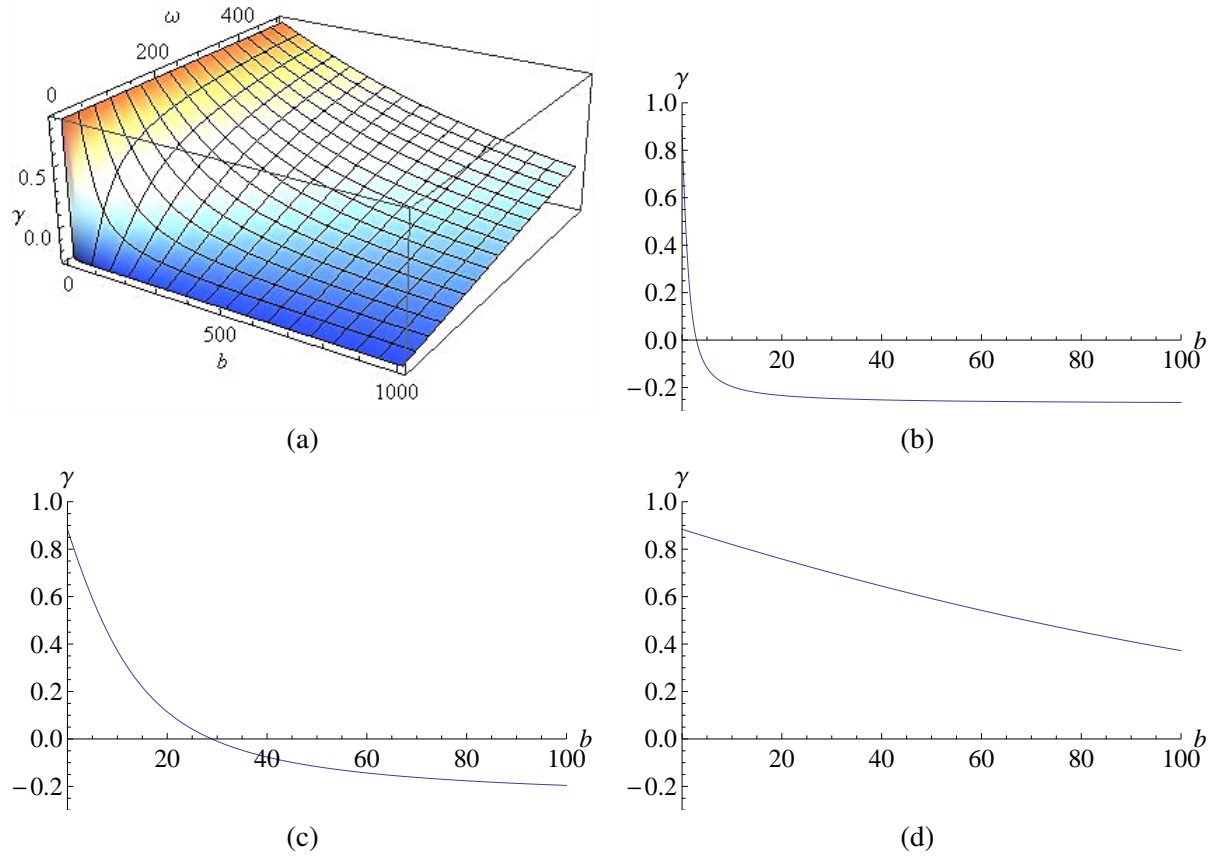
Figure 3.6: Figure demonstrates the non-Abelian to Abelian symmetry breaking. Figure (a) depicts the three dimensional dependence of the gauge on b and ω. Figures (b),(c) and (d) show the behaviour of the system moving away from the non-Abelian point for angular frequencies of 1, 10 and 100 Hz. As can be seen, with increase of rotational frequency, the transition of the system becomes slower. The non-abelian behaviour is 'retained' for higher values of magnetic field for a higher angular frequency, the figure also demonstrates that by selecting appropriate values of b and ω, we can control the behaviour of the system precisely, with the phase acquired defined only by the pair of values of b and ω. For these graphs, the value of θ is kept as 57.3^o. Magnetic field b and angular frequencies ω are expressed in Hz.

To apply the dressed state method, we assume an ansatz of the form

$$\begin{pmatrix} C_1(t) \\ C_2(t) \end{pmatrix} = \begin{pmatrix} \alpha_1(t)e^{-i\omega_+ t} \\ \alpha_2(t)e^{-i\omega_- t} \end{pmatrix}. \tag{3.28}$$

Now by inserting Eq. 3.28 into Eq. 3.26, we obtain the following equation for α_1 and α_2

$$i\begin{pmatrix} \dot{\alpha_1} \\ \dot{\alpha_2} \end{pmatrix} = \begin{pmatrix} -\frac{\omega}{2}\cos\theta - \omega_+ & -\omega\sin\theta \, e^{i(b+\omega_+ - \omega_-)t} \\ -\omega\sin\theta \, e^{i(b+\omega_+ - \omega_-)t} & \frac{\omega}{2}\cos\theta - \omega_- \end{pmatrix}\begin{pmatrix} \alpha_1 \\ \alpha_2 \end{pmatrix}. \tag{3.29}$$

Now if we choose $\omega_\pm = \mp\frac{b}{2}$, then the above 2×2 matrix becomes time independent and all the information about the time dependence of the system becomes encoded in behaviour of $\alpha_1(t)$ and $\alpha_2(t)$. Such a choice of the values of $\omega_\pm$ converts the above equation into a time independent problem, with an effective Hamiltonian given by

$$\mathcal{H}_D = \begin{pmatrix} -\frac{\omega}{2}\cos\theta + \frac{b}{2} & -\omega\sin\theta \\ -\omega\sin\theta & \frac{\omega}{2}\cos\theta - \frac{b}{2} \end{pmatrix}. \tag{3.30}$$

The Hamiltonian in Eq. 3.30 is the dressed form of the effective Hamiltonian given by Eq. (3.27). The advantage is that we converted the time dependent problem into an effective time independent problem thus allowing us to capture the complete behaviour of the system through the eigenvalues of the dressed Hamiltonian.

Solving Eq.3.30, we obtain the eigenvalues as $\pm\frac{\omega}{2}\sqrt{4\sin\theta^2 + \cos\theta^2 + (\frac{b}{\omega})^2 - 2\cos\theta\frac{b}{\omega}}$. The complete solution for C_1 and C_2 is given by

$$\begin{pmatrix} C_1 \\ C_2 \end{pmatrix} = \begin{pmatrix} C_1(0)e^{-i\lambda t} \\ C_2(0)e^{+i\lambda t} \end{pmatrix}, \tag{3.31}$$

where,

$$\lambda = \frac{\omega}{2}\left(\sqrt{4\sin\theta^2 + \cos\theta^2 + (\frac{b}{\omega})^2 - 2\cos\theta\frac{b}{\omega}} - \frac{b}{\omega}\right). \tag{3.32}$$

Here λ represents the phase dependent energy shift of the levels. As can be seen, this shift is of the form $\gamma_n\omega$, n being the nth eigenstate. In the pure non-Abelian or Abelian regime, the value of γ_n is independent of b or ω.

To obtain the non-Abelian limit, we put $b = 0$ and obtain the familiar non-Abelian gauge eigenvalues given by

$$\pm\sqrt{4 - 3\cos^2\theta}.$$

We can reach the Abelian limit by putting $\omega \to 0$ for any value of $b \neq 0$. However, physically, the exact value of ω required to reach the Abelian limit, depends on the value of b and hence a more suitable limit for the Abelian regime is $\frac{b}{\omega} \gg 1$. In this limit, the gauge tends to

$$\pm\frac{1}{2}\cos\theta. \tag{3.33}$$

As we can see in the Abelian or the non-Abelian limit, the gauge is independent of b and ω and is dependent only on the geometric parameters of the system. However, in the intermediate region, it is dependent on both b and ω, as is shown by Eq. 3.32.

It should be mentioned here that the choice of $\omega_\pm = \pm\frac{b}{2}$ is also a valid choice of the ansatz. However, this choice represents an opposite sense of rotation of the fields. Therefore this alternative choices corresponds to a difference of π of the angle between ω and b.

3.7 Perturbative Analysis for Intermediate Region

In the previous section, we have obtained the complete behavior of the system. However, the dressed state approach do not reveal the underlying physical phenomenon governing the intermediate regime. The physical processes, that is the system dependence on external parameters, controlling the two limits is however known. Now to obtain the physics of the intermediate regime, we approach perturbatively from the two well defined limits, where either $b = 0$ or $\frac{b}{\omega} \gg 1$ and try to identify the physical processes driving the system away from the two limits.

In this section our goal is to capture the response of the system due to small changes in system parameter (b or ω) from its two extreme limits. The key point is a suitable perturbation parameter for the Hamiltonian in the two regimes. As the non-Abelian and Abelian regimes are very different in nature one should not expect to use the same unperturbed Hamiltonian to describe both. Starting from the 'dressed' unperturbed Hamiltonian, the perturbation parameters are identified for Abelian and non-Abelian regimes.

3.7.1 Abelian Limit

The Abelian limit corresponds to the situation where $b \gg \omega$. In this condition, the phase dependent energy shift is given by $\frac{\omega}{2}\cos\theta$. The effective time independent Hamiltonian which can describe this system, including the phase dependent energy shifts, can be written as

$$H_D^A = \begin{pmatrix} \frac{1}{2}\cos\theta\,\omega - \frac{b}{2} & 0 \\ 0 & -\frac{1}{2}\cos\theta\,\omega + \frac{b}{2} \end{pmatrix} \tag{3.34}$$

Now to study the deviation of the system from the Abelian limit, we rewrite the total dressed Hamiltonian as

$$\mathcal{H}_D = H_D^A + \delta H_D^A,$$

where $\delta H_D^A = \mathcal{H}_D - H_D^A$ is the perturbing Hamiltonian. The form of δH_D^A comes out as

$$\delta H_D^A = \begin{pmatrix} 0 & \omega\sin\theta \\ \omega\sin\theta & 0 \end{pmatrix}. \tag{3.35}$$

Now we calculate the terms of the perturbation series using $\frac{b}{\omega}$ as perturbation parameter. The first order contribution of this perturbation being zero, the leading order term of the perturbation series is the second order contribution which is

$$E_D'' = -\frac{\sin^2\theta}{\cos\theta - \frac{b}{\omega}}. \tag{3.36}$$

As the perturbation series reveals, the 'non-Abelian' perturbation does not effect the energy levels of the unperturbed states, Eq. 3.36. However, it causes a population transfer between the eigenstates as is given by a non-zero second order term. We also notice that decreasing the value of $\frac{b}{\omega}$, which we know takes the system away from Abelian behaviour, also increases the coupling between the two states.

This perturbation however fails when $\frac{b}{\omega}$ approaches $\cos\theta$. This is because for $b = \omega\cos\theta$, the second order contribution has a singularity. This point indicates a deviation of the guiding physics
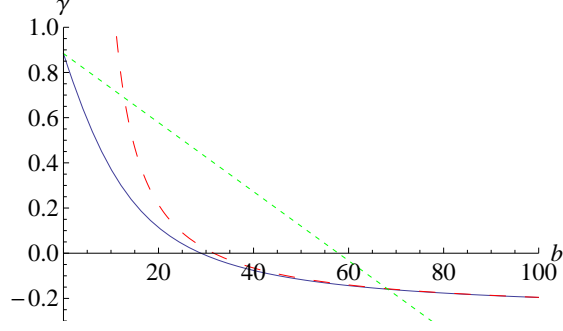
Figure 3.7: The figure depicts the results of the perturbative analysis with respect to the exact behaviour. The dashed line corresponds to the perturbation in the abelian regime. As can be seen, the perturbation mimics the exact behaviour till it reaches close the $b = \omega \cos \theta$ limit of the perturbation. The dotted line denotes the perturbation in the non-Abelian regime. As can be seen, the second order perturbation in this regime does not have a strong correspondence with the exact behaviour. This hints towards significant contribution from higher order perturbation terms, which is beyond the scope of this work. For this graph $\theta = 57.3^0$ and $\omega = 10$ Hz.

from the Abelian behaviour. For $b > \omega |\cos \theta|$, the Hamiltonian decomposition used above holds true.

3.7.2 Non-Abelian Limit

The non-Abelian limit corresponds to $b \ll \omega$. At the non-Abelian limit, that is $b = 0$, the phase dependent energy shift is given by $\frac{\omega}{2} \sqrt{4 - 3 \cos^2 \theta}$. The non-Abelian Hamiltonian is given by

$$H_D^{NA} = \begin{pmatrix} \frac{1}{2} \cos \theta \omega & \sin \theta \omega \\ \sin \theta \omega & -\frac{1}{2} \cos \theta \omega \end{pmatrix} \tag{3.37}$$

We again write the total dressed Hamiltonian as

$$\mathcal{H}_D = H_D^{NA} + \delta H_D^{NA}$$

where $\delta H_D^{NA} = \mathcal{H}_D - H_D^{NA}$ is the perturbing Hamiltonian in the Non-Abelian limit. δH_D^{NA} is given as

$$\delta H_D^{NA} = \begin{pmatrix} -\frac{b}{2} & 0 \\ 0 & +\frac{b}{2} \end{pmatrix}. \tag{3.38}$$

Now we calculate the perturbating terms using the perturbation parameter b. We find now that unlike the Abelian limit, in this case, the first order perturbation is non-zero whereas the second order contribution is zero. The first order contribution is given as

53

$$E'_D = \frac{b}{\omega} \frac{\cos\theta}{2\sqrt{4 - 3\cos^2\theta}}. \tag{3.39}$$

This series illuminate the fact that in the deviation of the system from non-Abelian behaviour, level shift plays the major role. The increasing energy gap between the levels however leads to a reduced rate of population transfer and thus drives the system away from the non-Abelian behaviour.

3.7.3 Sensitivity of Geometric Phase to Parameter Fluctuations

Having explored both the regions perturbatively, we can now analyze the influence of fluctuations of different external parameters on the geometric phase.

To develop a general framework, let us assume that

$$b' = b + \delta b \tag{3.40}$$

and

$$\omega' = \omega + \delta\omega \tag{3.41}$$

where δb and $\delta\omega$ are the fluctuations of b and ω respectively. The phase at the two extremes, that is the Abelian and non Abelian limits are independent of the values of b and ω. However in the intermediate regime, it is dependent on these parameters. In general, we can write the phase as follows

$$\gamma(b,\omega) = \gamma_0 + \gamma'(b,\omega) \tag{3.42}$$

where γ_0 is either the Abelian or non-Abelian phase and $\gamma\prime$ is the deviation from zero in each regime. γ_0 is independent of ω and b in both the limits.

Now to study the effect of fluctuation of each parameter on the geometric phase, we apply the substitutions of Eq. 3.40 and 3.41 and obtain

$$\gamma(b',\omega') = \gamma_0 + \gamma'(b,\omega) + \frac{\partial\gamma'}{\partial\omega}\delta\omega + \frac{\partial\gamma'}{\partial b}\delta b \tag{3.43}$$

The effect of the fluctuations of these parameters on the geometric phase are obtained through

$\frac{\partial \gamma^{'}}{\partial \omega}$ and $\frac{\partial \gamma^{'}}{\partial b}$.

In the Abelian limit assuming $\frac{b}{\omega} \gg 1$, we obtain

$$\frac{\partial \gamma^{'}}{\partial \omega} = \frac{\sin^2 \theta}{b} \tag{3.44}$$

and

$$\frac{\partial \gamma^{'}}{\partial b} = \frac{\omega \sin^2 \theta}{b^2}. \tag{3.45}$$

Similarly, for Non-Abelian limit $\frac{\omega}{b} \ll 1$,

$$\frac{\partial \gamma^{'}}{\partial \omega} = \frac{b \cos \theta}{2\omega^2 \sqrt{4 - 3\cos^2 \theta}} \tag{3.46}$$

and

$$\frac{\partial \gamma^{'}}{\partial b} = \frac{\cos \theta}{2\omega \sqrt{4 - 3\cos^2 \theta}}. \tag{3.47}$$

From the above four equations, depicting the effect of fluctuation of parameters on the geometric phase, it is evident that the role of ω and b are interchanged in the non-Abelian and the Abelian limits. While the non-Abelian limit is more sensitive to magnetic field fluctuations, the Abelian limit on the other hand is more sensitive to fluctuations of the angular frequency of their linear dependence on magnetic field and angular frequency respectively.

Experimentally usually magnetic field noise is one of the biggest source of dephasing for quantum systems as we will see in Chapter 5. From that point of view, we can say that the phase fluctuations due to magnetic field noise will be much higher in the non-Abelian regime than compared to the Abelian regime and thus the Abelian limit is much more robust against fluctuation of magnetic field. However, if in a certain situation, robustness against rotational frequency is required, then non-Abelian limit is a much better choice than Abelian limit.

3.8   Modified Ion Trap Design for Geometric Phase Generation

In this section we propose a concrete experiment where we it is possible to observe such phase dependent energy shifts using a single trapped ion. The trap is modified to impose a cyclic Hamiltonian on the ion and we can observe the resultant shift in the electronic levels of the trapped ion. The interaction by which we propose to impose such a time dependent Hamiltonian is the interaction of the quadrupole moment of some chosen electronic levels with a time dependent electric field gradient, provided by a modified trap geometry. To the best of our knowledge, the only experimental observation of similar splitting and shift has been by R. Tycko [68] who used a single crystal of $KClO_3$, where the crystal field gradient interacted with the nuclear quadrupole moment and the time dependence has been incorporated by mechanical rotation of the crystal. The proposed experiment using a single trapped ion however is fundamentally different in two ways. First, the electronic state of the ion allows the manipulation of the Hamiltonian by light field. Second, the presence or absence of static magnetic field allows the system to change between Abelian and non-Abelian geometry. This changeover from one regime to another has so far not been studied either experimentally or theoretically. In this section the effect of the modified trap geometry on the ions energy levels are estimated based on the electric field gradient- electric quadrupole moment interaction.

The interaction for a trapped ion with the electric field gradient is defined by Eq. 3.23. The pre-factor c in Eq. 3.24 contains the value of the electric field gradient and the quadrupole moment of the state under study. For a spin $\frac{3}{2}$ state, which represents the angular momentum of $5D_{\frac{3}{2}}$ state of a trapped Ba+ ion, the eigenvalues for this Hamiltonian are $c\hbar^2$ and $-c\hbar^2$ with each of them being doubly degenerate due to Kramer's degeneracy. $|\frac{3}{2}>$ and $|-\frac{3}{2}>$ is the first set of doubly degenerate eigenstates and $|\frac{1}{2}>$ and $|-\frac{1}{2}>$ consists of the second set. The value of c will depend on the value of the quadrupole moment of the $5D_{\frac{3}{2}}$ of Ba^+ ion [70], as well as the magnitude of the components of electric field gradient.

Now to transform back to the laboratory frame, we apply the Wigner D-matrices. Transformation to the laboratory frame consists of a rotation of $-\phi$ along the z-axis and then $-\theta$ along the rotated y axis and the third rotation being a null rotation. The time dependence comes from $\phi = \omega t$. Applying the Wigner matrices we obtain the following Berry phases for the eigenstates of the Hamiltonian
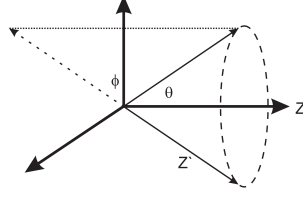
Figure 3.8: Principle axis of field gradient relative to laboratory axis. $\phi = \omega t$ is the time dependent parameter leading to rotation of the principle axis w.r.t. lab z-axis

$$\gamma_1 = 3\pi(\cos\theta - 1) \tag{3.48}$$

$$\gamma_2 = \pi((4 - 3\cos^2\theta)^{\frac{1}{2}} - 1)$$

$$\gamma_3 = -\pi((4 - 3\cos^2\theta)^{\frac{1}{2}} - 1)$$

$$\gamma_4 = -3\pi(\cos\theta - 1)$$

where 1, 2, 3 and 4 signify the states $|-3/2\rangle$, $|-1/2\rangle$, $|1/2\rangle$ and $|3/2\rangle$ respectively.

The constants of integration are so chosen as to ensure zero phase for $\theta = 0$. Thus incorporating the phase dependent energy shifts, we obtain the energies of the eigenstates as

$$E_4 = \alpha\hbar^2 - \frac{\hbar 3\pi(\cos\theta - 1)}{T}$$

$$E_3 = -\alpha\hbar^2 - \frac{\hbar\pi((4 - 3\cos^2\theta)^{\frac{1}{2}} - 1)}{T}$$

$$E_2 = -\alpha\hbar^2 + \frac{\hbar\pi((4 - 3\cos^2\theta)^{\frac{1}{2}} - 1)}{T}$$

$$E_1 = \alpha\hbar^2 + \frac{\hbar 3\pi(\cos\theta - 1)}{T}. \tag{3.49}$$

Thus the eigenvectors split depending on the Berry phase of each of the states as well as the frequency of rotation of the Hamiltonian. The Berry phase itself is independent of any external field value but only depends on the geometry of the rotation axis with respect to the quantization axis. This is not surprising since this phase is a purely geometric in nature and is potentially applicable to perform fault tolerant quantum information processing. This interaction can be mimicked by ion trap field gradient and the electric quadrupole moment interaction of the trapped ion.

3.8.1 Implementation of Rotating Field Gradient

An ion trap is a three dimensional harmonic oscillator with the three axes of oscillation being independent of each other, as is explained in Chapter 1. The electrodes define the trap symmetry axis. The
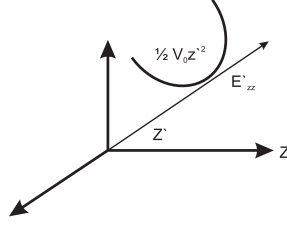
Figure 3.9: The tilted potential $\frac{1}{2}V_0 z'^2$ and resultant field gradient E'_{zz}
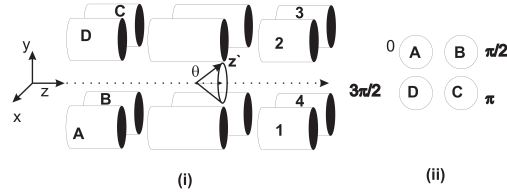

Figure 3.10: (i) Trap design and the resultant field gradient axis. (ii) Cross-sectional view and phase of applied RF.

proposal is based on the fact that a potential tilted with respect to the trap symmetry axis ($\frac{1}{2}V_0 z'^2$) can give rise to a field gradient whose principal axes are tilted with respect to the trap symmetry axes, also defined by the trapping electrodes, as shown in Fig 3.9. However it has been shown by our calculation and also in [70] that the main contributing component is the $\frac{\partial E_z}{\partial z}$ component. It can be proved by taking the potential $V = \frac{1}{4}V_0 x^2 + \frac{1}{4}V_0 y^2 - \frac{1}{2}V_0 z^2$ and calculating the Hamiltonian of quadrupole interaction. Hence for simplicity, we consider only the $\frac{\partial E_z}{\partial z}$ component of the field gradient tensor to be non-zero while the other components to be zero.

Thus the design goal is to have electrode geometry which can produce a parabolic potential rotating about the linear trap axis. It can be established using a segmented four rod structure for the end caps in a linear Paul trap and applying RF voltages on diagonally opposite end cap rods across the body. As is demonstrated in figure 3.10, by connecting body diagonally opposite end cap rods (e.g. A and 3) and applying suitably phase shifted RF voltage on each of the four pair of end cap rods ($\frac{\pi}{2}$), it is possible to rotate a parabolic potential about the trap axis [71], leading to rotation of the field gradient about the axis of symmetry. The proof of the fact that a tilted potential can give rise to a tilted field gradient will be obvious by calculating the field gradient matrix from a potential $\frac{1}{2}V_0 z'^2$ and comparing it with a matrix obtained by rotating the basis of a gradient matrix with only $z'z'$ component and representing it in the trap basis, i.e. $R^T E'_{z'} R$ with Euler angles ϕ,θ and 0.

Here we will show that such a distorted trap indeed leads to a tilted potential. We simulate the

58

trap potential, given its geometry and the rotating time dependent potential, using *Simion* 7.0 and plot the three components of the electric field for a position, off axis from the trap center (exactly at the trap center the field is zero). Also we plot the electric field as obtained theoretically by taking the gradient of the potential $\frac{1}{2}V_0 z'^2$. The electric field components, E_x, E_y and E_z are plotted as functions of each other in a three dimensional graph as a phase diagram and the two situations are compared, Fig. 3.11 (a) and (b).

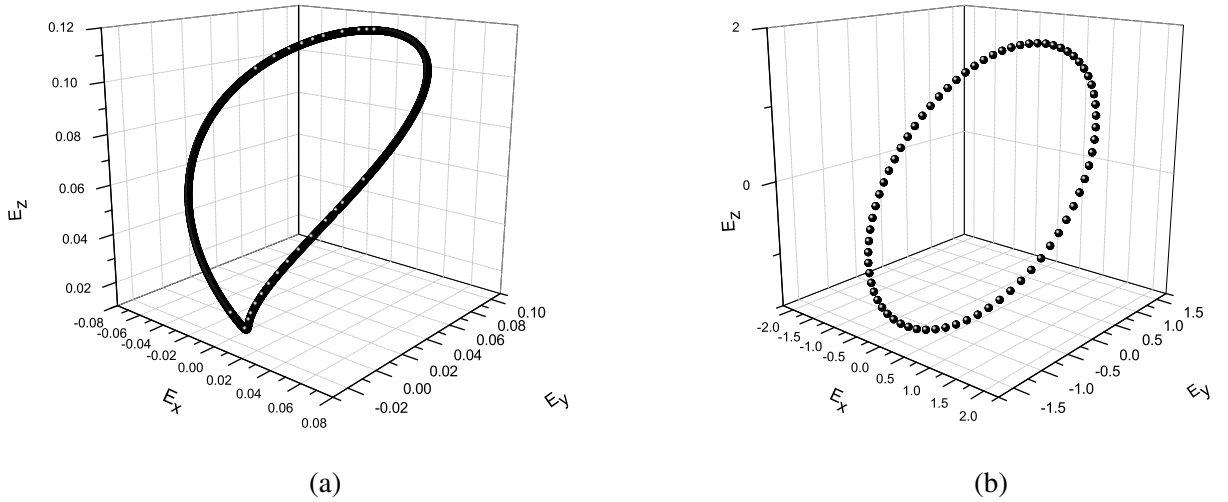(a)   (b)

Figure 3.11: Correlation of time dependent electric field components according to theoretical predictions (a) and Phase diagram of time dependent electric field components from Simion (b).

As can be seen there are certain differences between the two figures. They arise out of the fact that even though $\frac{1}{2}V_0 z'^2$ assumes a x' and y' symmetry, the actual trap does not have so and hence it can lead to the difference that is observed. The value of θ has been taken as 40.7^o for generating the first graph. This value corresponds to the angle a straight line, connecting the middle of two diagonally opposite rods, makes with the trap axis. Hence we can assume that the trap creates a sort of a distorted parabola when the above mentioned potential is applied to the end caps.

To obtain the true form of the potential in the case of the actual trap geometry, the potential along the diagonal is plotted for two values of the end-cap voltages 500V and 1000V respectively (Fig. 3.12).

The fitting parameters show that as the voltages of the end caps are increased, potentials become more parabolic. However, the berry phase and the resultant energy difference is independent of the
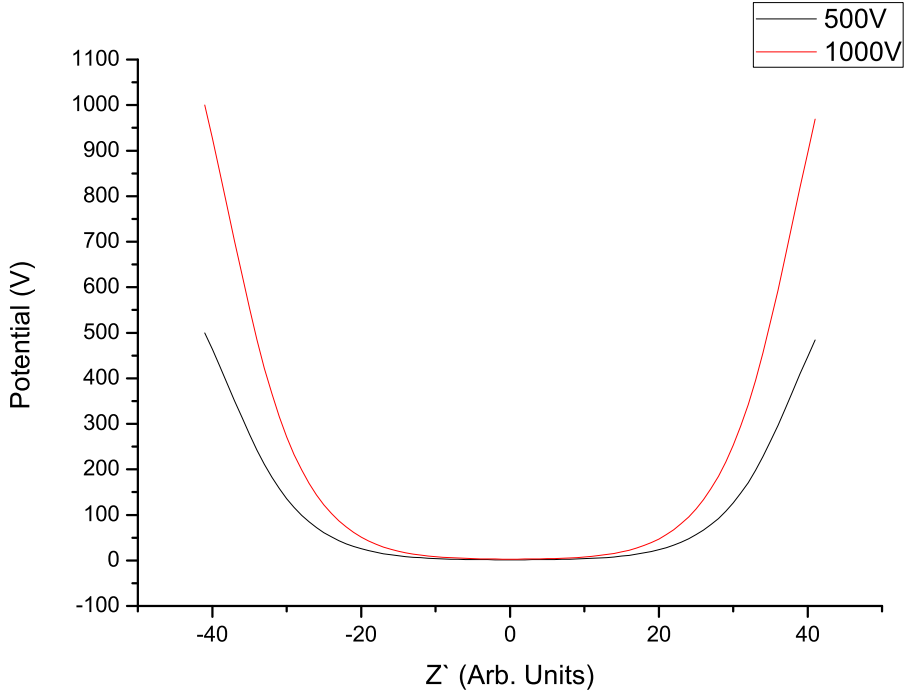
59

Figure 3.12: Potential along z' for end cap voltage of 500 and 1000.

magnitude of the field gradient and hence it should not affect the splitting of the levels.

To maintain the adiabatic condition, the precession frequency has be much smaller than the level splitting caused by the Hamiltonian itself. As an example, for Ca ion, the splitting is of the order of 150 Hz for an electric field gradient of about $50V/mm^2$ [27]. Since the quadrupole moment of Ba^+ is almost double that of Ca^+ [70], hence we can assume that given similar gradient magnitudes, the splitting will be of the order of 300 Hz and the rotation frequency should be much less than that. For such low frequencies, it will not affect the motion of ions in the trap as the relevant trap frequencies are of the order of MHz.

3.9   Conclusion

This chapter demonstrates the range of interactions that can be studied using the trapped barium ions. Ranging from weak interaction to artificial gauges, the presence of metastable states with long lifetimes, dipole forbidden transition and inherent quadrupole moment, makes barium an ideal system to study this vast array of interactions.

The branching fraction measurement gives greater insight into the dipole matrix elements cou-

pling different excited states while quadrupole moment measurement can potentially reveal detailed information about the structure of the D state wavefunction of the barium ion.

From the point of view of Abelian and non-Abelian physics, this system can provide insights into changeover from abelian to non-abelian situations. For the first time, using a combination of ion trap potentials and external magnetic fields, it is shown here that the system can be continuously driven from non-Abelian to Abelian regime and obtain detailed insights about the adiabaticity of a quantum system as well obtain the capability of engineering any form of artificial gauge, as is needed by the application. As a first step towards implementing such a scheme, one needs to measure the quadrupole moment. Later in the thesis the experimental development is discussed in more detail.

Chapter 4

Development of Experimental Setup

In course of this thesis work, a barium ion trap system has been developed and experiments were performed. Development of the experimental set up includes

1. Developing laser systems for laser cooling of barium

2. Design and constitution of ion trap and vacuum chamber.

3. Imaging and detection systems

4. Ultra-stable narrow linewidth 1760 nm diode laser system

In the following each of the sub-system relevant to this thesis will be discussed in further details.

4.1   Laser Systems for Trapping and Laser Cooling of Barium Ion

4.1.1   493 nm laser for S-P transition (cooling laser)

The primary transition used for laser cooling of a barium ion is $6S_{1/2}$ to $6P_{1/2}$ dipolar transition. The resonance wavelength for this transition is 493.54537 nm in vacuum. Lack of suitable diodes in this wavelength region forced us to obtain this wavelength via frequency doubling of a 986 nm laser diode. The frequency doubled system is a commercially available *Toptica* SHG PRO system with an output power of about 90 mW at 493 nm.

The first stage of the system comprised of an ECDL operating at 986 nm and giving an output of about 200 mW. A small part of this laser power is sampled for purposes of frequency stabilization

with respect to a reference cavity and wavelength measurements. The rest of it is sent to a bow-tie cavity with a doubling crystal inside. A cavity is used to enhance the conversion efficiency of the frequency doubling crystal by creating a multi-pass system. The cavity is designed such that it forms a cavity for only 986 nm while it is transparent to 493 nm light at the output mirror. The cavity length can be adjusted by a piezo. The cavity length is locked by Pound Drever Hall technique to the output of the 986 nm laser to give about 90 mW power at 493 nm with manufacturer specified linewidth of about 1 MHz.

The laser output of the 493 nm laser has several optimization parameters. Primarily it is the temperature of the doubling crystal which is optimized for non-critical phase matching of the non-linear process. The temperature range for this phase matching is quite narrow and often is about 1 K wide. So optimization of temperature is one of the key points for optimal output power. Secondly, the power can be maximized by the cavity alignment. Maximum power output is obtained by suppressing all but one transverse mode of the doubling cavity. The alignment mirrors are a part of the commercial setup provided by *Toptica*. And lastly, it is the crystal alignment within the cavity as well as small alignment of the output mirror which has to be fine tuned to maximize the power output of the system. Usually the system is quite stable, requiring adjustment of the alignment in an interval of more than six months.

Frequency Stabilization of Cooling Laser

Frequency stabilization means keeping the laser at a fixed pre-defined frequency. While a wavemeter provides monitoring of the actual wavelength, a frequency stabilization setup provides an active feedback to the laser to keep the frequency at the right value. Moreover wavemeter requires frequent calibration to provides desired accuracy because of which frequency is often referenced with a transition of an element or a molecule. Frequency stabilization is an important part of the optical setup for the experimental system. This is because there is always a frequency drift of all ECDLs and this effects the response of the ion. For example, if the cooling laser drifts to the blue side of the transition, then instead of cooling, it will start heating the ion and ion can even be lost from the trap.

For frequency stabilization of the 493 nm laser, we use the spectrum of ^{130}Te$_2$ molecule. Mod-

ulation transfer spectroscopy has been used, which is a modification of the saturated absorption spectroscopy. The optical setup is shown in Fig. 4.1.
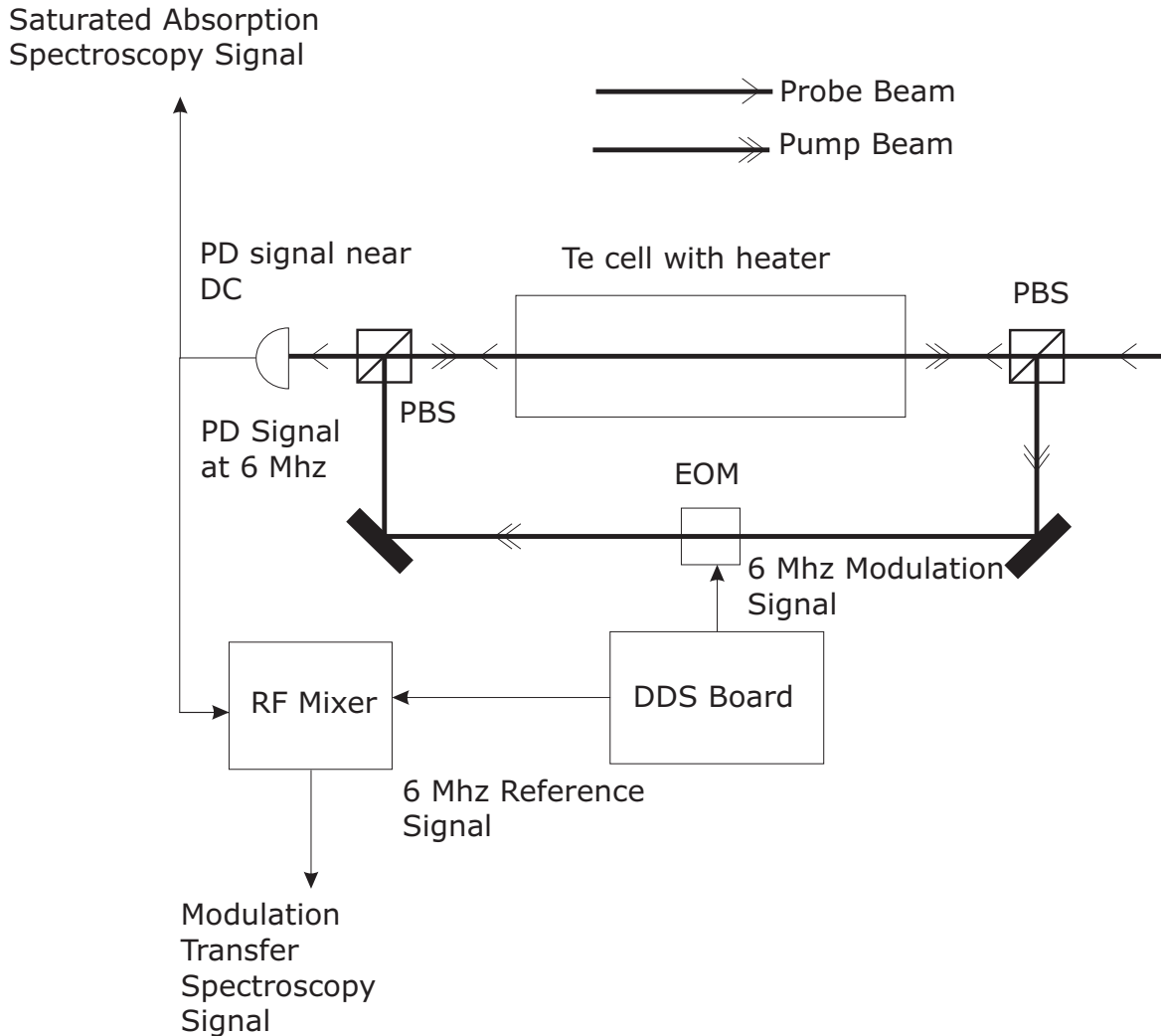
Figure 4.1: The setup for Saturated Absorption Spectroscopy and Modulation Transfer Spectroscopy of $^{130}Te_2$. It shows the optical layout as well as the electronic requirements to obtain the spectroscopic signals.

The Te_2 comes in a quartz cell and is a solid metal deposited on the wall of the cell. To obtain reasonable vapour pressure of Te_2, we heat the cell to about 550° C. The challenge here is to create a proper design which can maintain the cell at high temperatures and at the same time the assembly can be used on the optical table as a part of an optical setup. Uniformity of heating is also a major concern as colder part of the cell can have solid Te_2 deposition. Since in the entire setup, the windows of the cell are usually exposed to the outside atmosphere, they tend to be the coldest part of the cell. However, the design of the internal mount, as shown in Fig. 4.2 is made such that the windows of the

cell are also heated uniformly as the rest of the cell.

First the cell is put in a two piece stainless steel jacket as is shown in Fig. 4.2 and then a ceramic heating collar, from *Watlow* (model no. MBIJ3ANI-X48), is used to heat the cell. Then the entire contraption is wrapped with high temperature insulation tape such that it tightly fit inside a 10 cm stainless cylinder which is then placed on a stand on the table. Fig. 4.3 shows the image of the setup as placed on the optical table.
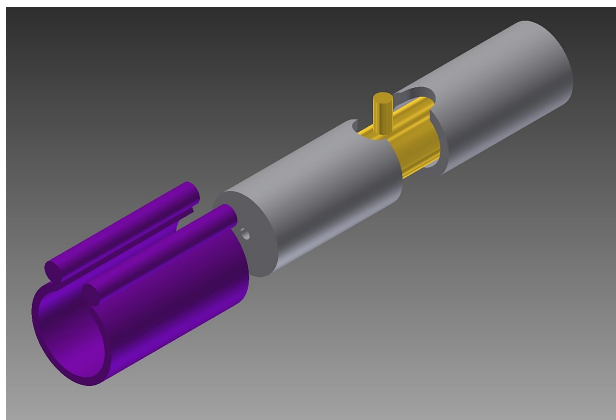

Figure 4.2: CAD drawing showing the architecture of the Te cell assembly inside the enclosure. The yellow part is the cell, the gray are the stainless steel covers (stainless steel because aluminium has melting point near 600° C and we are heating to about 550° C) and the purple is the ceramic band heater used to heat the cell.

Figure 4.3: The complete tellurium cell setup. The stainless steel cylinder houses the cell. The cell temperature is 550° C while the temperature outside the cylinder is about 50° C.

Using this design we achieved high thermal insulation with the cell temperature being around 550° C and the outside temperature of the cylinder being around 50° C.

We use a modulation frequency of 5.79 MHz to drive the EOM, from *Qubig* (model no. EO-F6M3-VIS), resonantly. The setup provides both saturated absorption spectrum of Te$_2$ as well as modulation transfer spectra of it as is shown in Fig. 4.4. The drift of 493 nm laser is restricted by frequency locking the ECDL of 986 nm master laser to an MTS resonance, near 493 nm, which is 330 MHz blue detuned from the barium resonance as is shown in Fig. 4.4. The actual locking of the

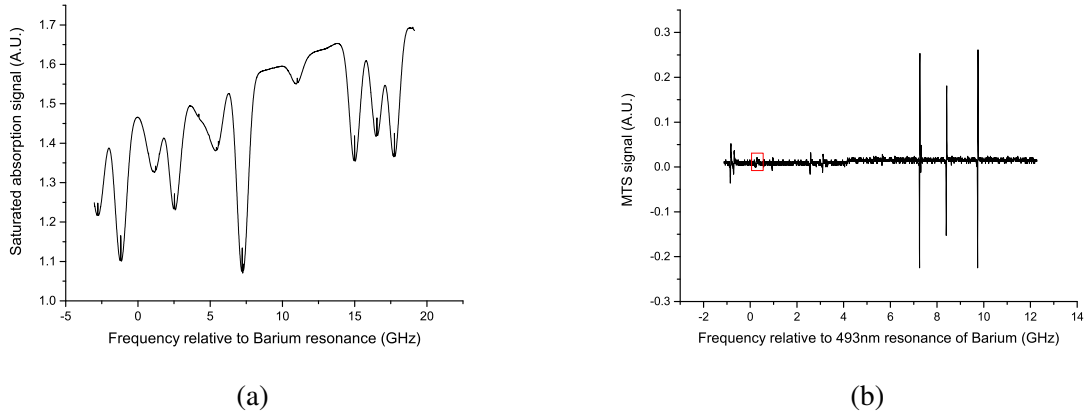(a)   (b)

Figure 4.4: The figure shows the saturated absorption spectra and the modulation transfer spectra of tellurium in the frequency region around the 493 nm transition of barium. The red box in figure (a) shows the mts peak where the 493 nm laser is locked.

493 nm laser is performed in two stages. First, the master laser is locked to a reference cavity whose length can be adjusted by a piezo. Once the laser is locked to the cavity, the cavity is then locked to the Tellurium saturated absorption peak, which takes care of any drift of the cavity or ECDL over time.

4.1.2   413 nm Ionization Laser

To trap barium in an ion trap, we need to create ionized barium. While that can be done in several ways, such as electron beam ionization, where high energy electrons knock out one electron from the atom, we used resonant laser photoionization using a single 413nm ECDL laser [91–97, 120].

The photoionization by 413 nm is a two photon process, as is shown in Fig. 4.5. The first photons resonantly excites the barium atom to an intercombination line, having a line width of about 200 kHz and then the second photon takes the electron to a auto-ionization state near-resonantly from where
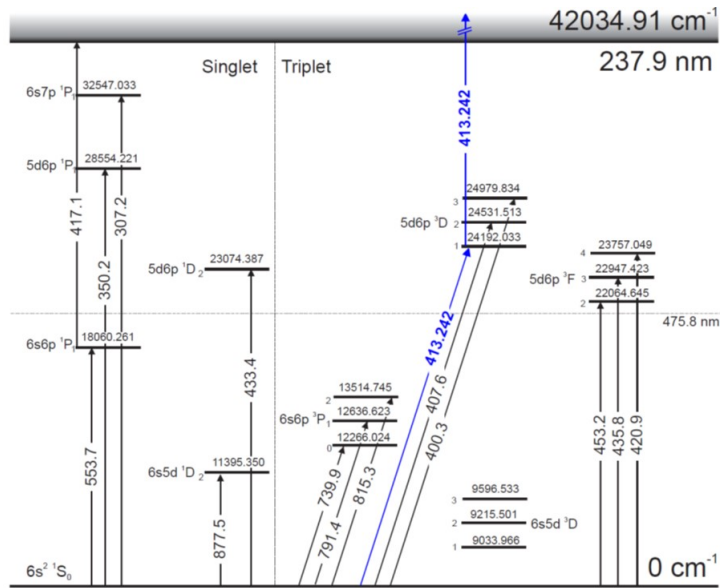
Figure 4.5: The spectrum of neutral barium. The 413 nm laser first excites the atom to an intercombination state. Then the second photon excites the atom to an auto-ionization state [97].

the electron is ejected from the atom. The spectra for neutral barium atom is shown in Fig. 4.5, as a reference to the scheme. The resonance of this transition is 413.2426 nm, in air. While there are some other photoionization schemes for barium, all of them require multiple lasers for the process. The advantage of our process is that it requires a single laser and yet it is as selective as a resonant multi-laser process.

4.2   Design of the Ion Trap

The ion trap used for this experiment is a linear Paul trap with blade like RF electrodes. This ensures harmonicity of the potential near the trap center. Figure 4.6 shows the CAD drawing of the RF blades and end cap electrodes.

The blade design of the RF electrodes allowed us to reduce the distance between the rf blades in the trapping region without compromising on the optical access and photon collection efficiency. For the trap used, the distance between the blades of the RF electrodes, is 1.4 mm.

The end caps are also designed to have a hyperbolic surface facing the ions to ensure harmonic trapping potential. Fig. 4.6 shows the design of the end caps used for the trap. The trap electrodes
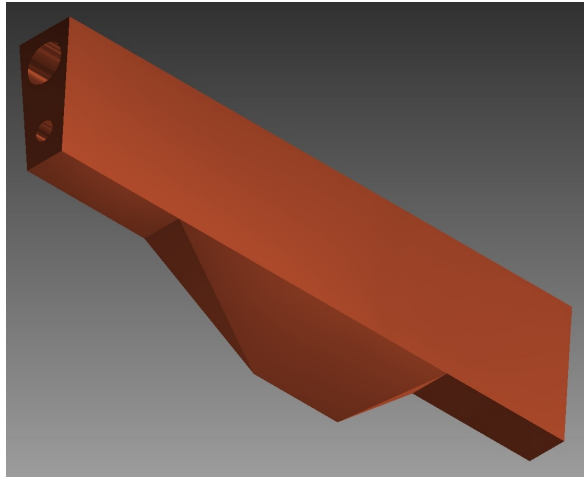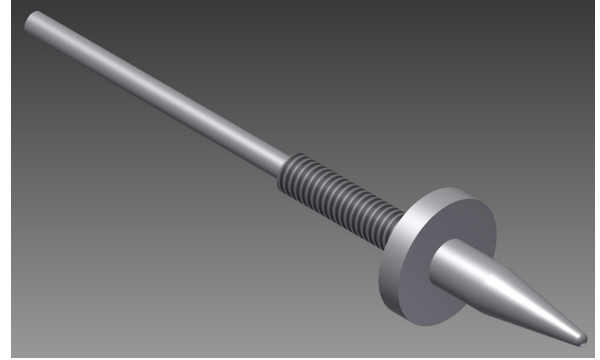
(a)   (b)

Figure 4.6: The CAD drawings of the trap electrodes. Fig. (a) is the RF electrode which provides the radial confinement via RF voltages and Fig. (b) is the end cap electrode which provides the axial confinement.
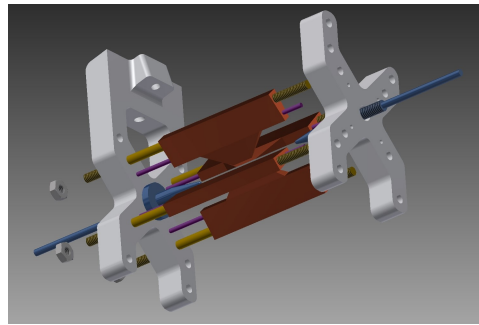

Figure 4.7: The complete trap design.

are held in place using electrically insulating ceramic called Macor. Macor, along with providing insulation, also has low de-gassing rates and high thermal stability which is extremely good for UHV environment. Fig 4.7 shows the complete trap design. The macor has holes for holding the barium atomic ovens. These ovens are thin and long metallic cylinders which are heated to high temperatures ($\sim 1000^{o}$C) by passing current through them. This in turn leads to the production of barium vapour forming a beam of neutral barium atoms which are then ionized inside the trap by the 413 nm laser.

Fig. 4.8 shows a picture of the actual trap while it is being assembled. The wires used for connection are Kapton coated copper wires. Kapton provides insulation and have low out gassing properties, making them ideal for wire insulation in UHV environment. The whole trap as shown in the picture along with all electrical connections is assembled on a single CF 200 flange, thereby minimizing the assembly error of the trap and the collection optics.
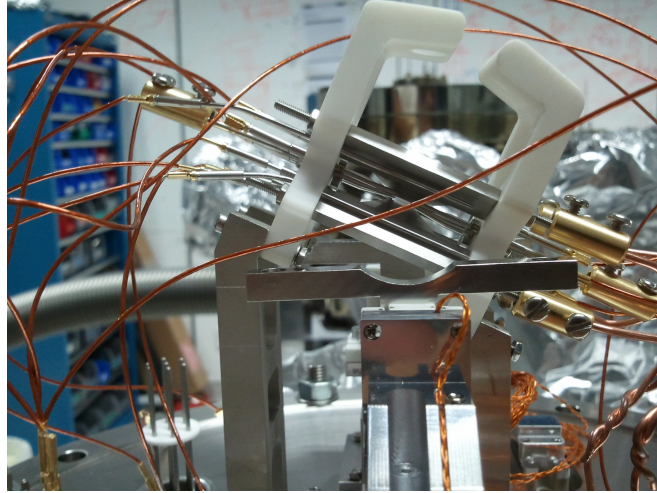
Figure 4.8: The actual trap while assembling. The ions are trapped in the empty space between the electrodes.

4.3   Vacuum Chamber Design

The ion trap is housed inside a vacuum chamber. The collision of the test particles with surrounding atmosphere, which is made up of a huge number of particles, is the bane of atomic physics. Reducing the pressure of the surrounding atmosphere, means lesser number of atoms in the vicinity of the experiment and hence lower collision rate of the background particles with the atoms related to the experiment. The vacuum required will depend on how long the atom is required to be isolated or the mean free time, the time between two collisions. To estimate the target vacuum, let us consider a trapped ion is oscillating at 1 MHz with an amplitude of 3 μm. Thus in one second, the ion effectively travels a distance of 6 m. Now mean free path depends on the pressure of the gas and also its temperature. At room temperature, for ultra high vacuum, where pressure ranges from 10^{-7} to 10^{-12} mbar, the mean free path is of the order of 10 km. So the average time between two successive collisions at ultra high vacuum conditions is about 20 minutes.

However, for ion traps, the collisional cross-section is much higher than that predicted by kinetic theory of gasses because of the charge of the trapped particles. For our experiment, with a pressure of about 10^{-10} mbar, we observed collisional rate of about 1 Hz or three orders of magnitude higher than that predicted by kinetic theory of gasses.

4.3.1 The Chamber

Now that we have established that we require ultra high vacuum environment for running the experiments, we move on to designing the vacuum chamber. The vacuum chamber has a base dimension of a CF 200 flange, that is having a diameter of 200 mm. This is done to allow for space for putting in the nano-positioners as well as their connectors. It also facilitated using of 4 electrical feedthroughs since the ion trap having geometric phase generation capabilities needs to have 18 electrodes (4 for RF, 2 for end-cap, 4 for compensation, 8 for geometric phase generation as explained in Chapter 2) and three more connections for the atomic oven of barium. The geometric phase generating trap is however not used for the work in this thesis. The downside to having a CF 200 flange on the other hand is that the chamber had a large pumping volume and thus it required a long time to achieve the target vacuum.

The CF 200 flange carried the entire experimental setup, including the trap, the nano-positioner with the imaging system and all the electronic connections as is shown in Fig. 4.9 and 4.10. This is done such that the entire system can be assembled and fixed on the chamber quickly as barium oxidizes fast when exposed to air and thus the entire process from connecting the oven, after taking it out from an argon filled chamber, to sealing the chamber and running the pump has to be done fast. Hence a modular design of the experimental flange is implemented. More importantly a single flange assembly allows a low assembly tolerance of the trap parts and the optics of photon collection reducing the chances of design and assembly error.

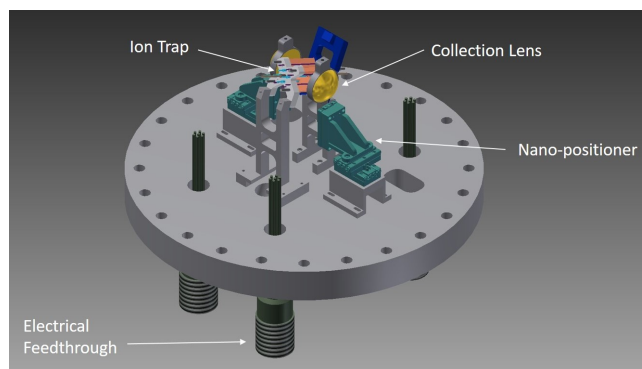Figure 4.9: The design of the experimental flange. The ion trap is setup on a CF 200 flange which is then connected to the chamber. On the flange, there is the ion trap, the collection lens and the electrical feedthroughs which establish electrical connection between the laboratory and the environment inside the chamber.

The vacuum chamber is designed to have 8 viewports. This is done to allow addressing the centre
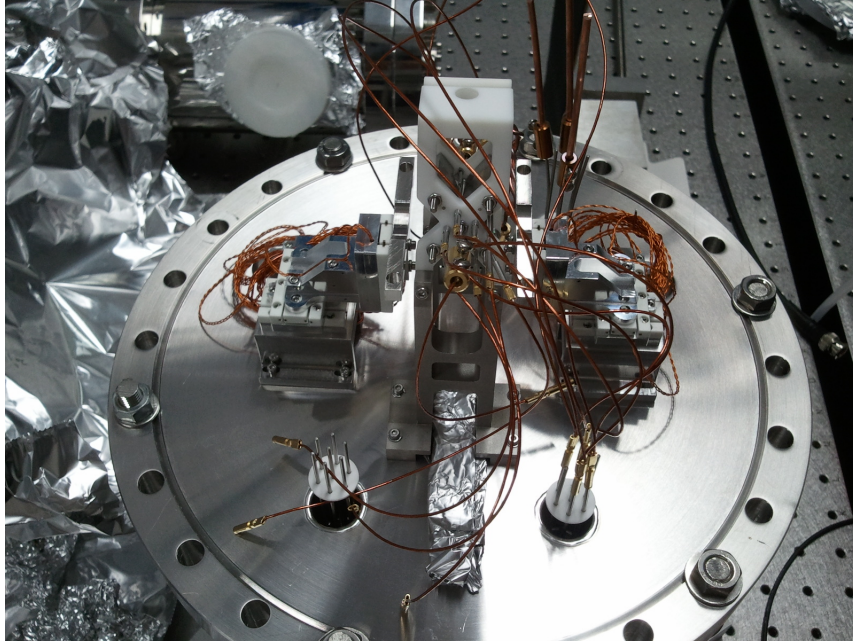
Figure 4.10: Assembly of the experimental setup flange. Along with the trap, it also shows the electrical feedthroughs as well as vacuum compatible nano-positioner which are used to control the photon collection lens inside the chamber.

of the trap at different angles with respect to the trap axis. Two viewports allow for laser beam to propagate along the axial direction of the trap, which is main cooling beam direction. Since the trap is mounted at an angle of 30° with respect to the axis of the viewports of the cooling beam, it lets the cooling beam to address all the principle axes of motion, which reduces the amplitude of the motion of the ion in all directions very efficiently. Fig. 4.11 shows the direction of the cooling beam. Two other viewports, perpendicular to the cooling beam and the axial direction of the trap is used for imaging as well as to address the ions using the 1760 nm laser. These viewports are kept to allow individually addressing of each ion in a linear chain, with the chain direction along the axis of the trap. And finally the 2 sets of viewports at 45° with the cooling beam direction are used to address the ion at an angle, different than the cooling beam direction. These beams are used to provide optical pumping as is described in Chapter 5. The viewports are connected at an angle of 15° with respect to the tube connecting them with the main chamber. This is done to prevent the back reflected the light from the exit viewport from reaching the experimental region. The viewports also have anti-reflection coating at 493 nm and 650 nm to reduce reflection while the light is passing through. It also helps to increase the photon collection efficiency for imaging, since the detectors are outside the vacuum chamber.

The assembly also has a separate pumping chamber. This is used to connect the ion pump (*Varian* S40) and the titanium sublimation pump. The separation of the pumping chamber from the experimental chamber keeps the large magnetic field of the ion pump farther away from the experimental region and prevents the titanium sublimation pump, which works by evaporation of titanium, from having a direct line of sight access to the ion trap. Also from a design perspective, it provides a modular structure, allowing us to work independently on the pumping system without changing anything on the experimental side.
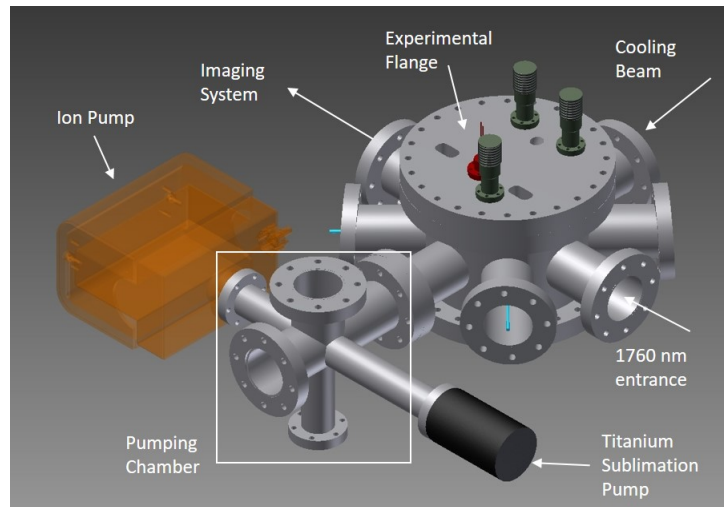

Figure 4.11: The CAD drawing of the full experimental chamber. The green cylinders on the top are DC electrical feedthroughs while the red is RF feedthrough. The brown structure on the top left corner is an ion pump and the black cylinder is representative of titanium sublimation pump.

4.4   Imaging and Detection System

Once we ionize, trap and laser cool the ion, the next step is detection of the trapped ion. For detection and measurements we use an electron multiplying CCD and a photo-multiplier tube (PMT) respectively. The CCD provides the image while the PMT provides the counts which are used for the actual experimental results.

To improve on the collection efficiency of the spontaneously emitted photons from the ion, we placed an aspheric lens inside the vacuum chamber on a vacuum compatible nano-positioner stage from *Smaract* as is shown in Fig. 4.10. This lens has an effective focal length of 17 mm and have a numerical aperture of 0.4. The nano-positioner allowed for very fine control of the internal lens

and thus enabled maximization of collection efficiency. The weight of the lens and the lens holder is kept below 100 gm to ensure that the load is lower than the maximum carrying capacity of the nano-positioner.
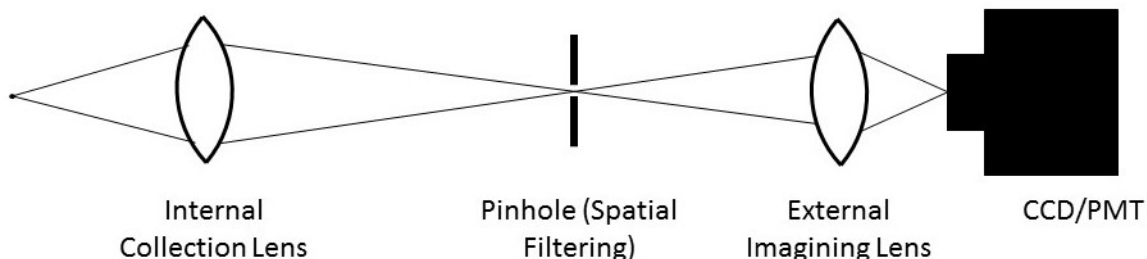
Figure 4.12: Imaging system layout.

The camera used is an *Andor* Luca CCD with electron multiplication capability. The size of each pixel is $8\mu \times 8\mu$. To obtain a reasonable signal level, we aimed to have the image size of the ion over 5 to 6 pixels, which means having an image size of the order of 40 microns.
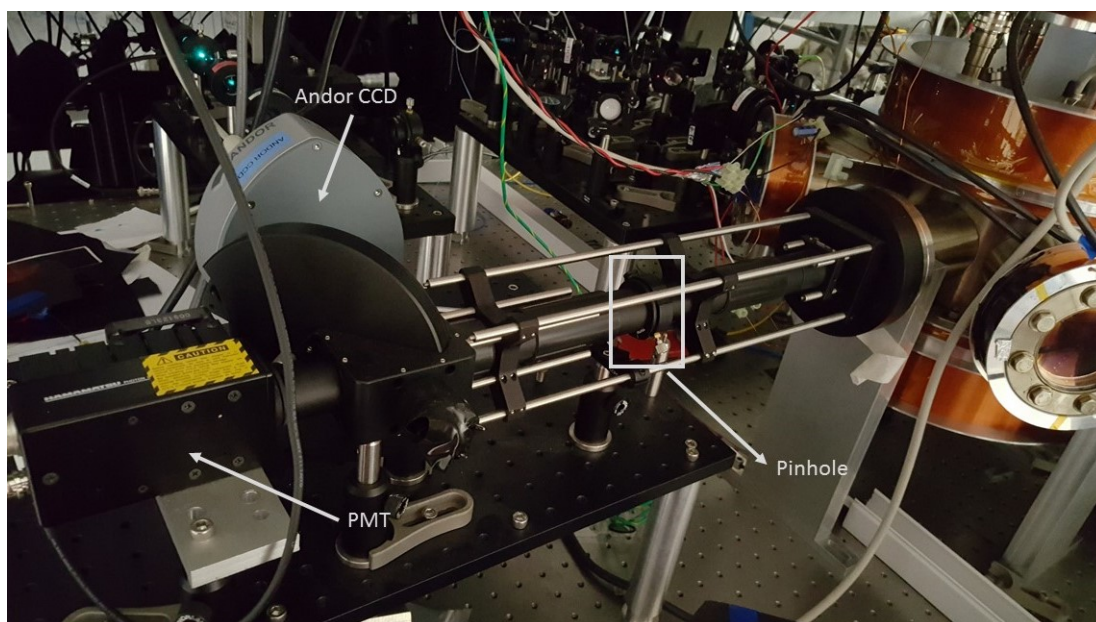
Figure 4.13: Imaging system showing the pinhole and the detection devices.

For a single ion, the amplitude of motion after Doppler cooling can range from $1\ \mu\ m$ to $.1\mu\ m$. The diffraction limit of the internal photon collection lens is about 0.4μm.

The imaging system is designed for a variable magnification of the image. This is done so that during initial loading, while setting up the system, we can get a wide-angle view and then we can

Figure 4.14: The first cloud of barium, trapped and laser cooled, in the setup described here. The cloud is shifted in one direction due to non-central position of the imaging system.

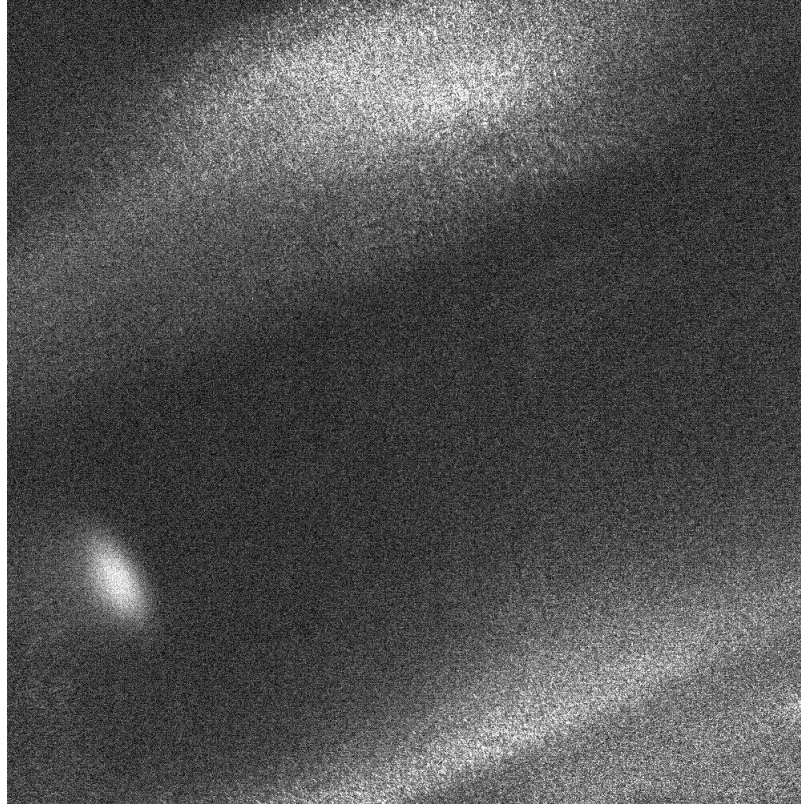zoom into the ions for a higher signal-to-noise-ratio (SNR). A pinhole is used as a spatial filter of the ions and to remove unwanted scattered light from the trap electrodes. The spatial filtering of the light is required to obtain a good SNR which in our case varied from 5:1 to 10:1, depending on the exact alignment of the lasers.

Fig. 4.14 and 4.15 show images of the ion cloud and crystalized ions as obtained by this imaging system.

4.5   Narrow Linewidth 1760 nm Laser System Development

The 1760 nm laser is required for addressing the $S - D$ transition of the barium ion. However, due to dipole forbidden nature of the transition, the linewidth of the transition is of the order of several mHz. This would require the laser linewidth to be extremely narrow to allow for achieving suitable Rabi frequency of oscillation of the order of 10 kHz and coherent manipulation. The laser belongs to *Toptica* DL Pro ECDL family. According to manufacturers, the initial linewidth of the laser is of the order of few hundred kHz. Along with narrow linewidth, lack of any absolute frequency reference
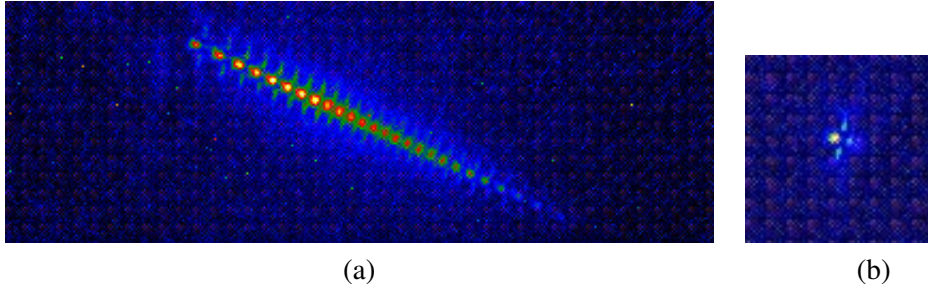
Figure 4.15: Ion crystal images. Fig. (a) is a linear chain of 25 ions and Fig. (b) is a single ion trapped and laser cooled.

for this laser implied that we required an ultra stable cavity for stabilizing the laser frequency.

The first cavity used an Invar spacer and had a finesse of 3000. It also had a piezo actuator on one of the mirrors to allow of small tuning of the laser frequency once it is locked to the cavity. The cavity linewidth was determined from the relation between linewidth and photon lifetime, given as $\delta\nu = 1/(2\pi\tau)$, where τ is the lifetime of the cavity as is determined experimentally from the decay of the transmission signal of the cavity when the light to the cavity is switched off. Fig 4.16 shows the signal decay curve of the home built cavity, to be called cavity1. From the decay time, the linewidth of cavity1 is determined to be 600 kHz. The switching time for the light without the cavity, as detected, was less than 100 ns. While it is of the same order as the cavity decay time, the switching measurement gave an upper limit to the cavity linewidth.

Cavity1 was used to develop the locking systems and also perform preliminary spectroscopy experiments for the quadrupole transition. It helped in developing necessary expertise required for working with the commercial cavity which was installed later. The locking has been performed using a Pound-Drever-Hall setup. Using cavity1 as reference, the spectrum of the S-D transition showed a linewidth of about 10 KHz, dominated by the laser linewidth.

4.5.1   Characterization of Commercial Cavity

After cavity1, we installed a commercial cavity system from Stable Laser Systems (SLS). The finesse is about $300,000$ with a free spectral range of 1.5 GHz, giving an estimated cavity linewidth of 5 kHz.

The linewidth of the SLS cavity has been measured using transmission power decay measure-
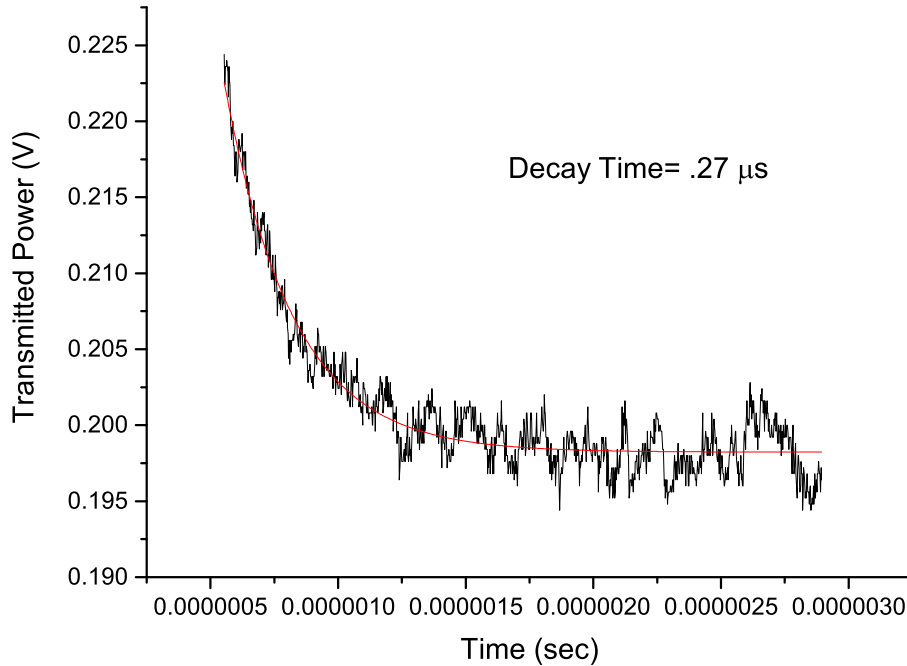
Figure 4.16: Cavity decay signal of the locally made cavity. The fitting gives a decay time of 0.27 μs.

ment. The 1760 nm laser is locked to the cavity, with an AOM in its path. The light is then switched using an AOM and the transmission power is measured by a fast photodiode as a function of time. The detected switching time for the light without the cavity was less than 1 μs.

The decay measurement gives a cavity linewidth of around 5 KHz, as specified by the manufacturer. Locking to this cavity required development of a high bandwidth error signal generating board. The correction, being given by the FALC module of *Toptica*, had a bandwidth of the order of 30 MHz. Thus a error signal generating board is designed and developed having a bandwidth close to 30 MHz. This allowed for extremely stable lock of the laser to the high finesse cavity and a laser linewidth of around 300 Hz as is measured from the fourier limited linewidth of the quadrupole transition.

4.6   Conclusion

The system to trap and laser cool ions is developed with physics, described in Chapter 2 in mind. While the 493 nm and 650 nm lasers are used for high precision measurement of the branching ratio,
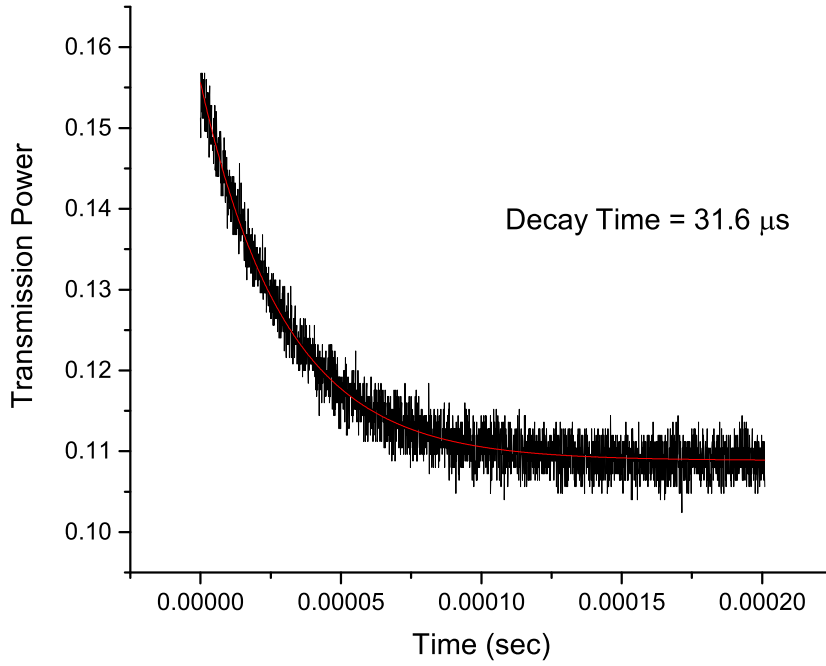
Figure 4.17: Cavity decay signal of high finesse SLS cavity. The fitting gives a decay timescale of 31.6 μs.

as is described in Chapter 4, the 1760 nm laser is used to address the dipole forbidden transition between $6S_{1/2}$ and $5D_{5/2}$, described in Chapter 5, to run an extremely fast optical qubit near the telecom wavelength as well as in preparation for measurement of quadrupole moment of the D levels of barium ion.

Chapter 5

Precision Measurement of Branching Ratio for $6P_{1/2}$ level decay: towards PNC measurement

As discussed in chapter 2, branching ratio measurement plays a vital role in our understanding of the parity non-conserving effects in atomic systems. In this chapter the measurement processes and experimental implementation of the algorithm discussed in Chapter 3 as well as the details of the data analysis that was performed for this experiment is discussed.

5.1   Experimental Setup

A schematic of our setup is shown in Fig.5.1. The ion trap, as described in Chapter 4, is driven with a RF frequency of about 16 MHz and with about 1 Kv amplitude giving a radial secular frequency of approximately 1 MHz. The axial potential was kept such that the axial frequencies was about a few hundred kHz. For the experiment we trapped and laser cooled about 20 ions. This was done to improve the signal-to-noise ratio and to ensure that we acquire statistically significant counts in a relatively short period of time. Since we are measuring internal properties of the ion and not the motional one, presence of multiple number of ions does not effect the result of our experiment and only aids in reducing the statistical uncertainty of the measurement.
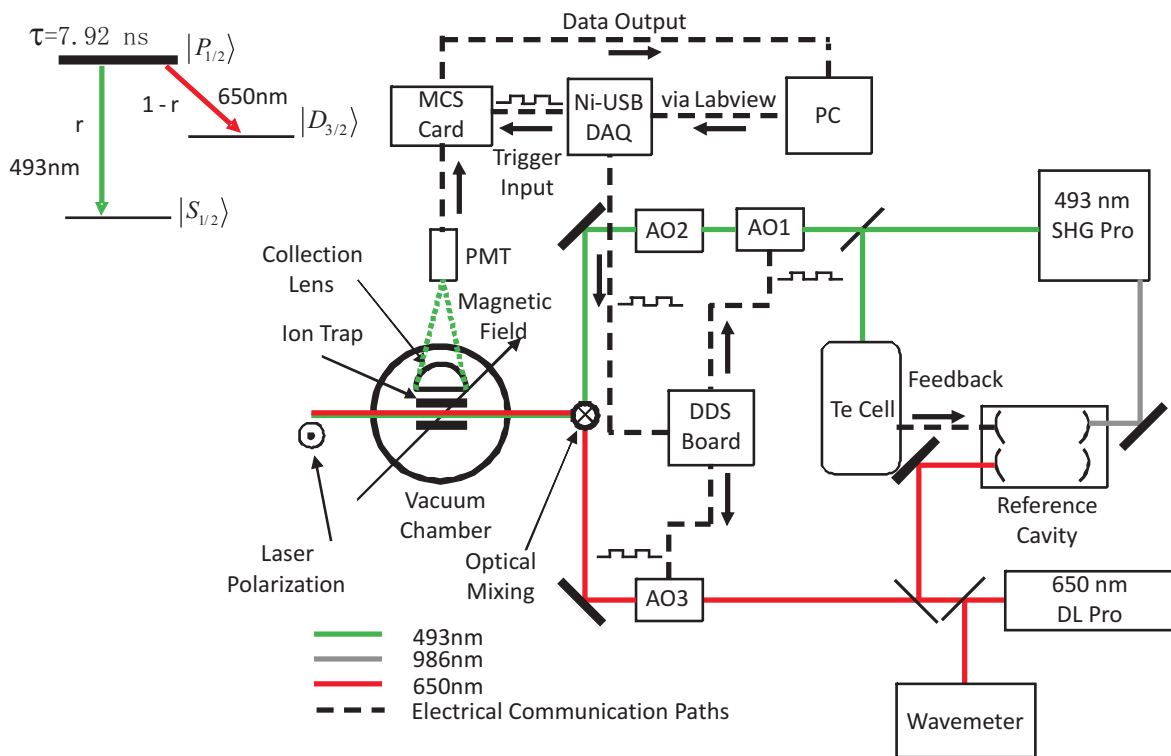
Figure 5.1: Schematic diagram of our experiment: During the experiment, AO1 and AO3 are switched using a DDS controlled by NIDAQ. Relevant atomic levels of Ba^+ ions are also shown. The branching fractions reported here are r and $1 - r$ for the two decay channels.

Both the 493 nm laser and 650 nm lasers are locked to reference cavity. The 493 nm is additionally frequency locked to a Tellurium resonance line using modulation transfer spectroscopy in a Tellurium cell. As shown in Fig. 5.1, the detection is performed perpendicular to the beam of light falling on the ion but in the same plane. The detector is a Hamamatsu PMT with an interference filter at 493 nm in front of it to allow detection of only 493 nm light. A magnetic field is applied to lift the degeneracy of the D levels, preventing the ion from falling into a 'dark state' and also to improve the Doppler cooling rate of the ion.

As is evident from the algorithm discussed in Chapter 3, this measurement requires pulses of 493 nm and 650 nm lasers to address the $6S_{1/2}$ to $6P_{1/2}$ transition and $6P_{1/2}$ to $5D_{3/2}$ transitions respectively and perform the necessary optical pumping. The amplitude modulation or pulsing is performed using Acousto Optic Modulator (AOM).

The AOMs are configured in double pass setup. This was done for two reasons- Firstly, it allows for scanning the laser frequency to optimize the detected fluorescence, without changing the beam direction and thus changing the intensity of the beam after an optical fiber. Secondly, it allows for a better cut-off when the rf drive of the AOM is in off state. Cut-off meaning the leak of laser power that is there even when the AOM is turned off. Presence of such leaks can seriously hamper the experiment because we will be driving transitions when we do not want to. For example, when the ion is being optically pumped from S to D via the 493 nm laser, if 650 nm laser light is leaking, it will depopulate the D-state back to the S-state. This leads to systematically wrong measurement of the D-state population and as theoretically Eq. 3.6 assumes only 493 nm pumping and absence of any re-pumping light, it will lead to a wrong ratio measurement.

Thus extreme prejudice was applied while setting up the AOMs to allow close to zero leakage of laser light when the AOMs are switched off. When measurements of laser power was performed, in the on state, the laser powers were $100~\mu W$ and $300~\mu W$ respectively for 493 nm and 650 nm. In the off state, the powers were around a few nano-Watts and in the zero order frequency, which was far away from the atomic resonance.

Fig. 5.2 shows the pulse sequence used for the measurement. The sequence is as follows-
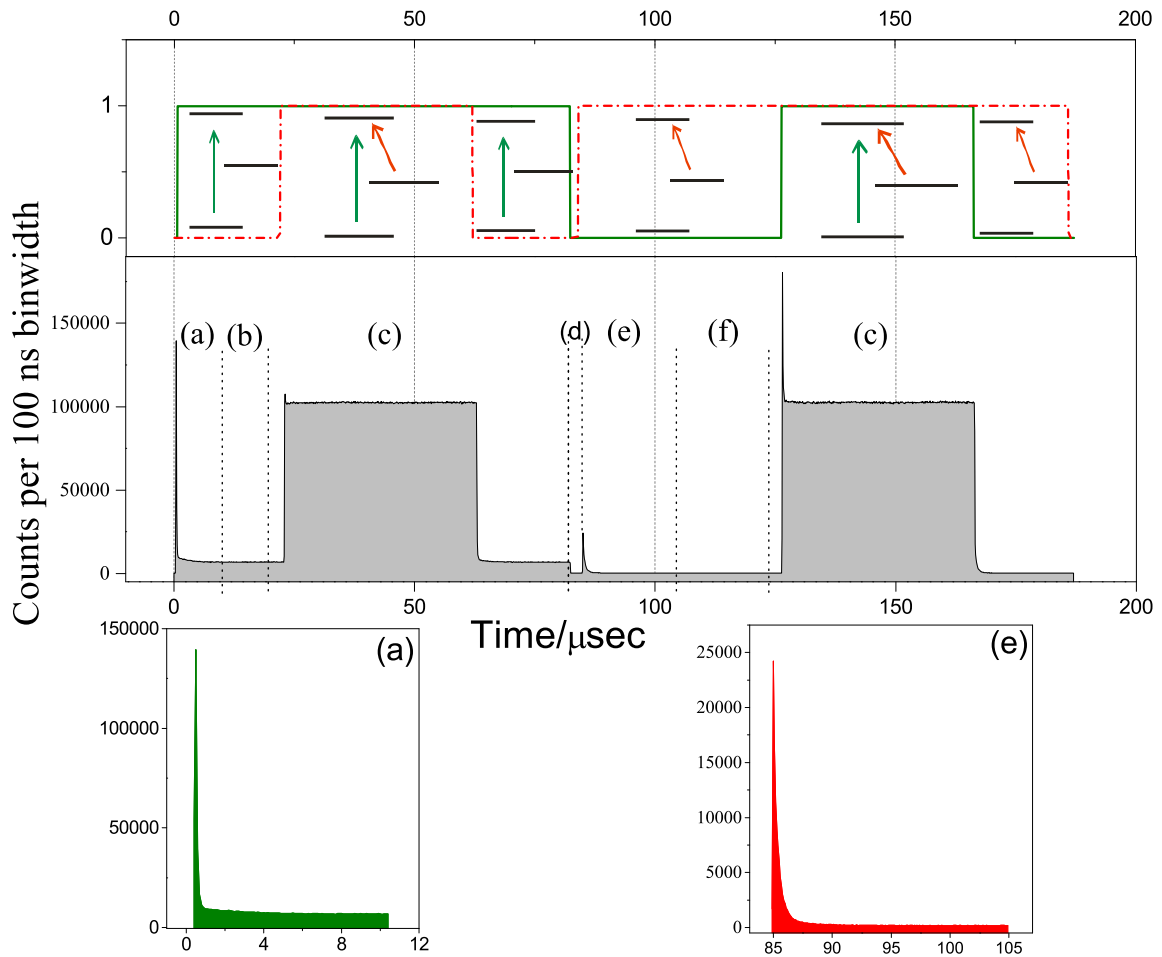
Figure 5.2: Experimental sequence and photon count measurement. The top part shows the experimental time sequence of the green and red pulses while the corresponding photon counts are shown in the middle panel. The sequence consists of (a) green photon measurement (only green laser on), (b) green background counts (green laser on), (c) cooling (both lasers on), (d) optical pumping to D-state (only green laser on), (e) red-repumping while green photon counting (only red laser on), (f) dark count measurement (both lasers off) and (c) another cooling pulse. The lower panel shows zoomed part of both the decay curves due to pumping and re-pumping of population.

1. The 493 nm laser was turned on.

2. Both 493 and 650 nm lasers were turned on.

3. 650 nm laser was shut down. Only 493 nm laser remained on.

4. 650 nm laser turned on after 493 nm laser shut down

5. Both 650 and 493 nm laser turned on.

6. 493 nm laser shut down. Only 650 nm laser remained on.

The first pulse drives the S to P transition and the green photon count during this process contains the branching fraction information (G_c denotes the number of photons emitted during this pulse). The ion is ensured to be in the ground state before this pulse is applied. The second pulse is for Doppler cooling. The third pulse is to ensure that the ion returns back to the state same as after S-P pumping once the cooling is complete. The fourth pulse drives the D to P transition and the green photons emitted during that pulse is used for the efficiency measurement (R_c denotes the number of photons emitted during this process). The fifth pulse is again a cooling cycle and the sixth pulse ensures that the ion is at the ground state, prepared for the start of a new cycle.

After the first pulse, the 493 nm laser is kept turned on for the same duration as the first pulse itself. This is to ensure that we measure the background green photon counts that are accumulated during the first measurement pulse (G_b). Similarly after the fourth pulse, the red laser was kept on for the same period of time to measure the background green photon counts (R_b). G_b and R_b were subtracted from G_c and R_c to obtain the true number of emitted green photons during each pulse, namely N_g and N_r.

From Chapter 3 we can see that the green photons counts during the first pulse contains the information about the branching ratio. If $< N >$ is the number of photons emitted during the first pulse, then

$$< N >= \frac{p}{1 - p}.$$

(5.1)

Now for C cycles of the experiment, with a detection efficiency of ξ and N_i number of ions in the sample, $N_g = C \, \xi \, N_i \, < N >$. However, for the fourth pulse, each ion will emit one single

green photon and thus $N_r = C \xi N_i$. Hence,

$$p = \frac{N_g}{(N_g + N_r)}. \tag{5.2}$$

5.2 Results and Analysis

We repeated the experimental sequence as mentioned in figure (5.2) for 25 different experimental sets, each of these measurements are having $2,000,000$ cycles. The total time required is mainly limited by the required statistical uncertainty which we targeted to be below 0.1% for the branching fraction measurement. In order to check for systematics we have performed about 50 similar experiments under different experimental conditions like varying magnetic field, laser intensity, added micro-motion, different Coulomb crystal structure *etc.*. None of the above varied condition showed variation in the value of r above $.1\%$ statistical variation. The laser intensity, however needs to be within certain range as too high value would saturate the PMT in short time scales and too low value would make the decay exponent too long for counting in a reasonable time. In order to check for any birefringence in our detection setup leading to disproportionate red to green counts, we on purpose changed the polarization angle of the linearly polarized green and the red beams showing no significant deviation beyond the statistical uncertainty. The only contribution to our uncertainty comes from the detector dead time, even though we worked in a regime where the rate is much below the saturation limit of the PMT and the counting electronics. The dead time leads to a calculable shift as well as uncertainty.

5.2.1 Estimation of Precision: Statistical and detector errors

One of the biggest limiting factor for the experiment is the loss of counts by the PMT because of the deadtime of the detector. Deadtime means the PMT cannot detect two photons having an arrival time gap smaller than that. The correction because of PMT deadtime is given as

$$N_{\text{corrected}} = N_{\text{measured}}(1 - \tau_{\text{D}} N_{\text{measured}}), \tag{5.3}$$

where τ_{D} is the deadtime of the PMT, N_{measured} is the number of photon counts measured in a given time interval and $N_{\text{corrected}}$ is the corrected number of counts.

For this measurement, there are 4 numbers which contribute to the final values of G_c, G_b, R_c and R_b. Let G_c^m, G_b^m, R_c^m and R_b^m be the measured values and G_c^c, G_b^c, R_c^c and R_b^c be the corrected ones. The final value of the branching ratio was obtained after careful measurement of the deadtime of the PMT. This is because the measurement uncertainty in the deadtime will affect the final precision of the value of the measured branching ratio.

The deadtime was measured by shining heavily attenuated laser light into the PMT. The power of the laser was measured by a commercial power meter from *Thorlabs* which had an uncertainty of .2 % as specified by the manufacturer. Under low light condition, the power and the measured number of counts within a certain time followed a linear relation. Thus from a linear fit of the initial points of the power vs count graph, one can obtain the values like detection efficiency and dark count which goes into measurement of the deadtime via non-linear fit.

Performing the fits, we obtained the deadtime as $54.0 \pm 0.3 \ ns$.

The measurement has been performed using a MCS card with a time bin of $100 \ ns$. However, the photon counts were not evenly distributed across all the bins, with the counts being higher when the pulse switched on, because of the initial population is in the ground state or the D state, depending on which pulse we are looking at and it tapered off exponential as more and more population was being pumped into the other state, not coupled to the probing laser. Fig. 5.3 shows a typical distribution of the photon counts across the bins.

Thus a more precise estimation of the actual counts and thus branching ratio can be obtained if the correction is applied to each bin separately. Also we calculated the statistical and deadtime uncertainty error for each bin and then for each section performed a root mean square sum of all the bins involved for each of the counts which go into the branching ratio measurement.

If N_i is the count of one bin, then the corrected values of that bin is

$$N_i^a = N_i/(1 - \tau_d \ N_i) \tag{5.4}$$

85
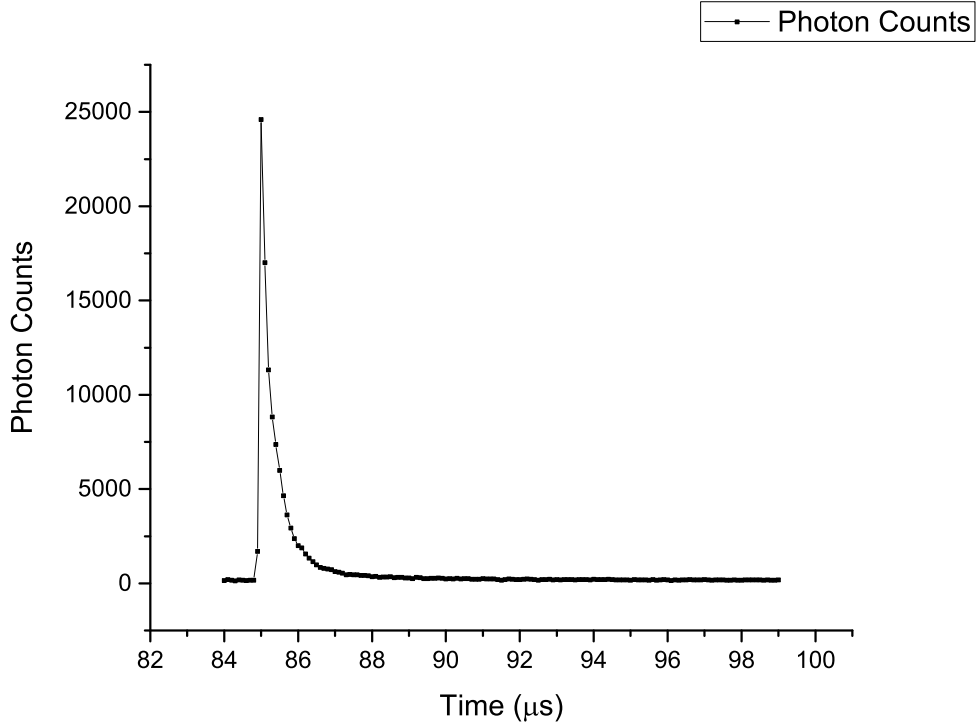
Figure 5.3: Distribution of photon counts per bin of MCS card. The time starts from the time 493 nm or 650 nm laser is switched on.

and the error arising from that bin is

$$\delta N_i = \delta N_i \left(\frac{1}{1 - \tau_d\, N_i} + \frac{N_i\, \tau_d}{(1 - N_i\, \tau_D)^2} \right) + \delta\tau_D\, \frac{N_i^2}{(1 - N_i\, \tau_D)^2}. \tag{5.5}$$

So the correction to the value of the branching ratio is obtained by summing N_i^a over the bins relevant for G_c, G_b, R_c and R_b. Now, since $N_g = G_c - G_b$, $\delta N_g = \sqrt{(\delta G_c)^2 + (\delta G_b)^2}$, assuming root mean square addition.

δG_c is obtained by root mean square summing of δN_i over the relevant bins. For all the four sections relevant for counting,

$$\delta G_c = \sqrt{\sum_i \delta N_i^2}. \tag{5.6}$$

The equation is similar for G_b, R_c and R_b.

The final step is obtaining the statistical uncertainty is using the Central Limit Theorem. This allows for more precise knowledge of the means of multiple samples of a given population. In this

Table 5.1: Error budget for the branching fraction measurement.

Parameter	shift	uncertainty
Detector dead time $(54 \ ns)$[1]	$+5 \times 10^{-3}$	1.6×10^{-4}
Photon counting (statistical)		1.9×10^{-4}
Photon counting (finite measurement time)	–	–

case, we have 27 sets of measurements, each giving a certain value of the mean and standard deviation or error calculated using the above formulae. Now, because of the central limit theorem and since the sample data are independent of one another, the effective uncertainty of the measurement is given by the mean of the error over 27 samples, divided by square root of one minus the sample number, which in this case is 26.

However, one should be careful while applying the central limit theorem. The theorem applies only to statistical uncertainty and not to the uncertainty contributed by our knowledge of the deadtime of the detector which is a systematic uncertainty. The statistical uncertainty is extracted by putting τ_D as zero and also $\delta\tau_D$, the uncertainty of the deadtime, as zero. Central Limit Theorem was applied on that uncertainty which have the statistical uncertainty alone. The contribution of the deadtime uncertainty is contained in the term along with $\delta\tau_D$ and that provides the uncertainty contribution coming from the deadtime, as is shown in Eq. 5.5.

The measured values of the branching fractions, along with the best literature value of the upper state life-time [113], 7.92 ± 0.08 ns, provides the transition probability as well as the matrix elements of the relevant transitions by following the procedure in [25]. In table (5.2), we show our results along with the values measured or calculated till date. The best measured experimental data on these transitions are limited to about 5% uncertainties on the matrix elements. On the contrary, since the experimental proposal by Fortson [53] for the possibility of measuring the atomic PNC in barium ion, the accuracies on the theoretical values of the matrix elements has improved significantly aiming towards below one percent level where many-electron correlation effects become significant. As can

be seen from Fig. 5.4, the theory values scatter within the experimental uncertainties while the claimed theoretical uncertainties are significantly lower than the previous experiments [108]. Our measurements, for the first time, provides the values below a percent limit, thereby allowing the theories to be compared at a similar uncertainty level. The $S - P$ transition probability is rather close to the theory values of [25,116,117] but seems to quite off from the value by [108]. On the other hand, the $P - D$ transition probability is close to the values calculated by [108, 116, 117] while deviating significantly from [116]. These theories mostly consider all orders in perturbation but limited to certain number of collective excitations, therefore it is now possible to make a comparative study of these different approaches in view of the experimental data. The branching fractions themselves are important for estimating the abundance of barium in solar and stellar atmosphere [111] which provides insight into the process of nucleo-synthesis, especially of heavy elements. Our measured branching fractions are 0.73037 ± 0.0002 and 0.26963 ± 0.0002 for the $P - S$ and $P - D$ branches respectively [120].
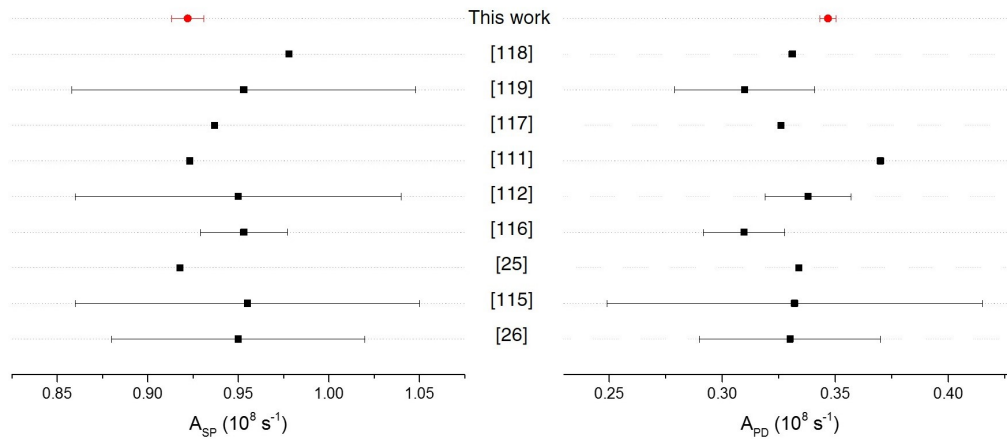

Figure 5.4: A comparison of different measurements and theory values of the dipole transition probabilities for $S - P$ and $D - P$ transitions. The hatched area provides the value and 1σ confidence band of this measurement. The values which do not have error associated with them are theory values while values in [115] and [119] are compilation results of earlier experiments.

Table 5.2: Comparison of measured vales in this work with previously measured and calculated values.

Transition involved	Branching fraction	Transition probability $\times(10^8 s^{-1})$	Transition matrix	References
$\left\lvert P_{\frac{1}{2}}\right\rangle - \left\lvert S_{\frac{1}{2}}\right\rangle$	0.735 ± 0.021	0.95 ± 0.07	3.35 ± 0.11	[118]
		0.955 ± 0.095	3.36 ± 0.15	[119]
		0.9178	3.300	[117]
	0.756 ± 0.012	0.953 ± 0.024	3.362 ± 0.038	[111]
		0.95 ± 0.09	3.36 ± 0.14	[112]
		0.9232	3.309	[116]
		0.9368	3.333	[25]
		0.953 ± 0.095	3.36 ± 0.15	[115]
		0.978	3.405	[26]
	0.73037 ± 0.00025	0.922 ± 0.009	3.306 ± 0.014	This work
$\left\lvert P_{\frac{1}{2}}\right\rangle - \left\lvert D_{\frac{3}{2}}\right\rangle$	0.265 ± 0.021	0.33 ± 0.04	2.99 ± 0.18	[118]
		0.332 ± 0.083	3.00 ± 0.37	[119]
		0.334	3.007	[117]
	0.244 ± 0.012	0.3097 ± 0.018	2.895 ± 0.084	[111]
		0.338 ± 0.019	3.025 ± 0.085	[112]
		0.37	3.165	[116]
		0.326	2.971	[25]
		0.31 ± 0.031	2.90 ± 0.15	[115]
		0.331	2.993	[26]
	0.26963 ± 0.00068	0.3468 ± 0.0036	3.064 ± 0.016	This work

Chapter 6

Coherent Manipulation of Quadrupole Transition: Towards Quadrupole Moment Measurement

In this chapter, driving dipole forbidden transition between $6S_{1/2}$ and $5D_{5/2}$ levels is discussed. One of the main tools to explore this transition is a narrow linewidth 1760 nm laser, development of which is presented in Chapter 4. Here the performance of the laser system and its limitations are discussed in view of measuring the quadrupole moment of the D orbital for the Ba^+. The measured quadrupole moment addresses two physical problems as discussed in Chapter 3. One of them is to probe the electronic wavefunction of the D-state as the quadrupole moment is the expectation value of the quadrupole moment operator in the D-state [25]. Secondly, measuring the quadrupole moment allows us to implement the geometric phase generation protocol as proposed in Section 3.3 and estimate the possible systematics in the parity violation experiment that uses interference between the quadrupole transition and the PNC dipole transition [53]. The first and foremost requirement is to measure the transition frequency between S and D state to a precision which is sufficient to resolve the frequency shift due to quadrupole interaction. In the following, the system has been developed to perform such a measurement in the near future. In addition, the present system allows fast qubit operations with low decoherence thereby opening up to possibility of using Ba^+ as a qubit near the telecom wavelength.

6.1 Experimental Protocol

6.1.1 Quantum Jumps

One of the first indication of the interaction of the 1760 nm laser with barium ion is the detection of quantum jumps, Fig. 6.1 [121]. Quantum jumps are sudden fall of the fluorescence level of the trapped ion due to the shelving of the electron from the ground state to the metastable state $D_{5/2}$, which is disconnected with the fluorescence generating lasers. In this case, the fluorescence is observed by applying the 493 nm and the 650 nm laser and the drop in the fluorescence happens when the 1760 nm laser shelves the electron into the $D_{5/2}$ level. To observe quantum jumps, we bring the laser close to the known wavelength value, using wavemeter with a resolution of 10 MHz and suitable AOMs. The rate at which the quantum jumps occur depends on the detuning of the laser from the atomic transition, linewidth and the intensity of the laser at the ion position. For our measurement, the ion fluorescence is measured with in a time bin of 100 ms. To check that the jumps are due to 1760 nm laser and not due to collisions with background gas molecules (which can reduce fluorescence due to sudden transfer of energy to the ion, which in turn heats it up and doppler shifts the transition away from the cooling laser), we switch on the 614 nm laser, which brings the electron back to the S level via dipole coupled paths, making the jumps disappear.

As can be seen in Fig. 6.1, the counts sometimes drop to a value which is higher than the background counts. This is because the 1760 nm laser coherently drives the transition, not only to the $5D_{5/2}$ level but also back to the ground state increasing the fluorescence by coupling to the cooling and repumping lasers. However, that happens sporadically and that is why sometimes there is a long period of darkness of the fluorescence count and sometimes there is a partial drop in the fluorescence.

Once the quantum jumps are detected, we can optimize our alignment to increase the intensity at the ion location. When the light is optimally aligned the rate of jumps increases a lot and the net fluorescence collected in the 100 ms window decreases significantly, as shown in Fig. 6.2. Turning on the 614 nm laser brings the fluorescence back to the original level.

While the $5D_{5/2}$ level has a lifetime of several seconds [23–25], the dark state does not last that long because the 1760 nm laser coherently drives the transition between the $5D_{5/2}$ and $6S_{1/2}$ levels. Closer the wavelength, higher the power, narrower the linewidth and better the alignment, more faster is this cycling between S and D levels.
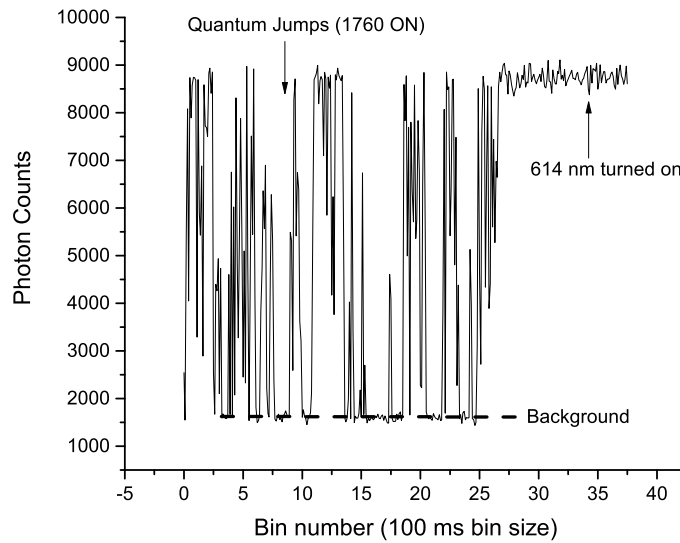
Figure 6.1: Observed quantum jumps. The ion is sporadically excited to the $5D_{5/2}$ state and thus gets decoupled from the 493 nm and 650 nm laser. This leads to a drop of the fluorescence level. The electron is again brought back to the ground state by stimulated emission by the 1760 nm laser. Thus we have much smaller 'dark' periods compared to the natural lifetime of the level. Also because of this cycling, sometimes the fluorescence does not drop to the background level.

6.1.2 Temporal Pulse Sequence to Address Quadrupole Transition

For driving and detecting the quadrupole transition, the following pulse sequence is used, as shown in Fig. 6.3-

1. Cooling: In this segment, 493 nm, 650 nm and 614 nm lasers are switched on for $100\ \mu s$.

2. State preparation: In this segment, the 650 nm and 614 nm lasers are switched on. This prepares the ion in the ground state. Optical pumping, when applied, is also switched on during this time. Optical pumping is transferring all the population into one of the Zeeman sub-levels of the ground state by using a circularly polarized 493 nm laser, applied using the 45° viewports.

3. S-D transition drive: In this segment, the 1760 nm laser is turned on.

4. Detection: In this segment, the 493 nm and 650 nm lasers are turned on. This segment detects if a transition has taken place or not. If the ion is on the $5D_{5/2}$ level, then there would be no fluorescence (off state). If however, the 1760 nm laser cannot excite the S-D transition, the fluorescence level will be high (on state).
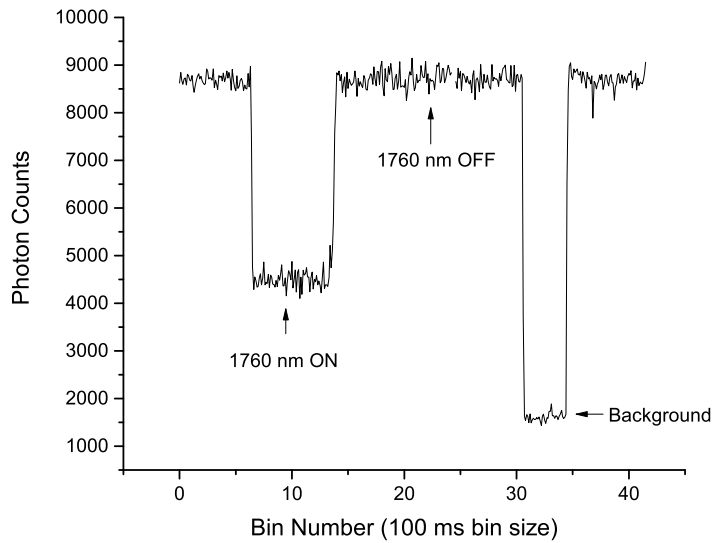
93

Figure 6.2: Improvement of alignment of the 1760 nm lasers increases the frequency of transfer from the S to D states. This leads to greying out of the fluorescence level, that is for a given bin size, the photon counts reduces significantly such that the average count is significantly lower than the average count with only 493nm or 650 nm laser. The higher count can be regained by turning of the 614 nm laser which brings the electron back to the ground state fast enough to restore the fluorescence level.

State detection is a projective measurement and hence the probability of finding the ion in the ground state is measured by preparing the ion in the same state multiple times prior to each measurement. The efficiency of each ground state determination is 100% provided the threshold counts determining the on and off state is properly set. To determine the count threshold, the following procedure is adopted- First the 1760 nm laser is blocked and the ion fluorescence count for the time period of the detection segment is measured. Also the background scattering for the same time period is measured by switching off the repumping lasers. The threshold is then set to a value, between the fluorescence counts and the background count. Thus if the ion is in the on state, the count will be larger than the threshold, and if it is in off state it will be lower. Fig. 6.4 shows the counts in the presence and absence of the ion and a distinct difference between the counts in the two conditions, which allows to set a threshold to estimate the on or off state of the ion with 100% efficiency. There is an optimal state detection time which is determined by reducing the time of the detecting pulse while ensuring there is no overlap of the on and off state photon count number. This reduces the total cycle time without compromising the state detection efficiency of 100%. Fig. 6.4 is not an optimal value.
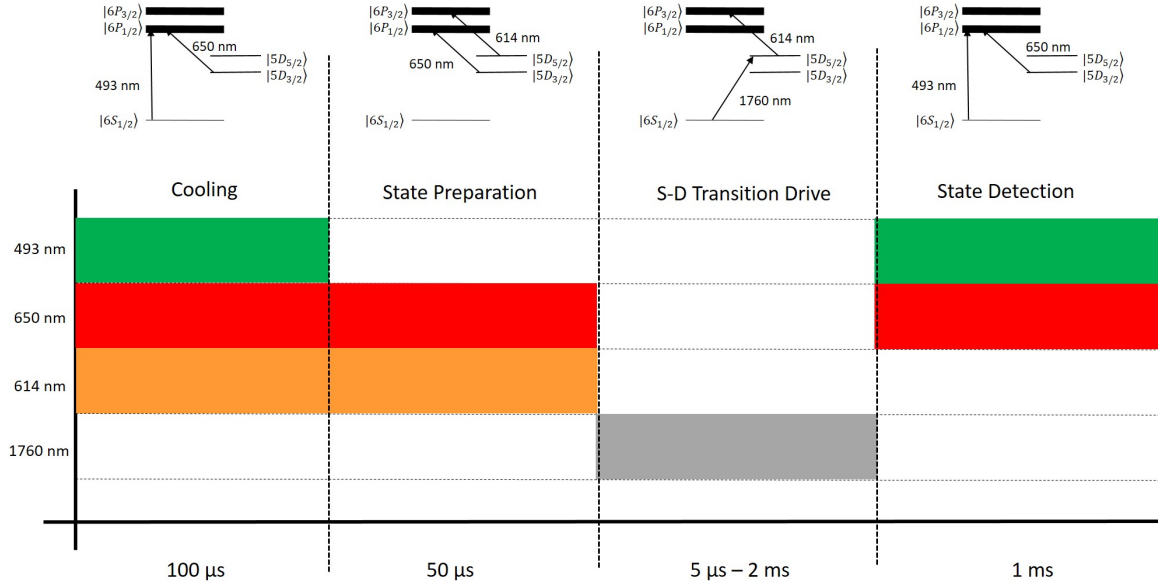
Figure 6.3: Pulse sequence for detecting quadrupole transition

In order to obtain the quadrupole transition spectra, the above sequence is repeated a 100 times for each frequency of the 1760 nm laser in order to obtain the state transfer probability. This produces one data point in the spectrum as shown in Fig. 6.5. After that the frequency is shifted by a predetermined step size and the process is continued.

6.1.3 S-D Transition

Fig. 6.5 shows the spectrum of the quadrupole transitions measured over a frequency range of 15 MHz. Given the geometry of the system as is shown in Fig. 6.6, that is the angle between the magnetic field (which determines the quantization axis) and the direction of beam propagation and the angle between magnetic field and the polarization of light, we know that the transitions with $\Delta m = 1$ will be excited while other transitions are suppressed as shown in Chapter 3, Fig. 3.4.

Now zooming in on the $m = -\frac{1}{2} \rightarrow -\frac{3}{2}$ line, as shown in Fig. 6.7, a linewidth of 3.5 kHz is obtained. This is the fourier limited linewidth of the 1760 nm light used, which is pulsed with a pulse length of 100 μs.

Fig 6.8 shows the reduction of the linewidth depending on the duration of the 1760 nm pulse of light. This shows that the width of the transition is limited by the fourier transform width of the 1760 nm light alone. However, with longer pulse, decoherence effects starts playing a role, which is why the pulse depth reduces with longer pulse duration.
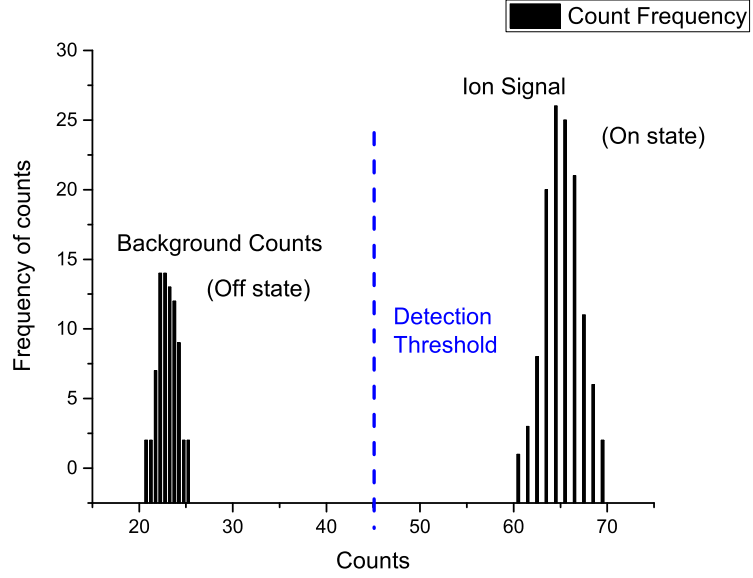
Figure 6.4: Histogram of counts of the ion signal and the scattered light signal. As can be seen the counts in the presence and absence of the ion fluorescence is distinctly separated which enables state detection with 100% efficiency.

6.2 Calibration of Magnetic Field Generating Coils

The Zeeman shift of the ground state is given by

$$\Delta E_S = -g_S m_j^S \mu_B |B| \tag{6.1}$$

and that for the D level is given by

$$\Delta E_D = -g_D m_j^D \mu_B |B|. \tag{6.2}$$

So the shift of the transition line is given by $\Delta \nu = E_D - E_S$ or

$$\Delta \nu = (g_S m_j^S - g_D m_j^D) \mu_B |B|. \tag{6.3}$$

Let $\mathcal{G} = g_S\, m_j^S - g_D\, m_j^D$. The g factors for S and D states are 2.0024906 [122] and 1.2020 [123] respectively. Bohr magneton is $\mu_B = 1.40\, MHz/Gauss$.

Let the magnetic field generated by each coil pair as a function of current be $B_i = \kappa_i I_i$ for the
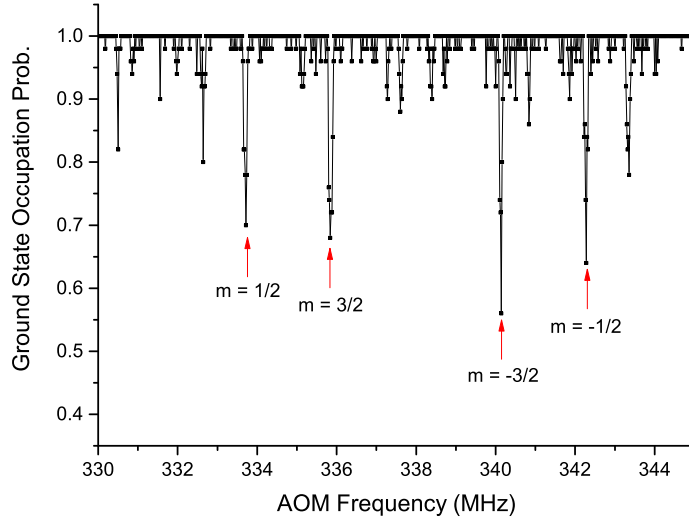
96

Figure 6.5: $6S_{1/2}$ to $5D_{5/2}$ transition lines for barium ion. The four narrow lines corresponding to $\Delta m = \pm 1$ transitions allowed by the geometry, as shown in Fig. 6.6, that is the angle between the magnetic field and the propagation direction of 1760 nm light and the angle between magnetic field and the polarization of the light.

i^{th} channel, as is shown in Fig. 6.6 where κ_i is the proportionality constant for a given pair of coils.

We first switch on one pair of coils and plot the S-D transition spectrum for different coil currents, which are always changed by the same amount. Now by looking at the ratio of relative shifts, it was possible to identify the zeeman levels involved for each transition lines, using the knowledge of the effective $\mathcal{G}$ factor. Once the zeeman levels involved has been identified, the shift is plotted as a function of the current, which is given by

$$\Delta\nu = \mathcal{G}\mu_B\kappa_i I_i. \tag{6.4}$$

Table 6.1 gives the values of $\mathcal{G}$ for different lines. From the value of $\mathcal{G}$ and that of Bohr magneton, we can obtain the value of κ_i.

Fig. 6.9 shows the S-D transition spectrum as a function of coil currents for the two pairs of coils, designated Ch2 and Ch3 in Fig. 6.6. We focus on the transition between $S_{-1/2} \to D_{-5/2}$ levels. From the linear fit of the peak frequency as a function of the current, the slopes obtained are 1.464 MHz/A for Ch2 and 1.452 MHz/A for Ch3. Now from Eq. 6.4, we obtain the calibration for the coils as $.522$ Gauss/A for Ch2 and $.518$ Gauss/A for Ch3.
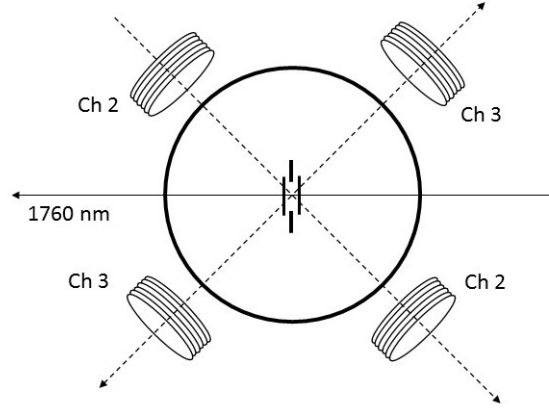
Figure 6.6: Orientation of magnetic field generating coils, 1760 nm beam direction and the ion trap. It also shows the pair of coils considered as channel 2 and the pair considered as channel 3.

m_j^S	m_j^S	$\mathcal{G}$	Δm
$+1/2$	$+5/2$	$+\frac{1}{2}g_S - \frac{5}{2}g_D \;=\; -2.0037547$	$+2$
$+1/2$	$+3/2$	$+\frac{1}{2}g_S - \frac{3}{2}g_D \;=\; -0.8017547$	$+1$
$+1/2$	$+1/2$	$+\frac{1}{2}g_S - \frac{1}{2}g_D \;=\; 0.4002453$	0
$+1/2$	$-1/2$	$+\frac{1}{2}g_S + \frac{1}{2}g_D \;=\; 1.6022453$	-1
$+1/2$	$-3/2$	$+\frac{1}{2}g_S + \frac{3}{2}g_D \;=\; 2.8042453$	-2
$-1/2$	$+3/2$	$-\frac{1}{2}g_S - \frac{3}{2}g_D \;=\; -2.8042453$	$+2$
$-1/2$	$+1/2$	$-\frac{1}{2}g_S - \frac{1}{2}g_D \;=\; -1.6022453$	$+1$
$-1/2$	$-1/2$	$-\frac{1}{2}g_S + \frac{1}{2}g_D \;=\; -0.4002453$	0
$-1/2$	$-3/2$	$-\frac{1}{2}g_S + \frac{3}{2}g_D \;=\; 0.8017547$	-1
$-1/2$	$-5/2$	$-\frac{1}{2}g_S + \frac{5}{2}g_D \;=\; 2.0037547$	-2

Table 6.1: Table of effective $\mathcal{G}$ factors for all the possible quadrupole transitions between the zeeman levels of $6S_{1/2}$ and $5D_{3/2}$.

6.3 Estimating Ion Temperature

As described in Eq. 2.30, the average phonon number of the trapped ion after doppler cooling can be obtained by measuring the excitation probability of the red and blue sidebands of the S-D transition.

Fig. 6.10 shows the experimental data for the probability of excitation of the sidebands. The trap frequency is 1.75 MHz. From the graph we obtain $R = 0.85$ giving the average phonon number to be $\overline{n} = 5.67 \pm 0.31$. Based on the properties of Barium ion and assuming the ion temperature is the doppler limit of the temperature, for this trap frequency, the theoretical estimate of the average phonon number is 5.21 which is quite close to the experimental value obtained via measurement of the sideband excitation probabilities.

In terms of absolute temperature, this translates to a temperature of 518 μK.
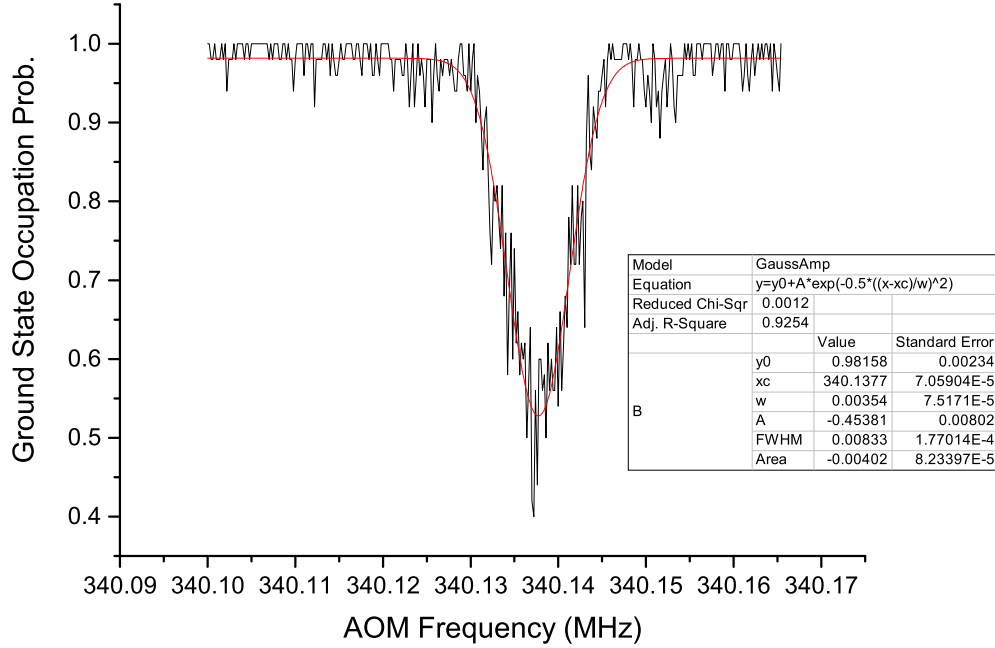
Figure 6.7: High resolution scan of the $m = -\frac{3}{2}$ line. The transition is fitted with a gaussian peak function to obtain the linewidth of the transition. As the fit shows, the linewidth is 3.5 kHz.

6.4 Linewidth Reduction and Magnetic Field Noise

Once the basic protocols are established, the main task is to obtain the narrowest linewidth of the S-D transition. The theoretical limit is the linewidth of the 1760 nm laser. However, the dephasing and noise in the system prevents achieving this linewidth limit because of decoherence effects in the system.

One of the biggest sources for noise in quantum systems is the magnetic field noise, especially when one is working with a magnetic field sensitive transition [125, 126]. Magnetic field sensitive means that the effective g-factor is non-zero for the levels between which the transition is driven. The noise may originate from ambient magnetic field fluctuating at 50 Hz due to nearby electronics being fed from the power line as it may as well be the residual current noise at 50 Hz supplied by the current supply to the magnetic field generating coils. Two solutions can be adopted to get rid of this noise. One is to shield the vacuum chamber with mu-metal which blocks any external magnetic field. However, this cannot eliminate the noise coming from the magnetic field generating coils.

The second way to eliminate the effect of 50 Hz noise is synchronizing the experiment to the
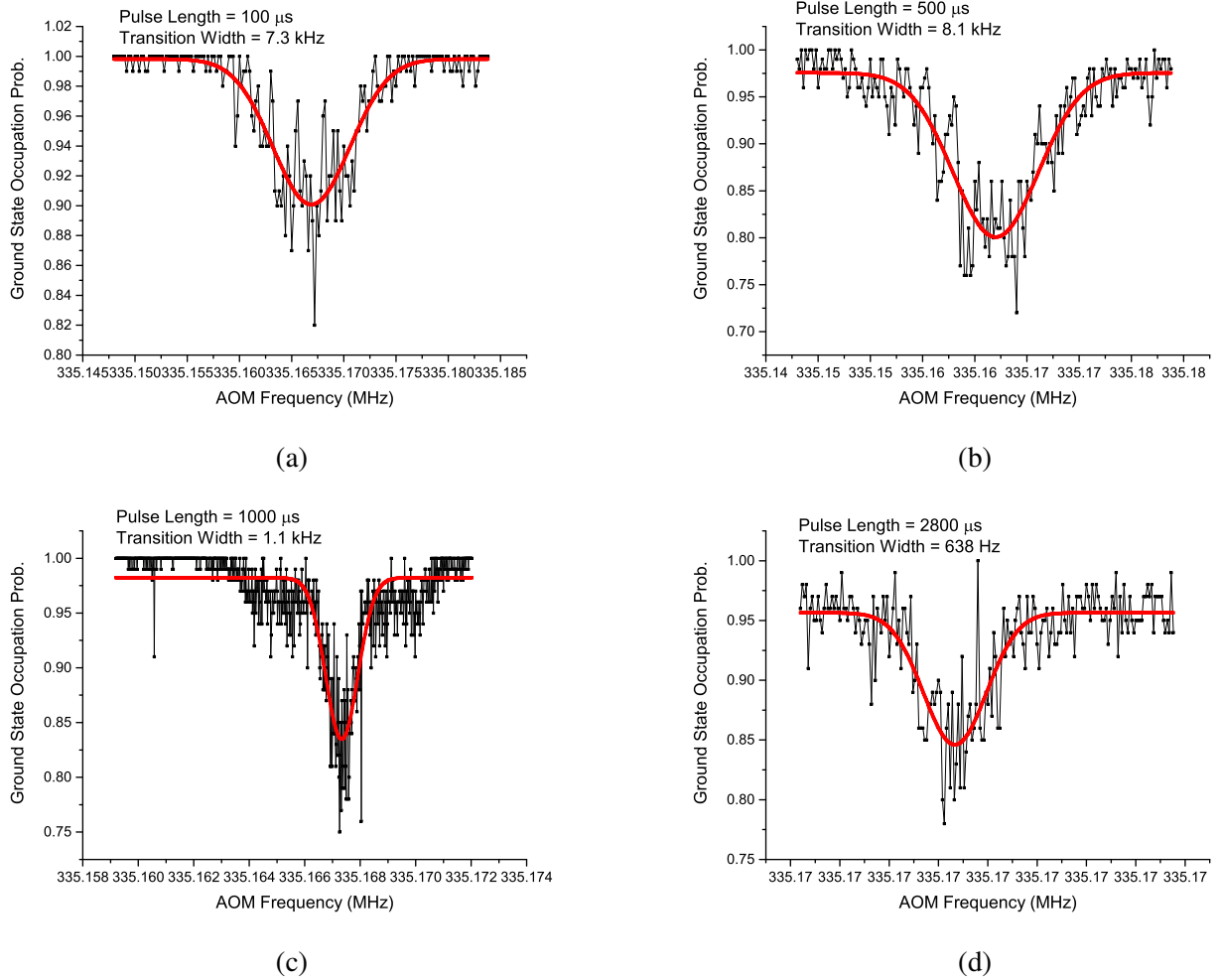
Figure 6.8: Figures showing reduction of the linewidth of the quadrupole transition as a function of the pulse length used for excitation of the 1760 nm transition. Longer pulse duration leads to reduction of the linewidth because the linewidth is fourier limited.

line frequency, which is used for the work in this thesis. This means that the experimental pulse sequence is always started at a given phase of the AC line frequency. Since all the experiments with the quadrupole transition is some form of probability measurement, locking the experiment with the line frequency allows one to measure these probabilities at exactly the same magnetic environment, with respect to the phase of the fluctuations due to the AC power lines . Fig. 6.11 shows the general building blocks for triggering the experiment with the AC line frequency.

Fig. 6.12 shows the effect of 50 Hz triggering. When triggered, the coherence of the system improves dramatically leading to a peak with a greater depth indicating lower decoherence effects during the exposure time. However, the linewidth in these measurements are Fourier limited by the excitation pulse length.
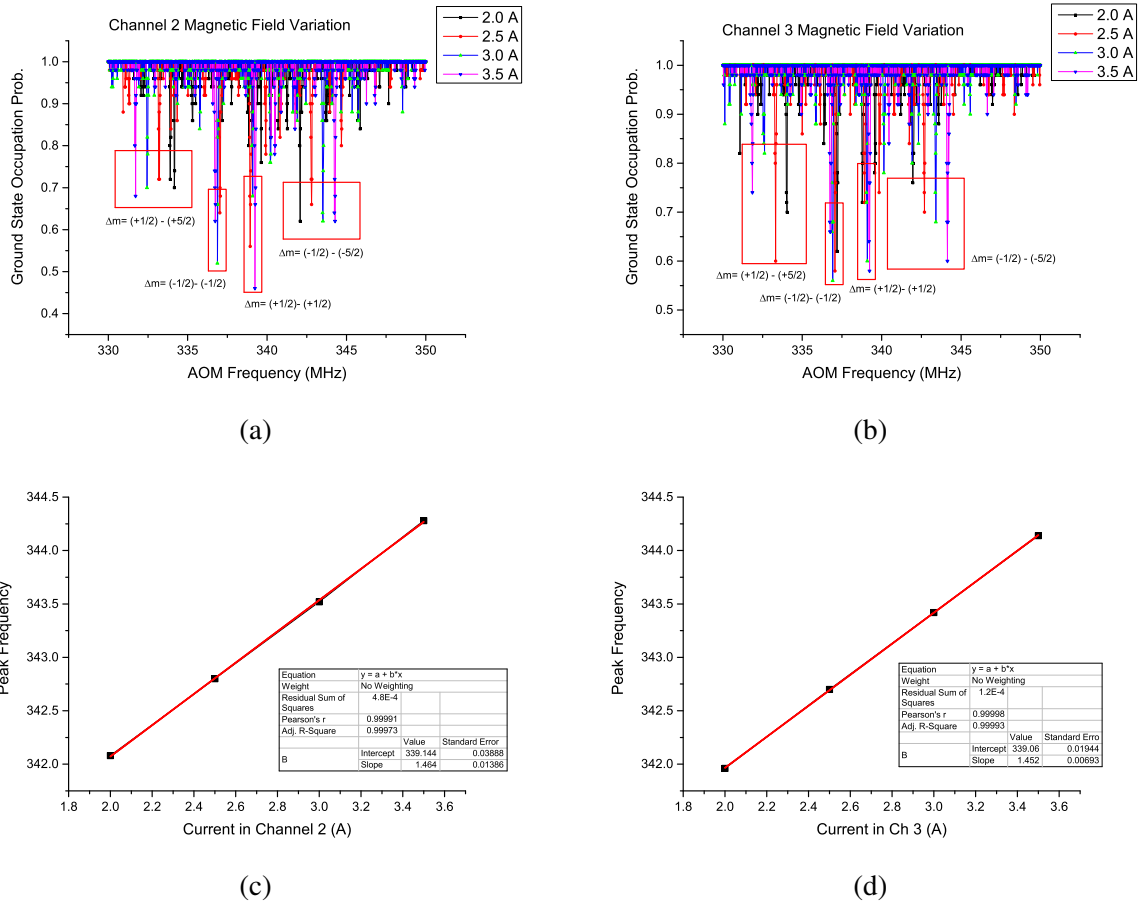
100

Figure 6.9: Figures showing S-D transition spectrum with different coil currents for different pairs of coils. The figures (c) and (d) show the peak frequency as a function of the coil currents. The slope is obtained by linear fit of the peak frequency as a function of the coil currents.

6.4.1 Coherence Time: Ramsey Measurement

The effect of 50 Hz can be observed more prominently during Ramsey interferometry of the transition in question, which is described in Section 2.3.1.

Fig. 6.13 shows the effect of the 50 Hz synchronization on the evolution of the system. Keeping all the parameters constant, without the line trigger, the coherence time is $178\ \mu s$ while triggering with 50 Hz increases the coherence time to about 6 ms. This conclusively shows that one of the limiting factors in our system is the residual magnetic field noise at 50 hz. Synchronization with the line frequency improves on the decoherence effect arising from magnetic field fluctuations. The fact that decoherence time after synchronization is about 6 ms also sets a limit on the present technical noise in our system which is most likely magnetic field noise, arising from sources different from the
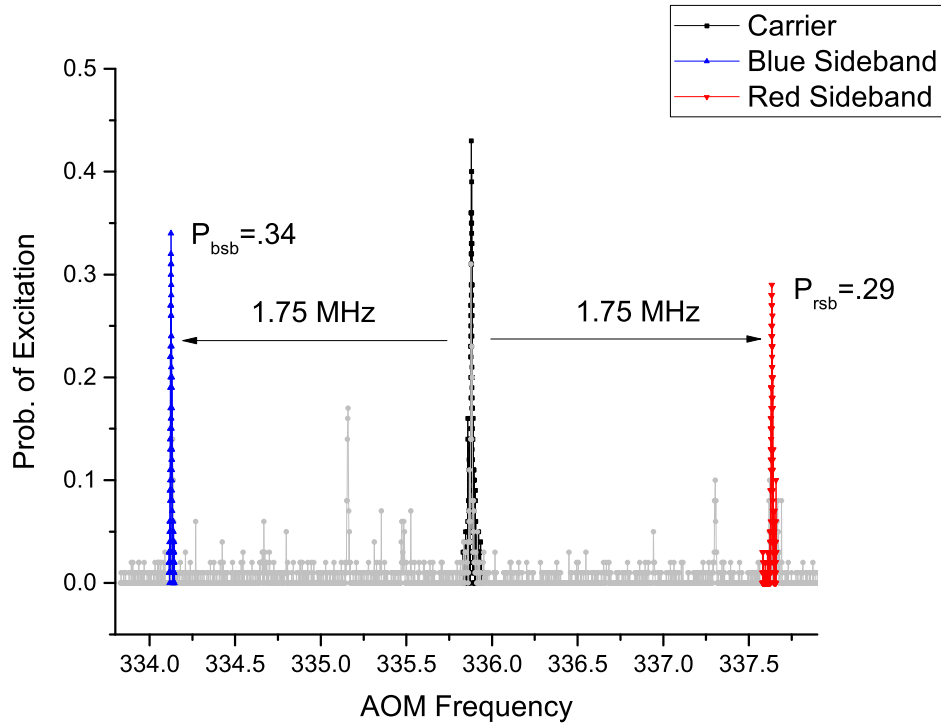
101

Figure 6.10: Main carrier peak and the sideband as is seen during spectroscopy of the quadrupole transition. The peaks are separated by 1.75 MHz, the trap frequency.
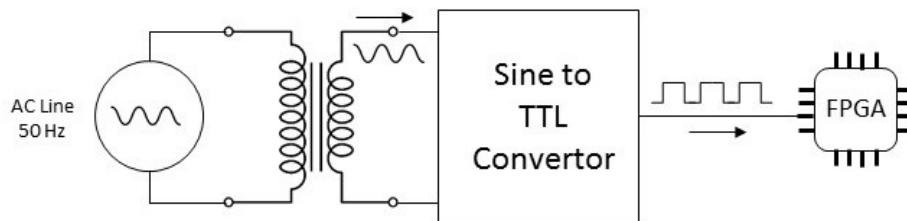

Figure 6.11: Setup for synchronizing the experiment with the line frequency.

power line frequencies.

6.4.2 Noise Limited Transition Linewidth

The power line synchronization of the experiment led to improved coherence of the system which in turn allowed us to achieve much lower linewidth of the quadrupole transition than was possible before. Increased coherence time allowed for longer exposure time of 1760 nm laser which in turn reduced fourier limited linewidth of the transition. It also increased the depth of the transition peak, which led to lower intensity requirement for 1760 nm laser which in turn allowed for longer Π times.
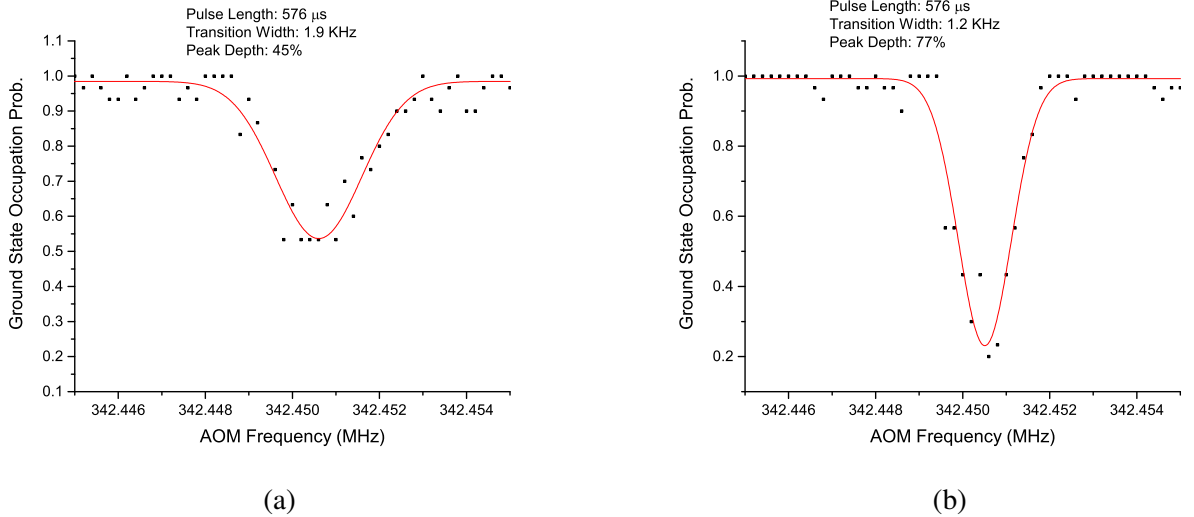
Figure 6.12: Graphs showing the effect of 50 Hz triggering. With the trigger active, the peak width reduces slightly. However, the more prominent effect is the increase of depth of the peak. This is because of reduced decoherence during the exposure time of 576 μs. All other parameters remained the same for the two measurements.

Fig. 6.14 shows the transition after synchronizing the experiment with the line frequency. This allowed to obtain transition linewidth of the order of 300 Hz with an exposure time of 2 ms. This the lowest linewidth which was achievable and the limit seems to be the maximum exposure time which was possible to use without losing the coherence of the system, a limit which is possibly set by residual magnetic field noise or laser intensity noise, sources of which are currently being investigated. It has to be kept in mind that the transitions are magnetic field sensitive and hence 300 Hz linewidth is rather promising.

This system is currently sufficient to measure the quadrupole moment of the D state of the Barium ion, which is the next goal of this experiment.

6.5 Optical Qubit at 1760 nm

Rabi oscillation is the oscillatory behaviour shown by a two level quantum system when it is coherently driven by an electromagnetic field. For example, a two level atom driven by the laser connecting the two levels [48]. In this process, the population is transferred from one level to another in a sinusoidal fashion, with the frequency of the sinusoidal oscillation depending on the intensity and frequency of the laser as well as the matrix element connecting the two levels. In a Bloch sphere all two level rotations are equivalent to single qubit operations. Therefore a fast rotation allows faster single qubit gate. As 1760 nm is very close to the presently used telecom wavelength, this single
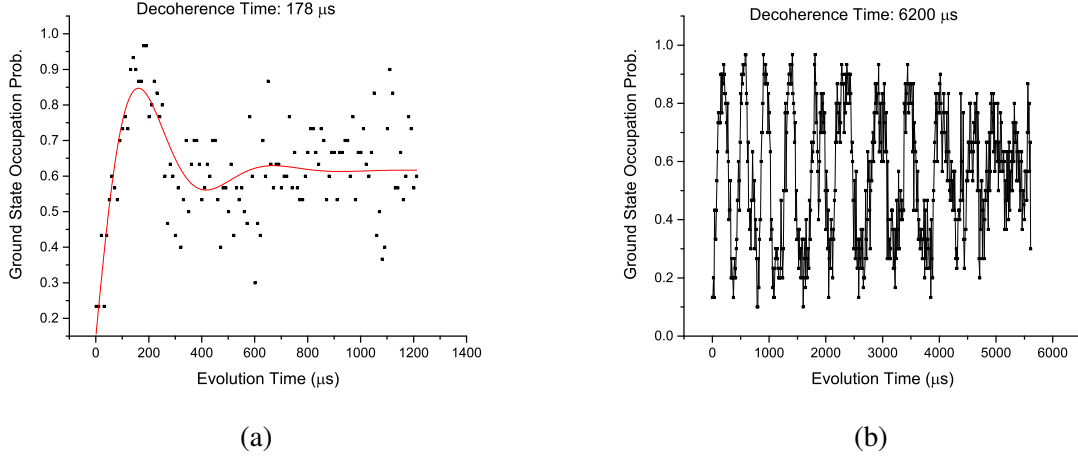
Figure 6.13: Effect on 50 Hz triggering on free evolution of the system. For both the measurements, the intensity and frequency of the laser as well as the magnetic field and trapping parameters are kept the same. Triggering with 50 Hz improves the free evolution coherence time dramatically. There is however a very low frequency noise in the system because of which with increasing evolution time, the period of the oscillation slowly changes.

qubit promises possible applications as both qubit and memory. In the following parts we investigate properties related to an atomic qubit in Ba^+. As compared to other systems, here all the lasers are diode lasers and hence in principle can be integrated for scaling up of the devices.

The Rabi frequency is obtained by using the same pulse sequence that is used for spectral measurement, Fig. 6.3. However, unlike the spectral measurement, here the frequency is kept constant at the resonance and the 1760 nm exposure time is scanned while the state of the atom at the end of the exposure is measured.

Fig. 6.15 shows a typical Rabi oscillation between two zeeman resolved levels of the ground state and the excited state, namely $6S_{1/2}$ and $5D_{5/2}$.

One of the characteristics of Rabi oscillation is the decay of the process, as is shown in Fig. 6.16 which is because of decoherence processes. Decoherence is the process by which a quantum system loses its quantum behaviour [127, 128]. It is primarily caused by external magnetic field noise for magnetic field sensitive transition, noise in the light intensity and frequency driving the transition, spontaneous emission and for trapped ion, the characteristics of thermal distribution such as average phonon number and Lamb-Dicke parameter.

For a trapped ion, the magnetic field fluctuation can be mitigated by synchronizing the experi-
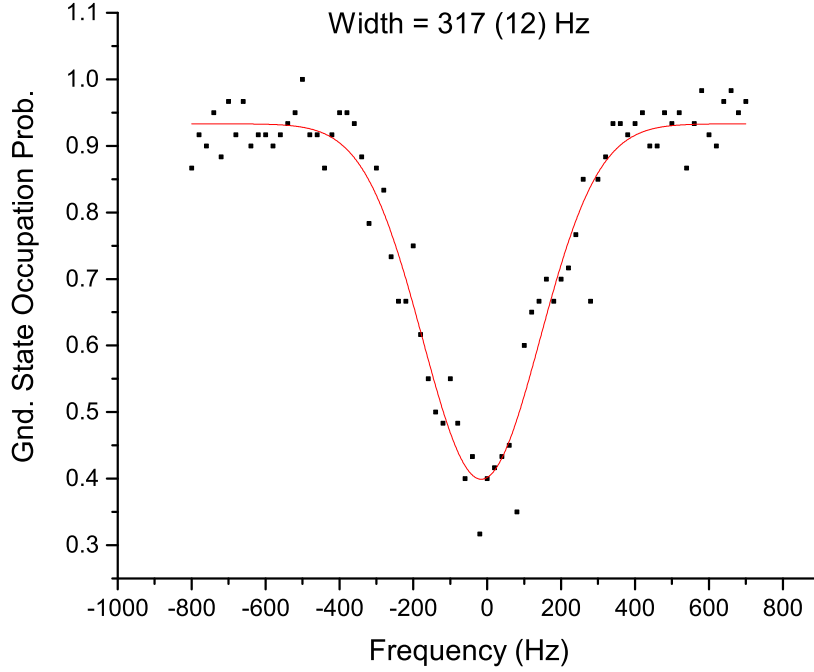
Figure 6.14: Noise limited linewidth for the transition between $6S_{1/2}$ and $5D_{5/2}$. The linewidth of the transition is 317 Hz.

ment with the AC line frequency as described before. For the $D_{5/2}$ level in question, the lifetime is of the order of 30 s. This means that spontaneous emission does not have a significant contribution in the experimental time scales which is of the order of few milliseconds. The fluctuation of the light frequency is suppressed by locking the laser of a high finesse ultrastable cavity and there is no significant fluctuation of the light intensity. Thus it can be concluded that the primary dephasing process is governed by the thermal distribution of the ion in different motional modes of the trap. This implies that from the measured Rabi oscillation, by plugging in the average phonon number measurement that we obtained before, we can extract the value of the Lamb Dicke parameter of the trapped ion using Eq. 2.26 [129].

Fig. 6.17 is the fitting of Eq. 2.26 to the experimental Rabi oscillation curve. By inserting the values of Rabi oscillation frequency and average phonon number, measured independently, we obtain the value of the Lamb Dicke parameter as 0.061. Theoretically, the Lamb-Dicke parameter for this system is 0.042. The discrepancy may stem from the fitting uncertainty as the χ^2 is only 0.85, dominated by magnetic field fluctuation.
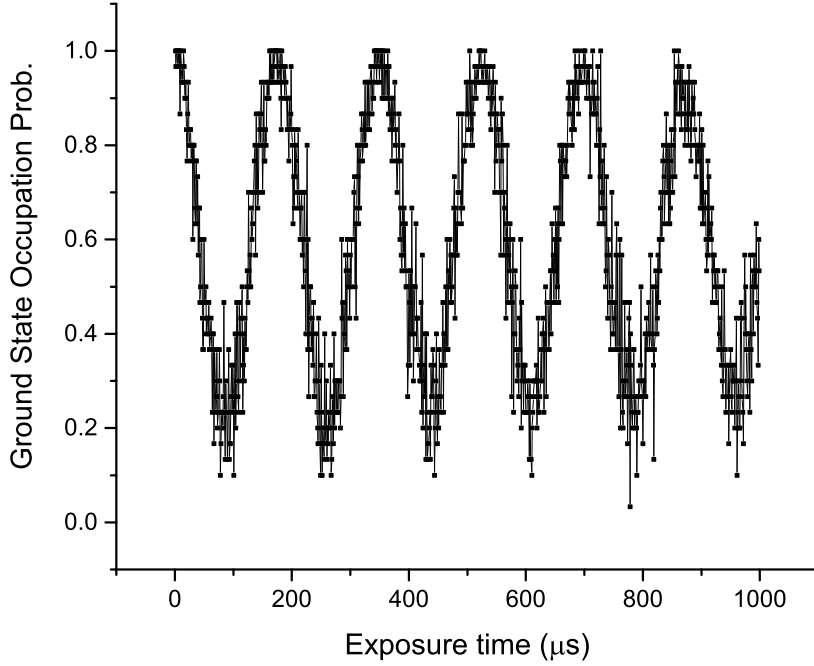
Figure 6.15: A typical rabi oscillation. The frequency and amplitude of this oscillation depends on the frequency and intensity of the light.

The fastest qubit operation that can be obtained with our system at present has a Π time of $1.9\mu s$ as is shown in Fig. 6.18. This means that optical qubit operation is possible at frequencies of 263 kHz, which is much faster than the currently reported values [49, 124]. The decoherence time during this operation is $82\mu s$. This means a fidelity loss of $\frac{1}{e}$ or 36% in $82\mu s$ of operation. During that time the number of oscillations is about 21. This gives an average loss of fidelity of 1% per oscillation. We believe that the source of this decoherence is from external magnetic field noise, other than the line frequency as well as noise in the laser frequency and intensity. The Ramsey decoherence time for this qubit is of the order of 6 ms, as is shown in Fig. 6.13. Thus with further optimization of the Rabi oscillation decoherence time, we can have fast qubit operation near the telecom wavelength with long coherence time driven by a diode based laser system.

6.6 Conclusion

The system development and characterization described in this section is aimed towards measurement of quadrupole moment of the $5D_{5/2}$ level of barium ion.
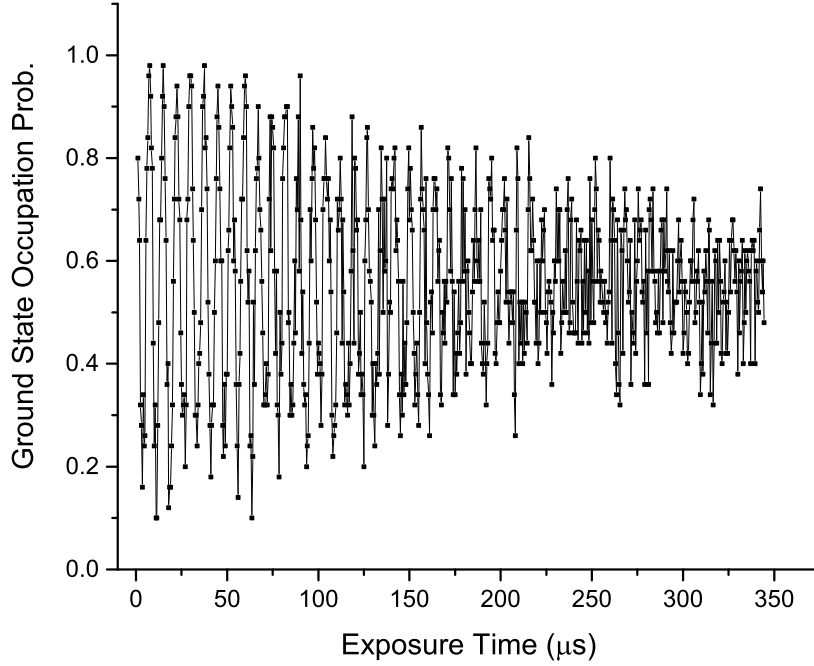
Figure 6.16: Rabi oscillation with decoherence.

From Eq. 3.19, we can estimate the shift for quadrupole moment to be of the order of 200 Hz when the end cap voltage is varied within 1000 V. Our current system allows us to measure the frequency of a single peak with an uncertainty lower than 300 Hz, which is quite close to the expected shift due to quadrupole interaction.

The work thus prepares the system towards measuring the quadrupole moment of the D state of the barium ion. The system provides noise limited linewidth of 300 Hz of the quadrupole transition frequency between the $6S_{1/2}$ state and the $5D_{5/2}$ state of the barium ion on a magnetic field sensitive transition. It in turn allows to determine the transition frequency with an uncertainty less than 300 Hz (limited by the transition linewidth). However, the measurement of the quadrupole moment requires long term stability which is presently being optimized.

The current system also allows to create an optical qubit near the telecom wavelength with operational frequencies of 263 kHz using a diode laser system. It also have driven and free coherence times of $80\mu s$ and 6 ms respectively thus allowing us to perform fast gate operations using a trapped
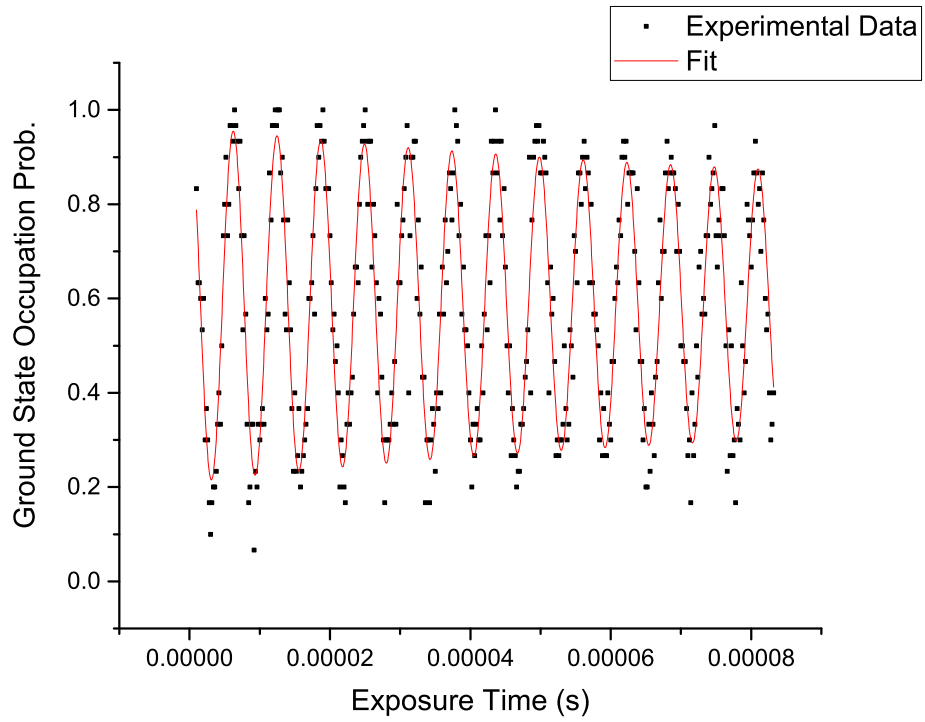
Figure 6.17: Fitting of Eq. 2.26 to Rabi oscillation for extracting the Lamb Dicke parameter. The Rabi frequency used is 161.2903 kHz and the average phonon number is taken as 5.67.
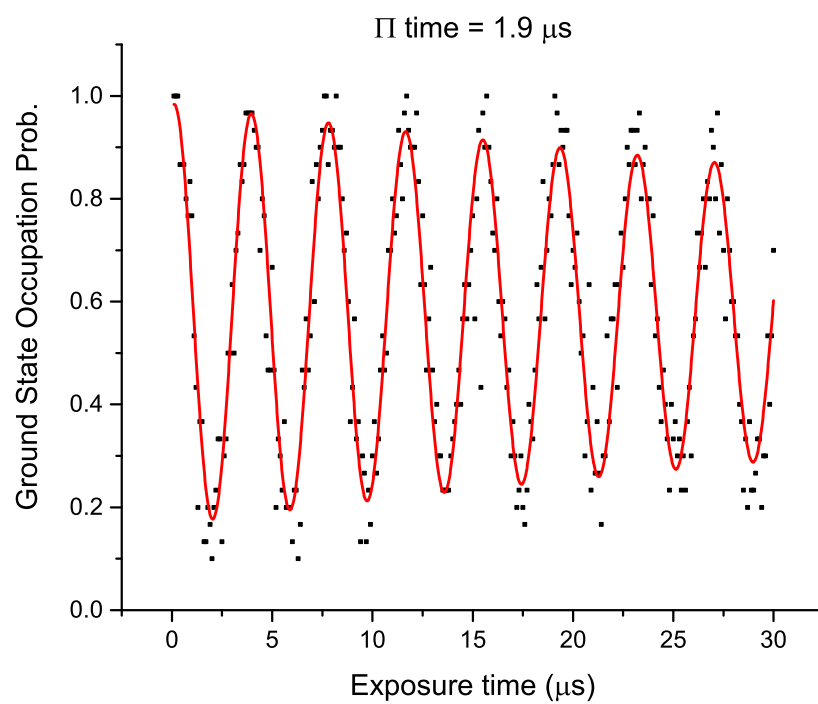
barium ion.

Figure 6.18: The fastest Rabi oscillation frequency we obtained, having a Π time of $1.9 \mu s$ and a Rabi frequency of 263 kHz.

Chapter 7

Conclusion

In this thesis, the work presented has been the culmination of the work for the past four and half years, since the beginning of 2012. During this time, a completely functional atomic physics laboratory was setup from scratch. First precision measurements have been performed with the setup making advances towards realizing PNC measurements using trapped barium ions.

The development of the geometric phase generating ion trap design can now allow us to impart global phases to a large number of ion trap qubits. While the system has not been implemented experimentally, it has helped us to develop necessary technical and scientific skills to handle the project later.

The most precise measurement of branching fractions for the excited state of Barium atom, for both $P_{1/2}$ state, where I contributed primarily and $P_{3/2}$ state, where I contributed in measurements and data analysis. The second part is presented in Tarun Dutta's thesis.

Development of extremely narrow, diode laser based, 1760 nm laser system for driving the quadrupole transition has also opened up possibilities of exploring multitude of physical phenomenon. We have been able to demonstrate extremely fast qubit manipulation capabilities using that laser, primarily because of the narrow linewidth that we could achieve. Our ability to synchronize the experimental system with the line frequency has also allowed us to obtain long coherence times, which in turn has allowed us to reduce the linewidth of the transition, almost to the levels, where we can start detecting the energy level shift because of the interaction of the inherent quadrupole moment with the trap electric field gradient. While there are some systematics left to figure out, the system is

almost ready to perform world first measurement of inherent quadrupole moment of the D state of the barium ion.

The work done here, both theoretical and experimental, has led to multiple publications in peer reviewed journals, which I am listing below-

1. T. Dutta, D. De Munshi and M. Mukherjee (2016). Absolute Te2 Reference for Barium Ion at 455.4nm. Journal of Optical Society of America B, 33, 6, 1177.

2. T. Dutta, D. De Munshi, D. Yum, R. Rebhi and M. Mukherjee (2016). An exacting transition probability measurement- direct test of atomic many-body theories. Scientific Reports 6, 29772.

3. D. De Munshi, T. Dutta, R. Rebhi and M. Mukherjee. (2015). Precision Measurement of Branching fractions of Ba 138+: Testing Many-Body Theories Below 1% level. Physical Review A, 91, 040501(R)

4. D. De Munshi, M. Mukherjee, and B. Dutta-Roy. (2013). Berry Phase Generation and Measurement in a Single Trapped Ion, Physics Letters A 377, 228-231.

This does not include the work performed with the 1760 nm based laser system, manuscript for which is under preparation.

To summarize, the work presented in this thesis has been geared towards precision measurements of atomic properties of a trapped barium atom, with possibilities of implementing ion trap based quantum computation systems.

Bibliography

[1] P. B. Schwinberg, R. S. Van Dyck, Jr., and H. G. Dehmelt, New Comparison of the Positron and Electron g Factors, Phys. Rev. Lett. **47**, 1679 (1981).

[2] Robert S. Van Dyck, Jr., Paul B. Schwinberg, and Hans G. Dehmelt. New high-precision comparison of electron and positron g factors, Phys. Rev. Lett. **59**, 26 (1987).

[3] Frederick G. Walther, William D. Phillips, and Daniel Kleppner, Effect of Nuclear Mass on the Bound-Electron g Factor, Phys. Rev. Lett. **28**, 1159 (1972).

[4] D. T. Wilkinson and H. R. Crane, Precision Measurement of the g Factor of the Free Electron, Phys. Rev. **130**, 852 (1963).

[5] H. H$\ddot{a}$ffner, T. Beier, N. Hermanspahn, H.-J. Kluge, W. Quint, S. Stahl, J. Verd$\acute{u}$, and G. Werth, High-Accuracy Measurement of the Magnetic Moment Anomaly of the Electron Bound in Hydrogenlike Carbon, Phys. Rev. Lett. **85**, 5308 (2000).

[6] J. Alnis, A. Matveev, N. Kolachevsky, Th. Udem, and T. W. H$\ddot{a}$nsch. Subhertz linewidth diode lasers by stabilization to vibrationally and thermally compensated ultralow-expansion glass Fabry-Prot cavities, Phys. Rev. A **77**, 053809 (2008).

[7] Lisheng Chen, John L. Hall, Jun Ye, Tao Yang, Erjun Zang, and Tianchu Li. Vibration-induced elastic deformation of Fabry-Perot cavities, Phys. Rev. A **74**, 053801 (2006).

[8] Kenji Numata, Amy Kemery, and Jordan Camp. Thermal-Noise Limit in the Frequency Stabilization of Lasers with Rigid Cavities, Phys. Rev. Lett. **93**, 250602 (2004).

[9] R Calder and G Lewin. Reduction of stainless-steel outgassing in ultra-high vacuum, Brit. Jour. of Appl. Phys. **18**, 10 (1967).

[10] J. M. Raimond, M. Brune, and S. Haroche, Manipulating quantum entanglement with atoms and photons in a cavity, Rev. Mod. Phys. **73**, 565 (2001).

[11] T. B. Pittman, Y. H. Shih, D. V. Strekalov, and A. V. Sergienko, Optical imaging by means of two-photon quantum entanglement, Phys. Rev. A **52**, R3429(R) (1995).

[12] Anders Karlsson, Masato Koashi, and Nobuyuki Imoto, Quantum entanglement for secret sharing and secret splitting, Phys. Rev. A **59**, 162 (1999).

[13] M. D. Lukin and A. Imamoglu, Nonlinear Optics and Quantum Entanglement of Ultraslow Single Photons, Phys. Rev. Lett. **84**, 1419 (2000).

[14] R. Ursin, et. al., Entanglement-based quantum communication over 144 km, Nature Phys. **3**, 481 (2007).

[15] E. Togan, et. al. Quantum entanglement between an optical photon and a solid-state spin qubit, Nature **466**, 730 (2010).

[16] N. Huntemann, M. Okhapkin, B. Lipphardt, S. Weyers, Chr. Tamm, and E. Peik, High-Accuracy Optical Clock Based on the Octupole Transition in Yb+171, Phys. Rev. Lett. **108**, 090801 (2012).

[17] S. A. Diddams *et. al.*, An Optical Clock Based on a Single Trapped $^{199}Hg^+$ Ion, Science **293**, 825 (2001).

[18] H.S. Margolis *et. al.*, Hertz-Level Measurement of the Optical Clock Frequency in a Single $^{88}Sr^+$ Ion, Science **306**, 1355 (2004).

[19] C. Monroe, R. Raussendorf, A. Ruthven, K. R. Brown, P. Maunz, L.-M. Duan, and J. Kim. Large-scale modular quantum-computer architecture with atomic memory and photonic interconnects, Phys. Rev. A **89**, 022317 (2014).

[20] Stephan Gulde, Mark Riebe, Gavin P. T. Lancaster, Christoph Becher, Jrgen Eschner, Hartmut Hffner, Ferdinand Schmidt-Kaler, Isaac L. Chuang and Rainer Blatt. Implementation of the DeutschJozsa algorithm on an ion-trap quantum computer, Nature **421**, 48 (2003).

[21] D. Kielpinski, C. Monroe and D. J. Wineland. Architecture for a large-scale ion-trap quantum computer, Nature, **417**, 709 (2002).

[22] J. I. Cirac and P. Zoller. A scalable quantum computer with ions in an array of microtraps, Nature **404**, 579 (2000).

[23] N. Yu, W. Nagourney, and H. Dehmelt. Radiative Lifetime Measurement of the Ba^+ Metastable $D_{3/2}$ State, Phys. Rev. Lett. **78**, 4898 (1997).

[24] A. A. Madej and J. D. Sankey. Quantum jumps and the single trapped barium ion: Determination of collisional quenching rates for the $5d^2D_{5/2}$ level, Phys. Rev. A **41**, 2621 (1990).

[25] Geetha Gopakumar, Holger Merlitz, Rajat K. Chaudhuri, B. P. Das, Uttam Sinha Mahapatra, and Debashis Mukherjee. Electric dipole and quadrupole transition amplitudes for Ba^+ using the relativistic coupled-cluster method, Phys. Rev. A **66**, 032505 (2002).

[26] B. K. Sahoo, B. P. Das, R. K. Chaudhuri, and D. Mukherjee. Theoretical studies of the $6s^2S_{1/2} \rightarrow 5d^2D_{3/2}$ parity-nonconserving transition amplitude in Ba^+ and associated properties, Phys. Rev. A **75**, 032507 (2007).

[27] C. F. Roos, M. Chwalla, K. Kim, M. Riebe and R. Blatt. 'Designer atoms' for quantum metrology, Nature **443**, 316 (2006).

[28] M. G. Raizen, J. M. Gilligan, J. C. Bergquist, W. M. Itano, and D. J. Wineland, Ionic crystals in a linear Paul trap, Phys. Rev. A **45**, 6493 (1992).

[29] M. Drewsen, C. Brodersen, L. Hornekr, J. S. Hangst, and J. P. Schifffer, Large Ion Crystals in a Linear Paul Trap, Phys. Rev. Lett. **81**, 2878 (1998).

[30] M. Drewsen and A. Brner, Harmonic linear Paul trap: Stability diagram and effective potentials, Phys. Rev. A **62**, 045401 (2000).

[31] G Huber, T Deuschle, W Schnitzler, R Reichle, K Singer and F Schmidt-Kaler, Transport of ions in a segmented linear Paul trap in printed-circuit-board technology, New Jour. Phys. **10**, (2008).

[32] D. J. Berkeland, Linear Paul trap for strontium ions, Rev. Sci. Instrum. **73**, 2856 (2002).

[33] D. A. Church, Storage-Ring Ion Trap Derived from the Linear Quadrupole Radio-Frequency Mass Filter, J. Appl. Phys. **40**, 3127 (1969).

[34] H. B. Pedersen, D. Strasser, S. Ring, O. Heber, M. L. Rappaport, Y. Rudich, I. Sagi, and D. Zajfman, Ion Motion Synchronization in an Ion-Trap Resonator, Phys. Rev. Lett. **87**, 055001 (2001).

[35] Lowell S. Brown and Gerald Gabrielse, Geonium theory: Physics of a single electron or ion in a Penning trap, Rev. Mod. Phys. **58**, 233 (1986).

[36] G. Savard, St. Becker, G. Bollen, H.-J. Kluge, R.B. Moore, Th. Otto, L. Schweikhard, H. Stolzenberg, U. Wiess, A new cooling technique for heavy ions in a Penning trap, Phys. Lett. A **158**, 247, (1991).

[37] Lowell S. Brown and Gerald Gabrielse, Precision spectroscopy of a charged particle in an imperfect Penning trap, Phys. Rev. A **25**, 2423(R) (1982).

[38] D. Liebfried, R. Blatt, C. Monroe and D. Wineland. Quantum dynamics of single trapped ions, Review of Mod. Phys. **75**, (2003).

[39] P.K. Ghosh. Ion Traps, Clarendon Press; Oxford (United Kingdom). (1995).

[40] D. J. Wineland, Wayne M. Itano, J. C. Bergquist, and Randall G. Hulet. Laser-cooling limits and single-ion spectroscopy, Phys. Rev. A **36**, 2220 (1987).

[41] F. Diedrich, J. C. Bergquist, Wayne M. Itano, and D. J. Wineland. Laser Cooling to the Zero-Point Energy of Motion, Phys. Rev. Lett. **62**, 403 (1989).

[42] J. S. Hangst, M. Kristensen, J. S. Nielsen, O. Poulsen, J. P. Schiffer, and P. Shi. Laser cooling of a stored ion beam to 1 mK, Phys. Rev. Lett. **67**, 1238 (1991).

[43] E. Peik, G. Hollemann, and H. Walther. Laser cooling and quantum jumps of a single indium ion, Phys. Rev. A **49**, 402 (1994).

[44] D. J. Larson, J. C. Bergquist, J. J. Bollinger, Wayne M. Itano, and D. J. Wineland, Sympathetic cooling of trapped ions: A laser-cooled two-species nonneutral ion plasma, Phys. Rev. Lett. **57**, 70 (1986).

[45] J. I. Cirac, R. Blatt, P. Zoller, and W. D. Phillips, Laser cooling of trapped ions in a standing wave, Phys. Rev. A **46**, 2668 (1992).

[46] D. J. Wineland, J. C. Bergquist, Wayne M. Itano, J. J. Bollinger, and C. H. Manney, Atomic-Ion Coulomb Clusters in an Ion Trap, Phys. Rev. Lett. **59**, 2935 (1987).

[47] F. Diedrich, E. Peik, J. M. Chen, W. Quint, and H. Walther, Observation of a Phase Transition of Stored Laser-Cooled Ions, Phys. Rev. Lett. **59**, 2931 (1987).

[48] Harold J. Metcalf and Peter van der Straten. Laser Cooling and Trapping. Springer-Verlag, (1999).

[49] Lukˇ Slodiˇcka, Single ion - single photon interactions in free space, Thesis, Institute for Experimental Physics, Innsbruck (2000).

[50] C. Bouchiat, Parity violation in atomic processes, Journal of Physics G: Nuclear Physics **3**, 2 (1977).

[51] Marie-Anne Bouchiat and Claude Bouchiat, Parity violation in atoms, Rep. Prog. Phys. **60**, 1351 (1997).

[52] C. Monroe, D. M. Meekhof, B. E. King, W. M. Itano, and D. J. Wineland. Demonstration of a Fundamental Quantum Logic Gate, Phys. Rev. Lett **75**, 4714 (1995).

[53] N. Fortson, Possibility of measuring parity nonconservation with a single trapped atomic ion, Phys. Rev. Lett. **70**, 2383 (1993).

[54] P. Mandal and M. Mukherjee, Quantum metrology to probe atomic parity nonconservation, Phys. Rev. A **82**, 050101(R) (2010).

[55] R. Gerritsma, G. Kirchmair, F. Zhringer, J. Benhelm, R. Blatt, C. F. Roos, Precision measurement of the branching fractions of the $4p^2 P_{3/2}$ decay of Ca II, Euro. Phys. Jour. D, **50**, 13 (2008).

[56] W. M. Itano, External-field shifts of the 199Hg optical frequency standard, J. Res. Natl Inst. Stand. Technol. **105**, 829 (2000).

[57] C. S. Wu, E. Ambler, R. W. Hayward, D. D. Hoppes, and R. P. Hudson, Experimental Test of Parity Conservation in Beta Decay, Phys. Rev. **105**, 1413 (1957).

[58] Aaron E. Leanhardt, *et. al.*, High-resolution spectroscopy on trapped molecular ions in rotating electric fields: A new approach for measuring the electron electric dipole moment J. Mol. Spec. **270**, 1 (2011).

[59] C. F. Roos, Controlling the quantum state of trapped ions, Thesis, Institute for Experimental Physics, Innsbruck (2000).

[60] D.F.V. James, Quantum dynamics of cold trapped ions with application to quantum computation, Appl. Phys. B, **66**, 181 (1998).

[61] J. K. Webb , V.V. Flambaum, C.W. Churchill, M.J. Drinkwater, and J.D. Barrow, Search for Time Variation of the Fine Structure Constant, Phys. Rev. Lett **82**, 884 (1999).

[62] S. A. R. Horsley and M. Babiker, Topological Phases for Composite Particles with Dynamic Properties, Phys. Rev. Lett. **99**, 090401 (2007).

[63] F. Wilczek and A. Zee, Appearance of Gauge Structure in Simple Dynamical Systems, Phys. Rev. Lett. **52**, 2111 (1984).

[64] J. E. Avron, R. Seiler and L. G. Yaffe, Adiabatic theorems and applications to the quantum hall effect, Commun. Math. Phys. **110**, 33 (1987).

[65] Z.-C. Wang and B.-Z. Li, Geometric phase in relativistic quantum theory, Phys. Rev. A **60**, 4313 (1999).

[66] Edmund R. Meyer, Aaron E. Leanhardt, Eric A. Cornell, and John L. Bohn, Berry-like phases in structured atoms and molecules, Phys. Rev. A , **80**, 062110 (2009).

[67] A. Vutha and D. DeMille, arXiv:0907.5116 (2009).

[68] R.Tycko, Adiabatic Rotational Splittings and Berry's Phase in Nuclear Quadrupole Resonance, Phys. Rev. Lett. **58**, 2281-2284 (1987).

[69] M. V. Berry, Quantal phase factors accompanying adiabatic changes, Proc. R. Soc. London A **392**, 45-57 (1984).

[70] W.M. Itano, Quadrupole moments and hyperfine constants of metastable states of Ca^+, Sr^+, Ba^+, Yb^+, Hg^+, and Au, Phys. Rev. A **73**, 022510 (2006).

[71] X.-P. Huang, F. Anderegg, E.M. Hollmann, C.F. Driscoll and T.M. O'Neil, Steady-State Confinement of Non-neutral Plasmas by Rotating Electric Fields, Phys. Rev. Lett. **78**, 875 (1997).

[72] G. P. Barwood, H. S. Margolis, G. Huang, P. Gill, and H. A. Klein, Measurement of the Electric Quadrupole Moment of the $4d^2D_{5/2}$ Level in ^{88}Sr$^+$, Phys. Rev. Lett. **93**, 133001 (2004).

[73] W. H. Oskay, W. M. Itano, J. C. Bergquist, Measurement of the ^{199}Hg$^+$ 5d^{9}6s$^2{}^2$D$_{5/2}$ Electric Quadrupole Moment and a Constraint on the Quadrupole Shift, Phys. Rev. Lett. **94**, 163001 (2005).

[74] P. Zanardi and M. Rasetti, Holonomic quantum computation, Phys. Lett. A **264**, 94-99 (1999).

[75] A. Ekert, Marie Ericsson , Patrick Hayden , Hitoshi Inamori , Jonathan A. Jones , Daniel K. L. Oi and Vlatko Vedral,Geometric quantum computation, Jour. Mod. Optics **47**, 14 (2000).

[76] L.M. Duan, J.I. Cirac and P.Zoller,Geometric Manipulation of Trapped Ions for Quantum Computation, Science **292**, 1695 (2001).

[77] Shi-Liang Zhu and Z.D. Wang, Unconventional Geometric Quantum Computation, Phys. Rev. Lett. **91**, 187902 (2003).

[78] Cosmo Lupo and Paolo Aniello, Robustness of the geometric phase under parametric noise, Phys. Scr. **79**, 065012 (2009).

[79] E. Knill, Nature, Physics: Quantum computing **463**, 441, (2010).

[80] K. R. Brown, A. C. Wilson, Y. Colombe, C. Ospelkaus, A. M. Meier, E. Knill, D. Leibfried, and D. J. Wineland, *et.al*, Single-qubit-gate error below 10-4 in a trapped ion Phys. Rev. A **84**, 030303 (2011).

[81] A. Lemmer, A. Bermudez and M. B. Plenio, Driven geometric phase gates with trapped ions, New J. Phys. **15**, 083001, (2013).

[82] A. Jacob, P. Oheberg, G. Juzeliunas, I. Santos, Cold atom dynamics in non-Abelian gauge fields, Appl. Phys. B **89**, 439 (2007).

[83] J.P. Vyasanakere, S. Zhang, V.B. Shenoy, BCS-BEC crossover induced by a synthetic non-Abelian gauge field, Phys. Rev. B **84**, 014512 (2011).

[84] Y.F. Wang, H. Yao , Z.C. Gu, C.D. Gong, D.N. Sheng, Non-Abelian Quantum Hall Effect in Topological Flat Bands, Phys. Rev. Lett. **108**, 126805 (2012).

[85] Jonas Larson and Sergey Levin, Effective Abelian and Non-Abelian Gauge Potentials in Cavity QED, Phys. Rev. Lett. **103**, 013602 (2009).

[86] Karl-Peter Marzlin and Barry C. Sanders, Inconsistency in the Application of the Adiabatic Theorem, Phys. Rev. Lett. **93**, 160408 (2004).

[87] C. Brouder, Gabriel Stoltz and Gianluca Panati, Adiabatic approximation, Gell-Mann and Low theorem, and degeneracies: A pedagogical example, Phys. Rev. A **78**, 042102 (2008).

[88] C. Zu, W.-B. Wang, L. He, W.-G. Zhang, C.-Y. Dai, F. Wang and L.-M. Duan, Experimental realization of universal geometric quantum gates with solid-state spins, Nature **514**, 72 (2014).

[89] Barry Simon, Holonomy, the Quantum Adiabatic Theorem, and Berry's Phase, Phys. Rev. Lett. **51**, 2167 (1984).

[90] D. De Munshi, M. Mukherjee, B. Dutta-Roy, Berry phase generation and measurement in a single trapped ion, Phys. Lett. A **377**, 228 (2013).

[91] D. J. Armstrong, R. P. Wood, and C. H. Greene, Photoionization Of The 5d6p 3d1 State Of Barium, Phys. Rev. A **47**, (1993).

[92] D. J. Armstrong, and J. Cooper, Isotope-Selective Photoionization Spectroscopy Of Barium, Phys. Rev. A **47**, R2446 (1993).

[93] L.-W. He, C. E. Burkhardt, M. Ciocca, J. J. Leventhal, H.-L. Zhou and S. T. Manson, Correlation effects in the photoionization of Ba(6s6p 1P1).: Determination of cross sections for production of specific final J states, Phys. Rev. A **51**, 2085 (1995).

[94] L.-W. He, C. E. Burkhardt, M. Ciocca, J. J. Leventhal, and S. T. Manson, Absolute cross sections for the photoionization of the 6s6p 1P excited state of barium, Phys. Rev. Lett. **67**, 2131 (1991).

[95] V. Lange, U. Eichmann, and W. Sandner, Photoionization Of Excited Barium 6s6p (1).P1, Phys. Rev. A **44**, 4737 (1991).

[96] R. P. Wood, C. H. Greene, and D. Armstrong, Photoionization of the barium 6s6p $1P_{\pm 1}$ state, Phys. Rev. A 47, 229 (1993).

[97] Daniel Rotter, Quantum feedback and quantum correlation measurements with a single Barium ion, Thesis, Institute for Experimental Physics, Innsbruck (2000).

[98] S. Olmschenk *et al.*, Measurement of the lifetime of the $6p^2 P_{1/2}^0$ level of Yb$^+$, Phys. Rev. A **80**, 022502 (2009).

[99] J. A. Sherman, A. Andalkar, W. Nagourney and E. N. Fortson, Measurement of light shifts at two off-resonant wavelengths in a single trapped Ba+ ion and the determination of atomic dipole matrix elements, Phys. Rev. A **78**, 052514 (2008).

[100] N. Kurz, M. R. Dietrich, Gang Shu, R. Bowler, J. Salacka, V. Mirgon, and B. B. Blinov, Measurement of the branching ratio in the $6P_{3/2}$ decay of BaII with a single trapped ion, Phys. Rev. A **77**, 060501(R) (2008).

[101] D. Nigg, M. Mller,E. A. Martinez, P. Schindler, M. Hennrich, T. Monz, M. A. Martin-Delgado and R. Blatt, Quantum computations on a topologically encoded qubit Science **345**, 302 (2014).

[102] A. C. Wilson, Y. Colombe, K. R. Brown, E. Knill, D. Leibfried and D. J. Wineland, Tunable spinspin interactions and entanglement of ions in separate potential wells, Nature **512**, 57 (2014).

[103] C. W. Chou, D. B. Hume, T. Rosenband, D. J. Wineland, Optical Clocks and Relativity, Science **329**, 1630 (2010).

[104] M. Leventhal, D. E. Murnick, and H. W. Kugel, Lamb-Shift Measurement for the n=2 State of Hydrogenic ^{16}O, Phys. Rev. Lett. **28**, 1609 (1972).

[105] C. S. Wood, S. C. Bennett, D. Cho, B. P. Masterson, J. L. Roberts, C. E. Tanner and C. E. Wieman, Measurement of Parity Nonconservation and an Anapole Moment in Cesium, Science **275**, 1759 (1997).

[106] M. Mukherjee *et al.*, The Mass of ^{22}Mg Phys. Rev. Lett. **93**, 150801 (2004).

[107] J. J. Hudson, D. M. Kara, I. J. Smallman, B. E. Sauer, M. R. Tarbutt and E. A. Hinds, Improved measurement of the shape of the electron, Nature **473**, 493 (2011).

[108] B. K. Sahoo, P. Mandal, and M. Mukherjee, Parity nonconservation in odd isotopes of single trapped atomic ions Phys. Rev. A **83**, 030502(R) (2011).

[109] Michael Ramm, Thaned Pruttivarasin, Mark Kokish, Ishan Talukdar, and Hartmut Hffner, Precision Measurement Method for Branching Fractions of Excited $P_{1/2}$ States Applied to ^{40}Ca$^+$, Phys. Rev. Lett. **111**, 023004 (2013).

[110] C. Raab, J. Bolle, H. Oberst, J. Eschner, F. Schmidt-Kaler, R. Blatt, Diode laser spectrometer at 493 nm for single trapped Ba+ ions, App. Phys. B **67**, 683 (1998).

[111] M. D. Davidson, L. C. Snoek, H. Volten and A. D"onszelmann, Oscillator strengths and branching ratios of transitions between low-lying levels in the barium II spectrum, Astron. Astrophys. **255**, 457 (1992).

[112] Anders Kastberg, Petrine Villemoes, Arne Arnesen, Filip Heijkenskjld, Alexander Langereis, Peter Jungner, and Staffan Linnus, Measurements of absolute transition probabilities in Ba II through optical nutation, J. Opt. Soc. Am. B **10**, 1330 (1993).

[113] P. Kuske, N. Kirchner, W. Wittmann, H.J. Andr, D. Kaiser, Lifetime measurements by pulsed laser excitation of fast ion beams, Phys. Lett. A **64**, 377 (1978).

[114] Tarun Dutta, Debashis De Munshi, Dahyun Yum, Riadh Rebhi and Manas Mukherjee, An exacting transition probability measurement - a direct test of atomic many-body theories, Scientific Reports **6**, 29772 (2016).

[115] J. J. Curry, Compilation of Wavelengths, Energy Levels, and Transition Probabilities for Ba I and Ba II, J. Phys. Chem. Ref. Data **33**, 745 (2004).

[116] V. A. Dzuba, V. V. Flambaum, and J. S. M. Ginges, Calculations of parity-nonconserving s-d amplitudes in Cs, Fr, Ba+, and Ra+, Phys. Rev. A **63**, 062101 (2001).

[117] C. Guet and W. R. Johnson, Relativistic many-body calculations of transition rates for Ca$^+$, Sr$^+$, and Ba$^+$ Phys. Rev. A, **44**, 1531 (1991).

[118] Alan Gallagher, Oscillator Strengths of Ca II, Sr II, and Ba II, Phys. Rev. **157**, 24 (1967).

[119] J. Reader, C. J. Corliss, W. L. Wiese and G. A. Martin, Wavelengths and transitions probabilities for atoms and atomic ions, Natl. Bur. Stand. (US). Circ. No. 68, vol. X (US GPO, Washington, DC). (1980).

[120] D. De Munshi, T. Dutta, R. Rebhi and M. Mukherjee, Precision Measurement of Branching fractions of Ba 138+: Testing Many-Body Theories Below 1% level. Physical Review A **91**, 040501(R) (2015).

[121] Th. Sauter, W. Neuhauser, R. Blatt, and P. E. Toschek, Observation of Quantum Jumps, Phys. Rev. Lett. **57**, 1696 (1986).

[122] K. H. Kn*ö*ll, G. Marx, K. H*ü*bner, F. Schweikert, S. Stahl, Ch. Weber, and G. Werth, Experimental g_J factor in the metastable 5D$_{3/2}$ level of Ba$^+$, Phys. Rev. A **54**, 1199 (1996).

[123] N. Kurz, M. R. Dietrich, Gang Shu, T. Noel, and B. B. Blinov, Measurement of the Lande g factor of the 5D$_{5/2}$ state of Ba II with a single trapped ion, Phys. Rev. A **82**, 030501(R) (2010).

[124] M. R. Dietrich, N. Kurz, T. Noel, G. Shu, and B. B. Blinov, Hyperfine and optical barium ion qubits, Phys. Rev. A **81**, 052328 (2010).

[125] C. J. Myatt, B. E. King, Q. A. Turchette, C. A. Sackett, D. Kielpinski, W. M. Itano, C. Monroe and D. J. Wineland, Decoherence of quantum superpositions through coupling to engineered reservoirs, Nature **403**, 269 (2000).

[126] D. Kielpinski, V. Meyer, M. A. Rowe, C. A. Sackett, W. M. Itano, C. Monroe, D. J. Wineland, MA Decoherence-Free Quantum Memory Using Trapped Ions, Science **291**, 1013 (2001).

[127] G. J. Milburn, Intrinsic decoherence in quantum mechanics, Phys. Rev. A **44**, 5401 (1991).

[128] H. Moya-Cessa, V. Buek, M. S. Kim, and P. L. Knight, Intrinsic decoherence in the atom-field interaction, Phys. Rev. A **48**, 3900 (1993).

[129] D. J. Wineland and Wayne M. Itano, Laser cooling of atoms, Phys. Rev. A **20**, 1521 (1979).